University of Nevada, Reno

Mineral Ridge: A Late Cretaceous Orogenic Gold System in the

Miocene Silver Peak-Lone Mountain Metamorphic Core Complex

By

Micah N. Claypoole

Dr. Michael W. Ressel/Thesis Advisor

May 2018

N

We recommend that the thesis
prepared under our supervision by

MICAH NOAH CLAYPOOLE

entitled

Mineral Ridge: A Late Cretaceous Orogenic Gold System in the
Miocene Silver Peak-Lone Mountain Metamorphic Core Complex

be accepted in partial fulfillment of the
requirements for the degree of

MASTER OF SCIENCE

Michael W. Ressel, PhD, Advisor

John L. Muntean, PhD, Committee Member

Scott D. Bassett, PhD, Graduate School Representative

David W. Zeh, PhD, Dean, Graduate School

May, 2018

Abstract

Gold deposits in rocks of the Silver Peak metamorphic core complex in west-central Nevada are contained in highly deformed, sheeted milky quartz veins that cut Neoproterozoic metasedimentary rocks and Cretaceous peraluminous granite and migmatite. Gold production at Mineral Ridge since discovery in 1864 has been approximately 1 million oz. Gold-bearing veins are concentrated in a major low-angle ductile shear system active during the Late Cretaceous. However, a broadly coincident brittle detachment cuts the ductile shear, separating metasedimentary and foliated granitic rocks from overlying non-metamorphosed Cambrian carbonates and Cenozoic volcanics. The Mineral Ridge biotite-muscovite granite pluton bounds the ductile shear along its roof, defining a wedge of prospective metamorphic rocks generally <50-m-thick. Zones of intense shearing generally correspond to highest vein density and therefore, gold grades, and such zones are overprinted with strong but narrowly defined quartz-sericite-pyrite-carbonate alteration. Vein boudins are subparallel to the strong planar to anastomosing shear fabric best developed over 1-10 meter thicknesses at contacts between muscovite schist and/or marble, and foliated granite. Gold-bearing veins contain Au:Ag of ≥4, zoned base metals, low As, Sb, and Hg, but high Bi, the latter correlating with gold.

Vein-bearing granites at Mineral Ridge yield U/Pb zircon ages of 91.7+/-0.3 Ma and 89.9+/-0.5 Ma and likely derive from crustal melts during peak metamorphism. Hydrothermal monazite in gold-bearing quartz veins yielded a U/Pb age of 76.0+/-1.8 Ma, indicating veins are unrelated to granites and formed during retrograde greenschist conditions. Previous cooling ages on mica in granites of ~42 and 53 Ma further define the cooling path to ~300°C. Mineral Ridge is interpreted as an orogenic gold system associated with a brittle-ductile shear that formed at depths as much as 11-20 km during the waning stages of Late Cretaceous Sevier contraction. Major exhumation occurred in the late Miocene in association with detachment and transtension in the Walker Lane deformation belt.

Acknowledgements

This project was made possible due to the support of many people, most importantly the faculty and students of the Ralph J. Roberts Center for Research in Economic Geology (CREG). My advisor especially, Dr. Mike Ressel, who provided the guidance, vision, and prodding required to finish this thesis. He is a deep well of Nevada regional knowledge and was instrumental in keeping me from falling too far down all the tangential rabbit holes along the way. Thank you to Dr. John Muntean, CREG's untiring leader, who helped this project behind the scenes but most importantly for his dedication and enthusiasm for teaching ore deposits, courses regarded as the most rigorous and fulfilling and useful learning experiences by me and my peers. Dawn Snell cannot be thanked enough for all the help with forms, fees, sheets, WorkDay, and all other forms of university bureaucy.

Thank you to Scott Briscoe formerly of Scorpio Gold for generating this project with Mike and for funding of analysis and thin sections. I appreciate the guidance from Ajeet Milliard during zircon separations, and to Dr. Joel DesOrmeau and Carolina Zamora for later zircon work that I was quite happy to not repeat myself. On the same page, a thank you to Da Wang at Washington State University for guiding me through the unknown world (to us both) of dating hydrothermal monazites.

To the students of the CREG department and UNR geology at large, I cannot envision completion of this thesis without their support, guidance, and friendship. Too many to name all who made the long drives to laser labs and conferences easier, talking me through the university red tape, or blathering about quartz textures over pizza, but especially David Freedman and Robert Selwood who could always be counted on to peel off from the office to continue highly academic conversations over several pints of ale.

And I am forever thankful to my parents Mark and Genie Claypoole who have been completely behind me in whatever path I go down. I know they never think twice about supporting me in any way they can.

Contents

List of Tables

List of Figures

Introduction

The Mineral Ridge gold deposit in Esmeralda County, west-central Nevada (Figure 1), is a shear-related quartz vein system hosted in highly deformed metamorphic and granitic rocks that has produced almost one million ounces of gold since the 1860s. Most production occurred underground from 1933 to 1942 (Albers and Stewart, 1972) and from intermittent underground and open-pit mining from 1991 to 2005, and 2012 to 2017. Mineral Ridge lies in the Walker Lane, a zone of disrupted structures that accommodates late Miocene to recent deformation between the Sierra Nevada Mountains to the west and the Basin and Range province to the east (Wesnousky, 2005). Although not a pure extensional terrane like the rest of the Basin and Range, extension in the Walker Lane exhumed mineralized lower-crustal rocks at Mineral Ridge in a metamorphic core complex (Kirsch, 1971), juxtaposing mineralized, metamorphosed, and tectonized clastic and carbonate strata of Neoproterozoic to Cambrian age against unmineralized and largely unmetamorphosed upper-plate rocks. Late Cretaceous peraluminous granite and pre-Tertiary hornblende-rich mafic sills intrude the lower-plate metasedimentary rocks and are concordant with the metamorphic fabric; in turn, pre-Tertiary rocks are intruded by non-foliated, high-angle Miocene mafic dikes (Petronis et al., 2002).

Gold mineralization at Mineral Ridge occurs in quartz veins that primarily cut the Wyman Formation, a Neoproterozoic to Cambrian, locally metamorphosed clastic and carbonate unit, and to a lesser extent, the granitoid intrusions. Gold-bearing quartz veins are hosted in a major ductile shear zone, which preferentially occurs along the contact between foliated granites and the lower amphibolite-upper greenschist facies metasedimentary strata. Previous studies at Mineral Ridge (Spurr, 1906; Bercaw, 1986) interpreted a genetic relationship between the auriferous quartz veins and the felsic intrusions, primarily due to the spatial association of pegmatites and gold lodes and the tendency of pegmatites to transition into quartz-rich veins at the top of the Mineral Ridge

pluton, where gold-bearing quartz veins also occur. However, Mineral Ridge also exhibits characteristics of orogenic lode gold systems, most importantly based on 1) a high degree of structural control of ore, 2) an essentially gold-only ore composition, and 3) ductilely-deformed ore zones hosted in greenschist-facies metamorphic rocks without a clear genetic or temporal relationship to magmatism.

The first detailed mineral deposit study of Mineral Ridge and Silver Peak area was by Josiah Spurr in 1906. Spurr's meticulous report concluded a magmatic origin was the most likely source of gold. Eighty years later, a M.S. study of gold mineralization at Mineral Ridge conducted by Louise Bercaw (1986) focused on the Oromonte area located west of the main-producing mines at Drinkwater and Mary. Extensive surface and underground mapping led Bercaw to a similar conclusion as Spurr, that the quartz-rich pegmatites were ultimately the source for gold in ore-stage quartz veins and lenses.

Objective

The main objectives of this study were to describe and characterize the gold mineralization and constrain the timing and relationships between gold-bearing quartz veins, igneous intrusions, and ductile and brittle-ductile shear deformation. Towards these goals, field work in the summers of 2015 and 2016 consisted of outcrop and pit mapping and sample collection. Geochemical, geochronological, and petrographic analyses of Mineral Ridge samples helped to characterize and better constrain both the overall geologic setting and gold mineralization. If gold mineralization at Mineral Ridge is related to igneous processes, it should have occurred synchronous with or shortly post-dated exposed igneous intrusions that host ore and exhibit geologic, petrographic, and geochemical characteristics of reduced, intrusion-related gold systems (e.g., Thompson et al., 1999; Hart et al., 2007). Alternatively, if the mineralization is not genetically related to the igneous intrusions, it should have ages that are demonstrably younger or older than those of the intrusions

and have a much closer relationship to other major process such as to fluid-focusing shearing and

metamorphism in the case of orogenic systems.
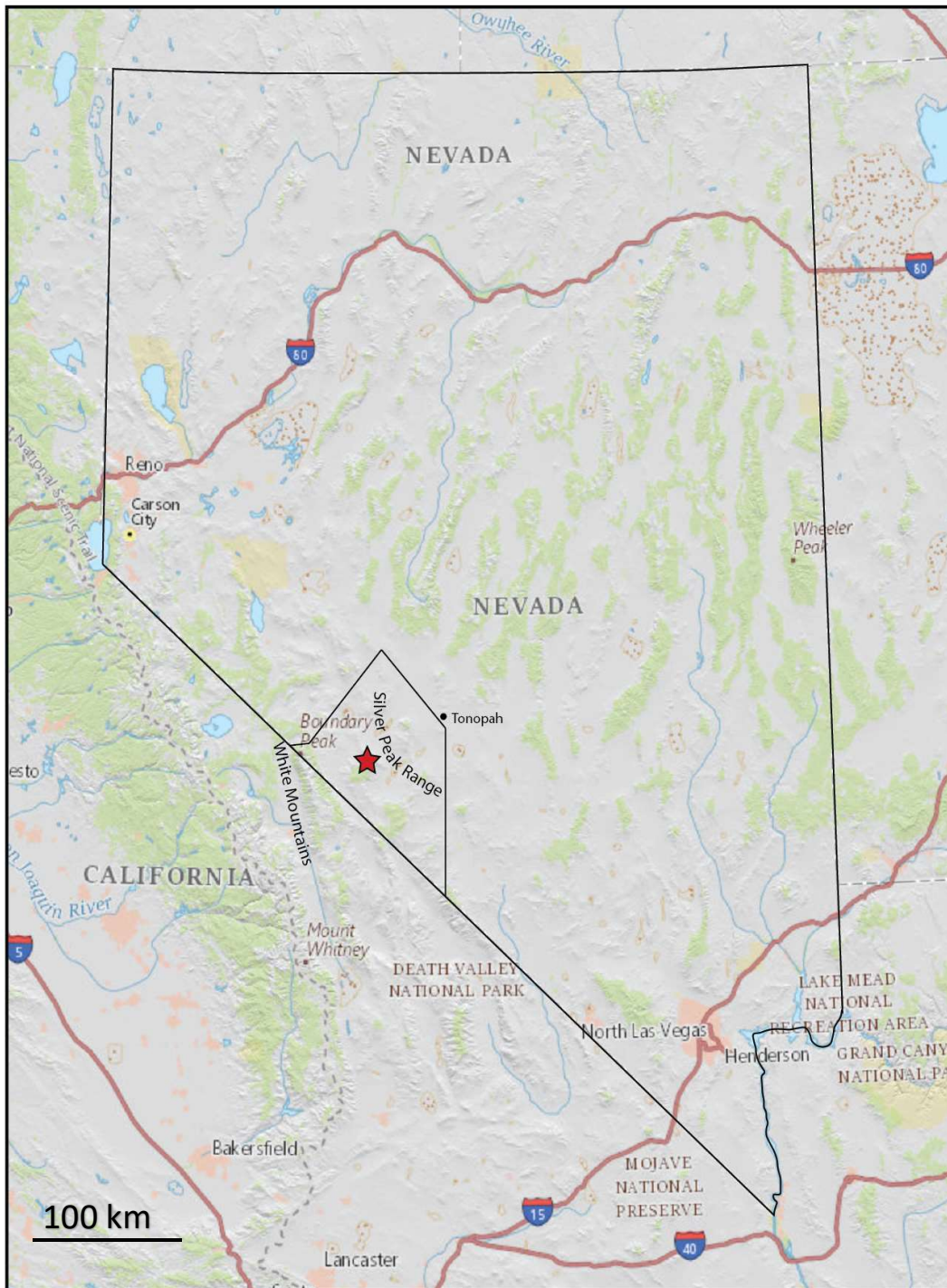
Figure 1. Location map of Mineral Ridge (red star) and Silver Peak Range within Esmeralda County (black outline), west-central Nevada.

Methods

This study combined observational and analytical methods to investigate the timing and style of gold mineralization in the Mineral Ridge area. In the field, outcrop and highwall mapping established the relationships between intrusions, mineralization, structural controls, and alteration characteristics and provided the geologic context for samples collected for geochemical, petrographic, and geochronologic studies. Laboratory analysis included reflected and transmitted light petrography, scanning electron microscopy with energy dispersive X-ray spectroscopy (SEM-EDS) for in-situ compositional determinations, whole-rock and trace-element geochemistry on bulk rock samples, and U/Pb and $^{40}Ar/^{39}Ar$ geochronology.

Field work

Field work at the Mineral Ridge gold mine was conducted during the summers of 2015-2016 and consisted of outcrop and subcrop mapping at 1:2000 scale around the periphery of Mineral Ridge, and 1:1200 scale for highwall mapping in the Drinkwater and Brodie pits. Contour maps derived from digital elevation models (DEM) served as the base for mapping outside of the mine areas, whereas detailed air-surveyed contour maps provided by Scorpio Gold were the base for disturbed areas. Geological mapping included lithology, alteration, and structure overlays. Samples collected during mapping were logged and georeferenced, and some were later selected for further geochemical, geochronological, and/or petrographic analysis.

Whole-rock and trace-element geochemistry

In order to rapidly discriminate mineralized versus unmineralized samples during the early stages of the project, many samples were fire assayed for gold concentration at the Mineral Ridge assay lab; these data are not reported in this study but were used to select samples for later more comprehensive geochemical analyses. During 2015 and 2016, 42 altered and unaltered igneous rocks were selected and later submitted for whole-rock geochemical analysis at ALS Minerals in Vancouver, British Columbia. Chemical compositions were determined through ALS Minerals' CCP-PKG03 analytical package, which uses a lithium borate fusion and acid digestion for major elements,

lithium borate fusion for resistive elements, a four-acid digestion for base metals, and aqua regia for volatile trace metals from 10-gram splits of sample pulps; solutions were then analyzed using inductively coupled plasma mass spectrometry (ICP-MS) and ICP-atomic emission spectrometry (ICP-AES). Gold was quantified by fire-assay on 30-gram splits followed by ICP-AES analysis for low-grade samples and a gravimetric finish for samples containing more than 10 g/t Au. Iron was re-calculated to FeO* from Fe_2O_3, and major elements were normalized to 100% after subtracting lost-on-ignition. Additionally, 52 quartz and quartz-rich samples were analyzed for 48 major and trace elements using ALS Minerals' package ME-MS61, which uses a four-acid digestion preparation followed by analysis by ICP-MS and ICP-AES; gold was determined by fire-assay methods.

Petrography

Polished thin sections were prepared from 47 samples considered representative of the altered and unaltered rocks at Mineral Ridge. Samples were rough cut and marked for final preparation at the University of Nevada, and sent to Spectrum Petrographics in Vancouver, WA and Wagner Petrographic in Lindon, UT for mounting, final cutting, and polishing. Thin sections were examined by transmitted and reflected light microscopy, with selected samples examined with the JEOL-JSM 6010LA scanning electron microscope (SEM) equipped with a semi-quantitative energy-dispersive X-ray spectrometer (EDS) for in-situ elemental determinations of minerals at the University of Nevada, Reno Microbeam Laboratory.

$^{40}Ar/^{39}Ar$ amphibole dating

$^{40}Ar/^{39}Ar$ analyses were made on hornblende phenocrysts from sample 71315, which was collected from the core of a foliated hornblende-plagioclase sill in the Drinkwater mine. The sample was crushed and sieved; the 60-80 mesh fraction was retained and processed with a Frantz Isodynamic magnetic separator at 0.25 amps, and the most magnetic and hornblende-rich fraction was then rinsed in distilled water and agitated in an ultrasonic bath. Dark unaltered hornblende phenocrysts were then hand-picked under a binocular scope. The hornblende separate was irradiated for 7 hours at the United States Geological Survey TRIGA Reactor in Denver, CO and later

analyzed at the Nevada Isotope Geochronology Laboratory at University of Nevada Las Vegas (UNLV) using a MAP215-50-triple-collector mass spectrometer. Irradiated Fish Canyon Tuff FC-2 sanidine with an assigned age of 28.02 Ma (Renne et al., 1998) was used for monitoring neutron flux and as a reference material in calculating the ages of unknown samples. Sample isochrons are based on the MSWD criteria of Wendt and Carl, (1991).

U-Pb zircon dating

Cathodoluminescence (CL) imaging of zircon for U-Pb dating was performed at the Microbeam Laboratory at the University of Nevada, Reno (UNR)using a JEOL JSM-7100FT FESEM equipped with a Deben panchromatic cathodoluminescence (CL) detector and Oxford Aztec EDS system.CL was used to inspect mounted and polished zircons for zonation and inherited zircon cores. Zircon grains were separated by crushing, sieving, magnetic separation, and heavy liquid methods, then mounted and polished at UNR. Zircon crystals from two granitic samples (624BR5 and 021101) were dated using the U-Pb zircon method at the Washington State University (WSU) Radiogenic Isotope and Geochronology Laboratory. Zircon grains were ablated with the New Wave UP-213 laser ablation system and concentrations of the radiogenic isotopes of uranium, thorium, and lead were measured by a Finnigan (ThermoScientific) Element 2 inductively coupled plasma mass spectrometer (ICP-MS). Laser ablation settings were at 10 Hz repetition rate and 30 μm laser spot size, with an ablation depth of 2-7 μm (Chang et al., 2006; Kohn and Vervoort, 2008). Zircon age monitors used for calibration were Plesovice, FC-1, and 91500. The isotopic ratios of uranium and lead were used to calculate the zircon crystallization age, which were then placed on a concordia diagram in the ET_Redux program to evaluate potential lead loss (Bowring et al., 2012).

U-Th-Pb monazite dating

Dating of monazite by U-Th/Pb was undertaken using the Finnigan Element2 ICP-MS at Washington State University. Monazite crystals were initially examined and identified from polished thin sections using a JEOL 6010LA SEM-EDS and petrographic microscope at UNR. Samples were

ablated in-situ from polished thin-sections using a repetition of 5 Hz, at 3 J/cm^2 and a 12 micron spot size, following procedures from Chang et al. (2006) and Kohn and Vervoort (2008).

Silver Peak District Geologic overview

Mining history

Mineral Ridge gold deposits lie on the eastern edge of the Silver Peak Range, about 9 km northwest of the town of Silver Peak, and 12 km west of the Clayton Valley lithium brine fields. The Silver Peak mining district is subdivided into the Mineral Ridge and Red Mountain subdistricts. The Mineral Ridge subdistrict contains a cluster of small historic and modern mines that are the subject of the present study and characterized by Au-bearing milky quartz veins and lenses contained in highly deformed metamorphic rocks. In contrast, the Red Mountain subdistrict, located about 10 km west of Mineral Ridge, contains low-sulfidation epithermal Ag-Au- veins contained in Neogene volcanic rocks, notable mines of which include the Mohawk, Nivloc, and Sixteen-to-One (Bercaw, 1986; Cline, 1986). Silver deposits at Red Mountain were discovered in 1864, followed by discovery of the gold ores of the Drinkwater and Blair mines, which precipitated the building of a 30-stamp mill in the town of Silver Peak in 1867. These deposits were mined for two years, followed by years of idleness and intermittent mining by several operators (Spurr, 1906). The next surge of mining occurred in the years between 1933 and 1942 before shutting down during World War II (Albers and Stewart, 1972). During the pre-war mining era, the Drinkwater mine produced 600 tons of ore per day at an average head-grade of 10.3 grams per ton Au (Viljoen, 1996). In total, an estimated 406,000 ounces of gold were recovered from underground mining during the early history.

In 1989, Zephyr Resources Inc. began the open pit-mining era at Mineral Ridge, hauling ore 27 km down to the old 16-to-1 stamp mill in Silver Peak. Homestead Minerals Corp. acquired Zephyr in 1990 and continued mining until bankruptcy in 1992. A total of 113,000 oz Au were recovered from 1.4 Mt of ore during this period. An additional 112,000 oz Au were mined from 1993-2005 by Mineral Ridge Resources Inc., Vista Gold, and Golden Phoenix LLC from both open pit and underground mines. No production occurred from 2005-2011, until Golden Phoenix and Scorpio

Gold entered into the Mineral Ridge Gold LLC (MRG) joint venture and began production in 2011. In 2016, Waterton Global Resource Management purchased Golden Phoenix' 30% stake. MRG open-pit mined the historic Drinkwater and Mary deposits before moving outward to the Brodie, Wedge, Solberry, Bluelite, and Missouri satellite deposits. Following declining production, mining was suspended in November 2017. In total, MRG produced approximately 207,000 oz Au from 5.3 Mt of ore since 2011.

Geology

The Mineral Ridge area is largely underlain by variably metamorphosed Neoproterozoic through Cambrian siliciclastic and carbonate rocks of the Cordilleran miogeocline and coarse-grained granites of Mesozoic age (Figure 2). The sedimentary and metasedimentary rocks were originally deposited along the western North American continental margin following Neoproterozoic rifting (Dickinson, 2006). The Wyman Formation and Reed Dolomite form the lower plate of the Mineral Ridge metamorphic core complex (MCC), and thus represent lower crustal rocks that were exhumed in the Tertiary. These lower crustal metamorphic rocks occur below unmetamorphosed and unmineralized mixed siliciclastic-dominant-rocks of the Cambrian Deep Spring, Campito, and Harkless Formations, from oldest to youngest, respectively, which comprise the upper plate of the Mineral Ridge detachment. Although faulted, the order of lower- through upper-plate units is consistent with that observed in a normal, non-faulted stratigraphic succession (e.g., Stewart, 1970).

The Neoproterozoic Wyman Formation is the most widespread unit in the field area and is found throughout Esmeralda County and across the White and Inyo Mountains of California (Stewart, 1970), mostly as weakly metamorphosed argillite and phyllite. At Mineral Ridge, the Wyman Formation consists of metamorphic tectonites of dark brown carbonaceous and siliceous argillite, muscovite, chlorite, and calc-silicate schist and paragneiss, and blue-gray calcite marbles. Metamorphic grades of greenschist to lower amphibolite facies are recorded by chloritic phyllites, clinozoisite-bearing greenschist, biotite schist, and staurolite-garnet-muscovite schists. Complex interlayering with leucogranite is common with proximity to the roof of the Mineral Ridge pluton,

forming massive, foliation-subparallel bodies of highly deformed migmatite. Rocks of the Wyman Formation rest within the footwall of the Mineral Ridge metamorphic core complex and are strongly deformed, commonly with small-scale recumbent isoclinal folds verging northwest. Axial planes of isoclinal folds are sub-parallel or at low angles to the tectonic foliation in schists of the Wyman Formation, Cretaceous granitic intrusions, and quartz boudins. A minimum thickness of 2750 m was estimated for the thickness of the Wyman Formation in the White Mountains, California (Ernst, 1996). At Mineral Ridge, the exposed thickness of the Wyman Fm. excluding leucogranite sills was estimated to be approximately 340 m (Bailly, 1951). However, all basal contacts of the Wyman Formation at Mineral Ridge are with underlying Mineral Ridge pluton, and the base of the unit is not exposed.
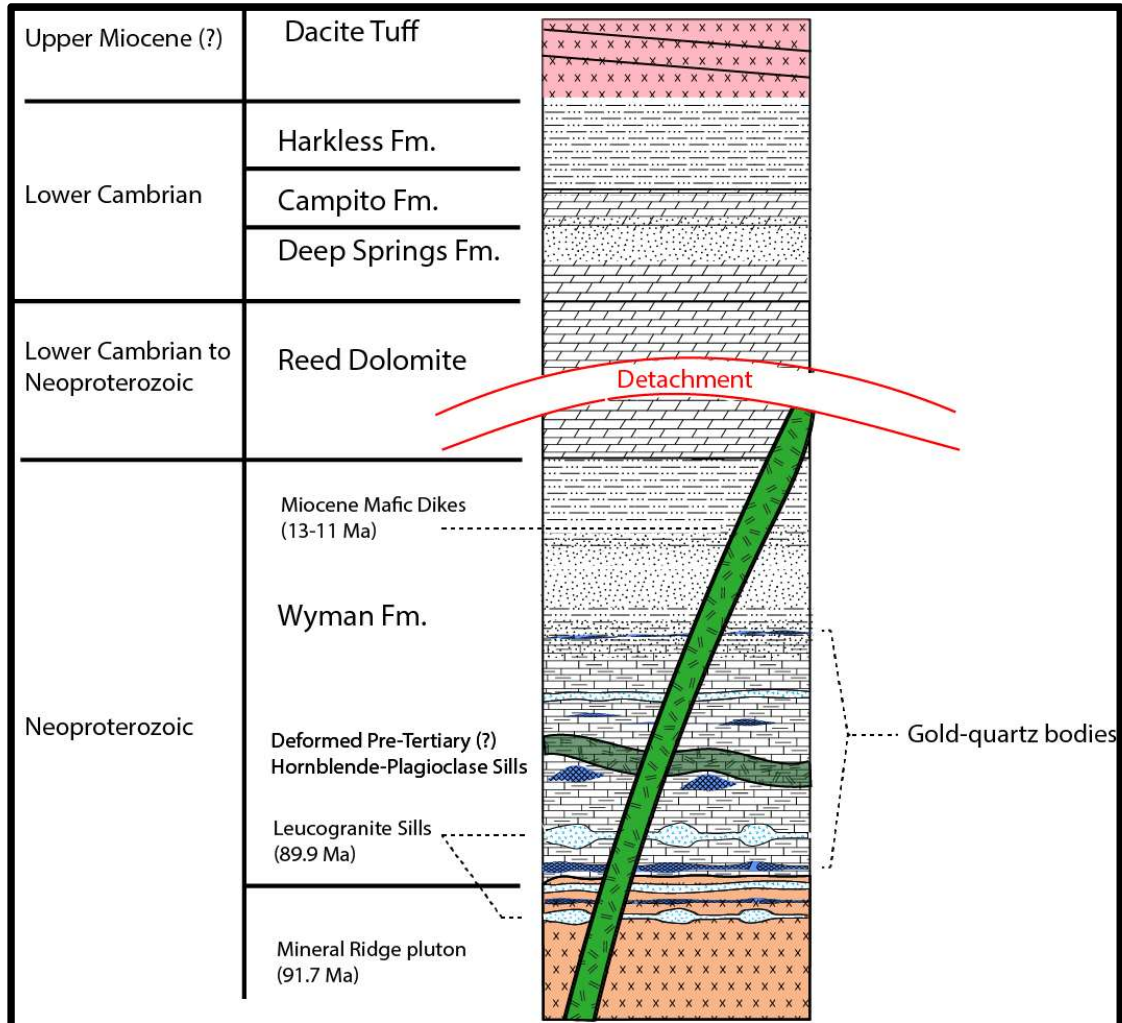
Figure 2. Stratigraphic column of the Mineral Ridge mine study area.

Above the Wyman Formation is the Lower Cambrian Reed Dolomite, the uppermost unit of

the lower plate in the Mineral Ridge metamorphic core complex that rests under the Mineral Ridge

detachment. The Reed lacks the strong tectonization seen in other units of the lower plate, and

ductile quartz bodies are rare. However, brecciation and metamorphism to dolomite marble with

strong calcite veining is locally present, especially in the eastern part of the mine site. This massive,

white to buff, fine- to coarse-grained dolomitic marble is estimated to be 650 m thick in the White

Mountains (Ernst, 1996), but has an estimated faulted thickness of ~300 m at Mineral Ridge (Bailly, 1951)

At least two phases of mafic intrusions occupy Mineral Ridge, Miocene hornblende-phyric andesite dikes, which cut tectonic foliation at high angles, and foliated pre-Tertiary diabase sills, which are oriented sub-parallel to foliation. The pre-Tertiary sills host ore in some locations (e.g., Drinkwater), and the high-angle Miocene dikes appear to entirely post-date gold mineralization, but locally are strongly altered to barren quartz-clay-pyrite-carbonate assemblages, indicating a post-gold hydrothermal event.

Upper-plate rocks in the complex are bounded from the metamorphosed lower plate by a shallowly north-dipping detachment fault (Oldow et al., 1994; Diamond and Ingersoll, 2002) that contains brittle fabrics and is broadly folded or domal in shape. Upper-plate sedimentary units in the study area consist of the Cambrian Deep Spring and Harkless Formations. The Deep Spring Formation consists of interlayered limestone and dolomite, with siltstone and sandstone. It is exposed in the study area as an isolated klippe of upper-plate rock in the southwest area of the mine site adjacent to the Brodie pit (Figure 3). The exposure sits above a several-meter-thick, chlorite-altered detachment surface marked by intense brecciation of both hanging wall and footwall rocks; a gently dipping Tertiary lithic-rich, welded rhyolite or dacite tuff caps the upper-plate sequence here. The Harkless Formation, composed of green-gray siltstones and quartzites, rests unconformably above the Wyman Formation, with the Reed Dolomite omitted by the detachment fault

The Mineral Ridge granite pluton intruded only the lower-plate of the MCC, and is a common host rock for gold mineralization. The intrusion is a peraluminous, two-mica granite with locally well-developed tectonic foliations, particularly at contacts with enclosing schist and paragneiss of the Wyman Formation. Interleaved in this two-mica granite as well as intruding Wyman strata are strongly lensoidal pegmatitic and gneissic leucogranite sills and lenses, composed of quartz, potassium feldspar, albite, muscovite, minor biotite, and accessory zircon and garnet. In

places, mingled leucogranite lenses, boudins, and veins with lit-par-lit texture are more abundant than metasedimentary rocks, and the rock is best termed migmatite. Thinner pegmatite lenses are commonly weakly foliated or laced with anastomosing shears that resulted in rounding and rotation of large crystals, whereas thicker sill-like bodies exhibit obvious shearing only on their margins.

Gold mineralization at Mineral Ridge is directly associated with abundant gray to milky white quartz veins, augens, boudins, pods, and lenses concordant with tectonic foliation in the Wyman Formation and granitic intrusions. Quartz veins at angles to the dominant foliation are commonly intensely folded and/or segmented. Au-bearing quartz veins are positively correlated with intensity of shear fabric, and Au-bearing veins are rare in rocks that do not contain strong foliation such as the massive interiors of thicker pegmatite. Pyrite, pyrrhotite, arsenopyrite, calcite, siderite, and fine-grained muscovite accompany the gold-bearing quartz lenses; less commonly, galena and sphalerite are indicative of the highest gold grades in quartz veins. The highest concentrations of Au-bearing quartz veins are found in the lower, ductiley deformed sections of the exposed Wyman Formation near intrusive contacts, both of granite and pre-Tertiary hornblende-plagioclase sills. Gold is primarily present as native gold and electrum in quartz, and as inclusions in pyrite. Gold grains generally range from 7-75 microns in size with gold to silver ratios ranging between 0.9 and 8, based on assay results and SEM-EDS analysis. High gold concentrations are associated with small amounts of base-metal sulfides and abundant ribbon-textured-quartz.

13

Figure 3. Generalized geologic map of Mineral Ridge study area, 1: 10,000. Locations of samples used for U/Pb dating inset with ages.

Tectonics

Cenozoic history

Structural relationships and thermal history of the Mineral Ridge area, in particular the mineralized lower plate, are complicated by late Cenozoic extension. Mineral Ridge lies within the Walker Lane, a seismically active zone of extension and transtension which accommodates approximately 20% of the dextral motion between the North American and Pacific plates (Faulds and Henry, 2008) since the late Miocene. Extension is most apparent along a major detachment at Mineral Ridge, where it juxtaposes Cambrian and younger strata in the hanging wall against deformed, metamorphosed, and mineralized Neoproterozoic to Cambrian metasedimentary strata, migmatites, and late Cretaceous and Miocene intrusions in the footwall. The chlorite-altered detachment fault has an elongate dome-shaped surface that coincides with the northwest-trending Mineral Ridge anticline. The Mineral Ridge anticline forms the topographic ridge of Mineral Ridge and continues northeast across the valley in the Weepah Hills (Diamond and Ingersoll, 2002). North- to northwest-striking high-angle normal faults cut the detachment fault and all units at Mineral Ridge.

Zircon and apatite fission-track dating from deformed lower-plate granitoids (Oldow et al., 1994) indicate the lower plate of the Mineral Ridge metamorphic core complex passed through ~200°C at 11.0 ± 0.7 Ma and ~100°C at 5.8 ± 0.5 Ma. However, K-Ar ages (Diamond, 1990) for trachyandesite welded tuffs (6.3 ± 0.5 Ma), which rest on the lower plate have an older age than the lower-plate apatite fission-track date. Due to the abundant late sericitic alteration in the Miocene diabase dikes, the apatite fission-track age may reflect late hydrothermal events, possibly related to the Silver Peak volcanism responsible for epithermal mineralization in the Red Mountain mining district (Keith et al., 1976; Cline, 1986).

Ingersoll and Diamond (2002) interpreted the fission-track data to show that the roof of the Mineral Ridge pluton was at depths of 9-18 km during early extension in the late-Miocene, based on an estimated geothermal gradient between 10-20°C/km; a higher gradient (~30°/km), as is the case

now, suggests burial depths in the late Miocene of ~7 km. Major activity on the Furnace Creek fault

system occurred during the late Miocene (Reheis et al., 1997) to the immediate southwest of

Mineral Ridge. The Furnace Creek fault system extends 250 km north from near Death Valley in

southeast California and ending in northern Fish Lake Valley west of the Silver Peak Range. Late

Miocene strain is thought to have transferred from the northern terminus of the Furnace Creek fault

to the central Walker Lane through a series of northeast-striking faults that link through shallow

northwest-dipping detachment faults at Mineral Ridge in the Silver Peak Range and Lone Mountain

to the northeast (Figure 4). This transfer-displacement system was shown by Petronis (2002) to

include clockwise vertical-axis rotation of the Silver Peak Range. Lower-plate rocks were at least

partially unroofed by the latest Miocene, based on K-Ar ages of trachyandesite welded tuff, which

overlap ages of detachment faulting, dated by Robinson (1968) and recalculated by Diamond (1990)

at 6.3 ± 0.5 Ma. These tuffs onlapped the exposed Reed Dolomite. Middle Miocene to Pliocene

extension in the Silver Peak area is also recorded by syn-extensional fluvial and lacustrine deposits

(Ridley and Diamond, 2000). Eutaxitic fabric in dacite tuffs near the Missouri mine record an

approximately 20 degree southeast-down tilt, which agrees with paleomagnetic data by Petronis

(2002).
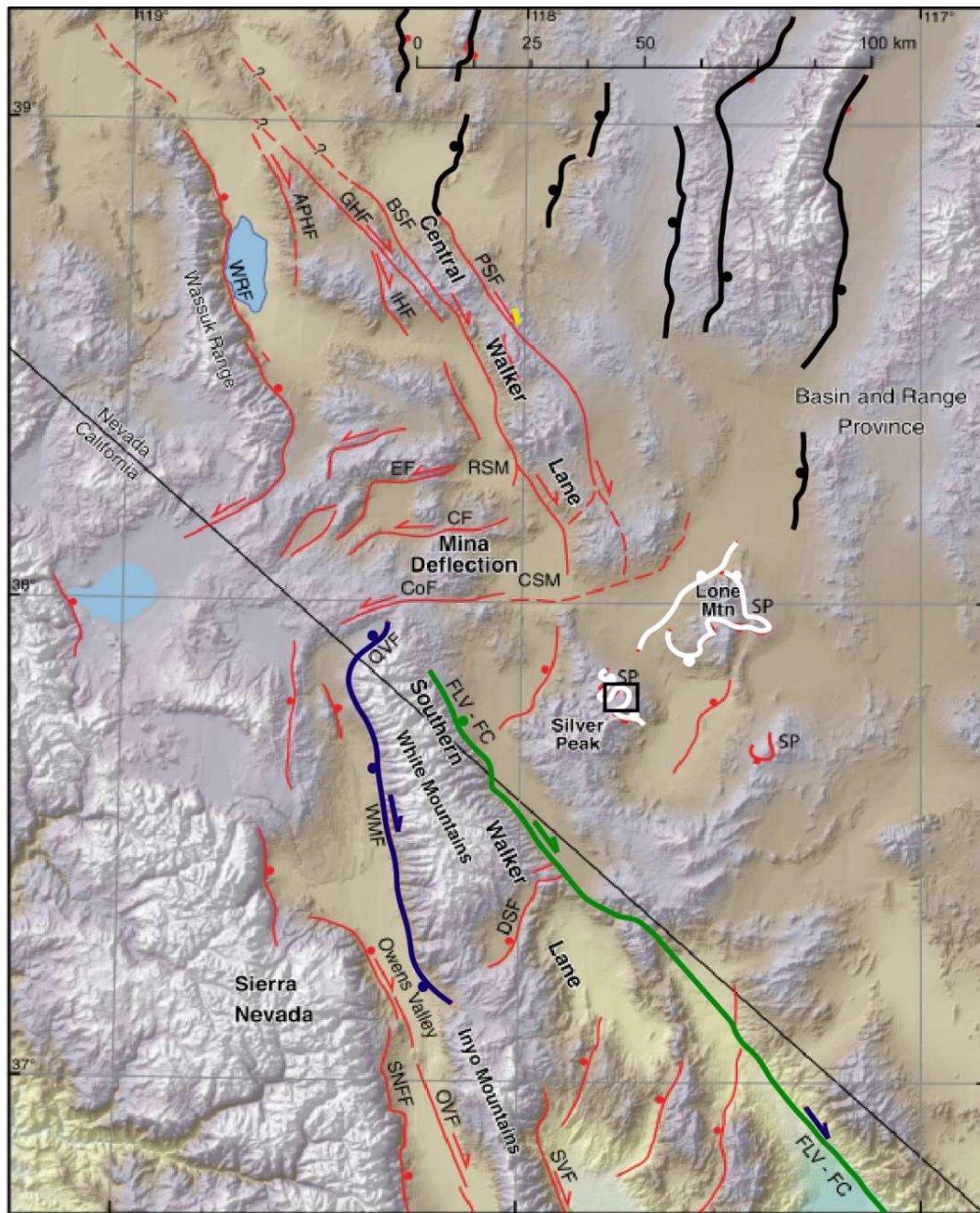
Figure 4. Study area within Cenozoic regional structural context.

Mineral Ridge (study area in black box) lies in a transition between the White Mountain shear zone (dark blue), Death Valley - Fish Lake Valley Fault (green), Walker Lane (red), and Basin and Range. Modified from Faulds and Henry (2008).

Prior to detachment faulting and exhumation, the incipient lower plate maintained deep crustal levels and high temperatures. This is recorded by the sizable difference between U-Pb zircon ages from this study, which indicate a Late Cretaceous (89.9 Ma) crystallization age for the Mineral Ridge pluton, and the Eocene cooling ages of K-Ar muscovite/biotite (Schilling, 1965) and Ar-Ar biotite (Diamond and Ingersoll, 2002) ages conducted by prior studies. Using the biotite closure temperature in the Ar-Ar system (Harrison et al., 1985), the lower plate passed through ~300-350°C at ~53 ± 1 Ma, approximately 36 m.y. after zircon crystallization in granites. Within this timeframe, a strong metamorphic foliation developed that is recorded in both Cretaceous granitoids and tectonized rocks of the Wyman Formation. Ingersoll and Diamond (2002) suggest this metamorphic fabric developed in response to the forceful emplacement of the Mineral Ridge pluton, as also hypothesized for Lone Mountain to the northeast (Albers and Stewart, 1972). However, we interpret the strong foliation in regionally metamorphosed rocks coupled with nappe-style folding to indicate mid-crustal exposures of contractional belts not local features related to pluton emplacement (e.g., Howard, 2003; Colgan et al., 2010).

The Silver Peak Range is situated at the convergence of several major tectonic domains (Figure 5), which include: a major flexural bend in the Neogene Walker Lane transtensional system, a probable western arm of Sevier hinterland fold-and-thrust deformation, and the leading edges of the Luning-Fencemaker, Golconda, and Antler contractional belts. Mineral Ridge falls on the western edge of a wide belt of Cordilleran metamorphic core complexes characterized by Jurassic to Eocene metamorphism, ductile deformation, two-mica granites and leucogranites, and major late Cenozoic low-angle extension (Miller and Bradfish, 1980; Lee et al., 2003). The Miocene extension and associated detachment faulting is the most pronounced and described feature at Mineral Ridge, in part because it is one of the youngest tectonic features and overprints older fabrics. However, Mesozoic contractional features, metamorphism, and intrusion are widespread at Mineral Ridge and

provide important information on the pre-Cenozoic tectonic history of the area, which bears on the

setting of gold mineralization.
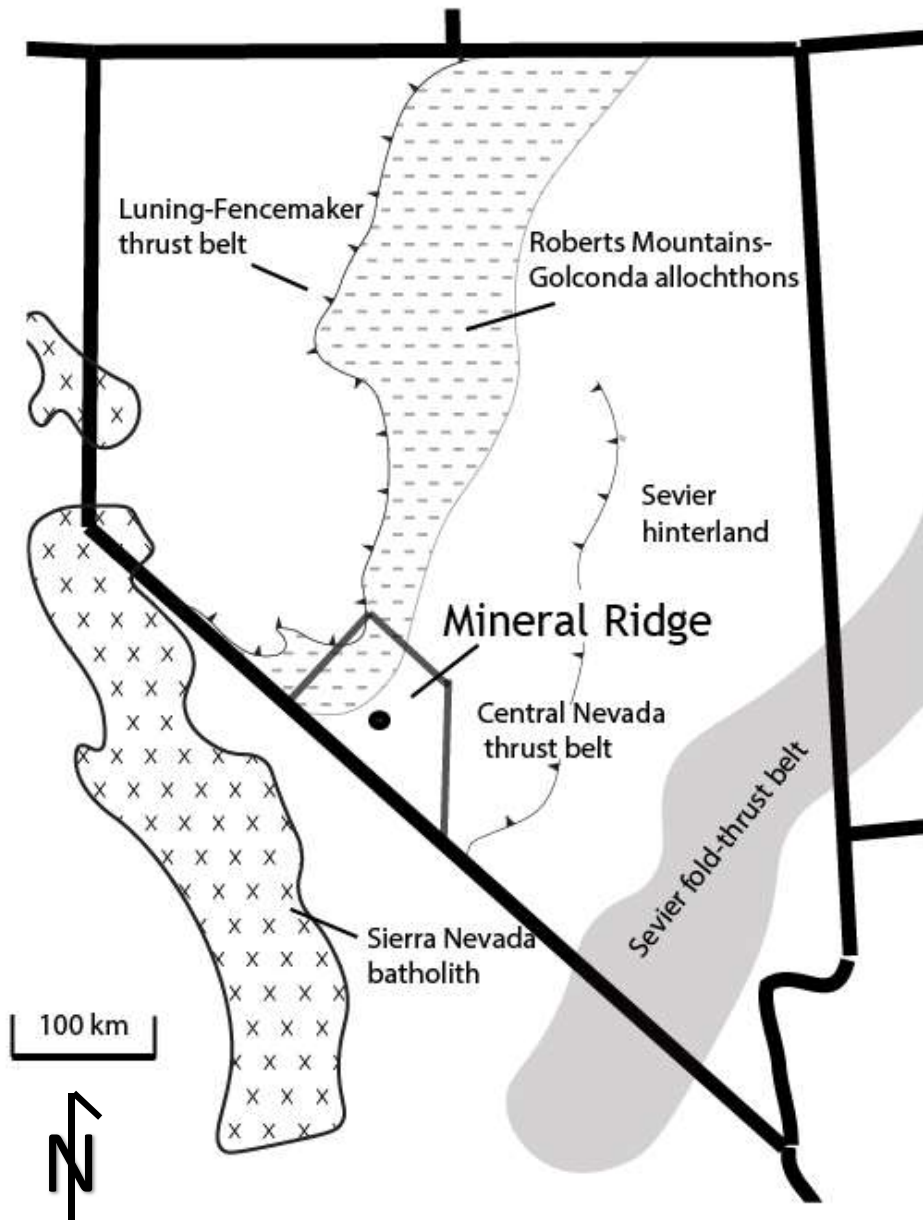
Figure 5. Major pre-Tertiary tectonic domains relevant to Mineral Ridge.

Pre-Cenozoic history

Neoproterozoic rifting of the western North American craton formed a westward-thickening passive continental margin sequence in which sedimentation occurred into the Devonian (Dickinson, 2006; Sillitoe, 2008). Following miogeoclinal deposition, transition to Farallon plate subduction in the Middle Jurassic triggered backarc magmatism, forming porphyry-copper and iron oxide-copper-gold deposits in Nevada (Barton et al., 2011). This was followed by Early Cretaceous retroarc thrusting in the Sevier belt and Late Cretaceous eastward migrating Laramide magmatism caused by a shallowing Farallon plate. The western Cordillera experienced widespread contractional deformation and associated crustal thickening in the hinterland during the Middle to Late Cretaceous Sevier orogeny. Deformation was likely due to flat-slab subduction, which eventually caused shutdown of arc magmatism by 80 Ma as Sevier east-vergent contractional deformation took hold (Yonkee, A.W., Weil, 2015). Large-scale contractional deformation in lower-plate rocks is apparent at Mineral Ridge in the ~300 m wavelength open F4 folds in Echo Canyon northwest of the Drinkwater mine (Figure 6), which are parallel to the orientation of the Mineral Ridge anticline, a large open anticline controlling the NE dip of ore bodies in the Drinkwater and Mary mines.

Figure 6. Large (300-m wavelength) open folds in Echo Canyon. Fold axes are subparallel to the Mineral Ridge anticline. View is to the north-northwest; Clayton Valley is to the right.

Similar NW-folding occurs in the White-Inyo Range located to the west of the Silver Peak Range, where a doubly-plunging anticlinorium cored by Wyman and Reed Dolomite Formations is intruded by peraluminous Late Cretaceous granites (Ernst, 1996) and deformed by a major Cretaceous transpressional shear zone (White Mountain shear zone) (Sullivan and Law, 2007), which is analogous to the timing and style of deformation at Mineral Ridge. The White Mountain shear zone is bracketed by the strongly deformed 91 Ma Pellisier Flats granitic pluton and undeformed 73 Ma Boundary Peak intrusion (Sullivan and Law, 2007). This fits with a well-established Late Cretaceous dextral transpressional setting in the western Great Basin-eastern Sierra Nevada. The Santa Rita, Gem Lake, and Sierra Crest shear systems in the east-central Sierra Nevada also trend NW-SE and contain mylonitic granitic rocks along rheologic boundaries (Greene and Schweickert, 1995; Tikoff and De Saint Blanquat, 1997; Saleeby, 2003).

In the White-Inyo Range, a consequence of Cretaceous Sevier deformation and crustal thickening is the 91.7 Ma peraluminous leucocratic and two-mica granites of the McAfee Creek series. This series of granites, similar in age and mineralogy to Mineral Ridge granites, were interpreted from highly radiogenic $^{87}Sr/^{86}Sr$ isotope values to be largely sourced from crustal melts (Miller and Gans, 1989). Ernst (1996) also interpreted the Late Cretaceous granites farther south in the White Mountains to derive from crustal melts of mid-crustal metasedimentary units, based on bulk-rock composition. Late Cretaceous peraluminous two-mica granites are found in a broad belt from Sonora Mexico to British Columbia, following the hinterland of the Sevier-Laramide thrust system (Miller and Bradfish, 1980). Peraluminous, garnet-bearing granite melts in this zone likely formed due to partial melting of overthickened crust from Jurassic-Cretaceous shortening, an elevated geotherm, strain weakening due to Jurassic through Late Cretaceous arc magmatism, and higher grades of metamorphism that prompted anatexis through dewatering and lowering of the solidus.

At Mineral Ridge, the mineralized 89.9 Ma Mineral Ridge pluton brackets the timing for major ductile deformation and the main gold event. Ductile deformation is recorded in Cretaceous granitoids by anastomosing micaceous foliation, local schistose fabric, which rarely grade into gneissic banding, and folded and boudinaged leucogranite sills. Similarly, Au-bearing quartz-carbonate-gold veins are deformed, recrystallized, and locally mylonitized (Figure 7). Contemporaneous upper-greenschist to lower-amphibolite facies metamorphism is recorded in the chlorite and muscovite (±garnet-staurolite) schists, which bound deformed granitic rocks, and in foliation-parallel crack-seal slivers of chlorite and muscovite derived from wallrock schist of the Wyman Fm. that occur in gold-bearing quartz lenses or boudins. Sevier prograde deformation and metamorphism at Mineral Ridge ended well before the earliest Eocene, when Ar-Ar biotite cooling ages indicate temperatures of <350° C that may reflect a stratigraphic burial depth of ~14 km (assuming a 25° C/km geothermal gradient) at the close of the Cretaceous due to early stages of lower-plate exhumation. This follows Miller and Gans' (1989) description of metamorphism in the hinterland of the Sevier belt in eastern Nevada (Figure 8) that occurred between ~90 and 70 Ma, coincident with muscovite-bearing granites and pegmatites likely generated at peak metamorphism.
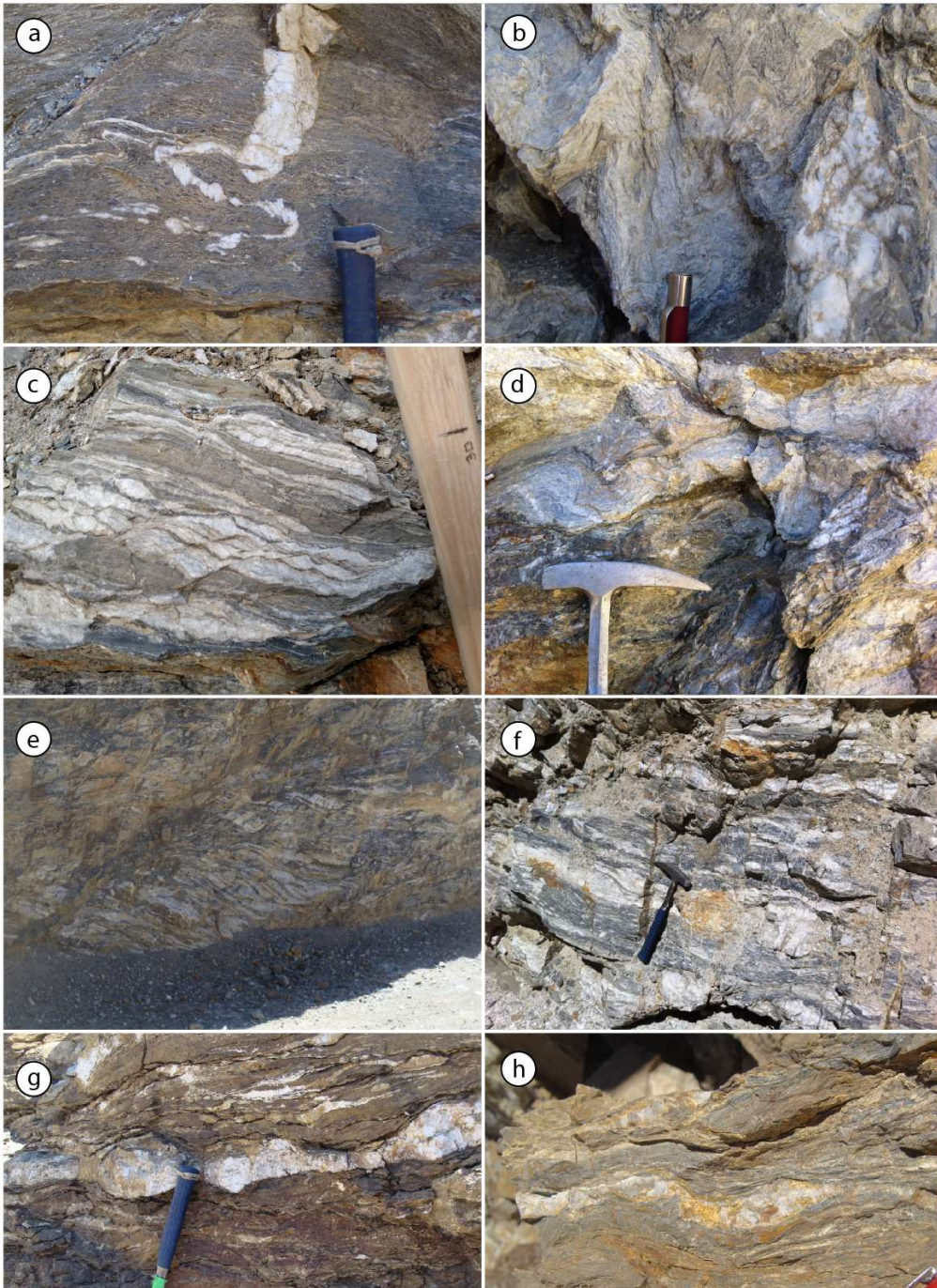
Figure 7. (a) Ptygmatic folding in quartz veins. (b) Chevron folding and pressure solution recrystallization in quartz. (c) S-C fabric development showing top to the north motion. (d) Crenulation folds. (e,f) Boudinaged metasedimentary-leucogranite migmatites. (g) quartz vein boudins in Wyman Fm. (h) cm-scale quartz boudinage in calcareous schist.
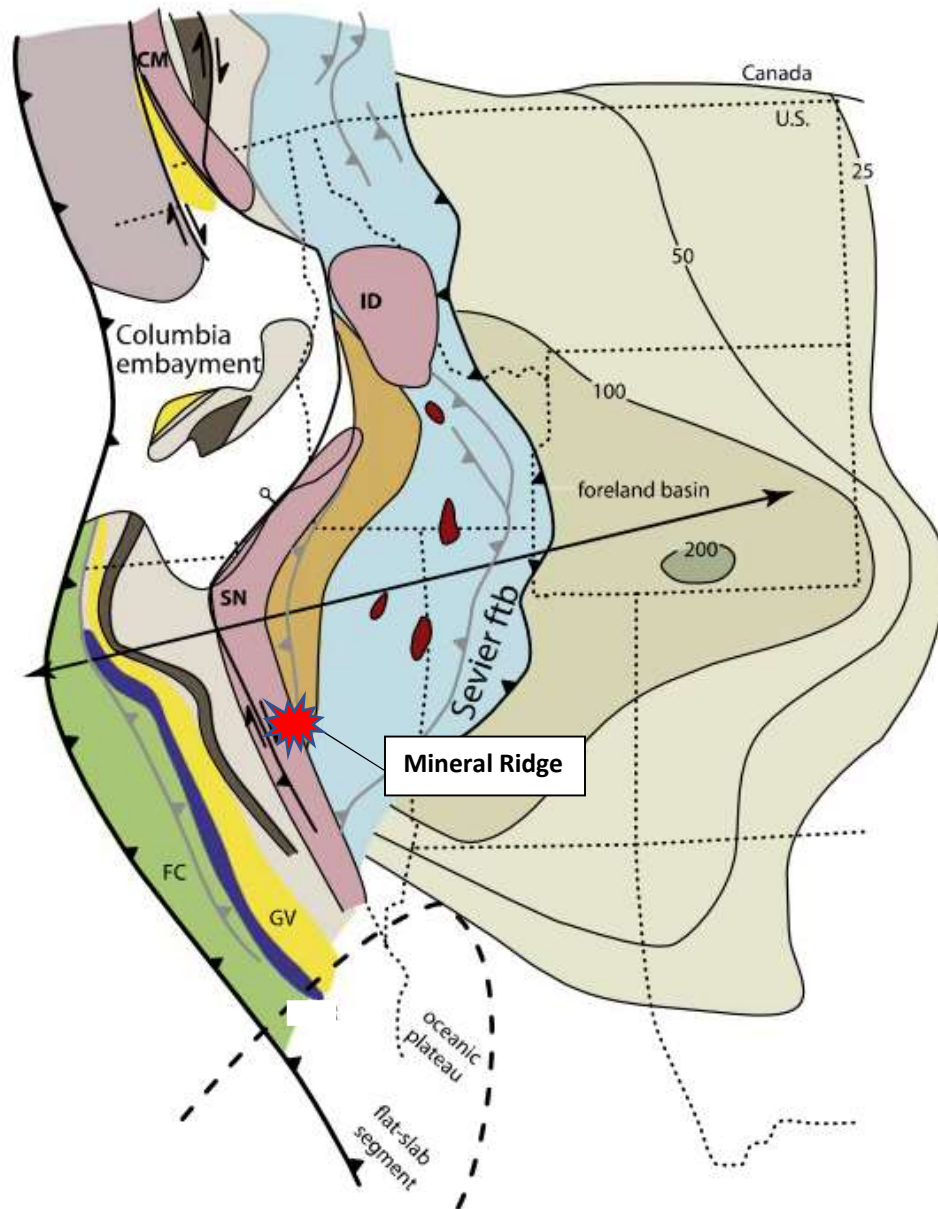
Figure 8. Palinspastic reconstruction of Sevier orogeny and associated deformation, from Yonkee and Weil (2015). Approximate location of Mineral Ridge within western-most Sevier fold and thrust belt, marked by red polygon. SN – Sierra Nevada batholith, GV – Great Valley, FC – Franciscan complex, ID – Idaho batholith, CM – Coast Mountains.

Igneous Geology

Background

Understanding the history and nature of the intrusions at Mineral Ridge is key to deciphering the complicated geologic history and genesis of gold mineralization. Magmatic-hydrothermal processes have long been considered responsible for mineralization at Mineral Ridge (Spurr, 1906; Bercaw, 1986; Noland et al., 2014), due to the proximity of granitic intrusions to productive ore zones. Because the layer-parallel leucocratic intrusions are cross-cut by gold-bearing quartz veins and have a similar sheared, boudinage texture, it is clear that main stage gold mineralization occurred after intrusion and formed either before or during ductile and/or brittle-ductile shear. To constrain the composition and timing of these felsic intrusive units, thin section and SEM petrography, litho-geochemistry, and Ar-Ar hornblende and U-Pb zircon geochronology were utilized in this study.

The lower-plate assemblage of Neoproterozoic to Cambrian metasedimentary clastic and carbonate strata is intruded by pre- to syn-deformational Late Cretaceous two-mica granite and pegmatitic leucogranites and hornblende-rich mafic sills, and post-deformation Miocene hornblende-rich intermediate dikes. The two-mica granites are exposed in a NW-trending area of roughly 2 km^2, along the hinge of the Mineral Ridge anticline. Observations made from the exposed granite north of Mineral Ridge to the canyons and drainages at the toe of the range near the pediment on the southeast end of the property, and in underground workings by Bailly (1951) and Bercaw (1986), suggest that a maximum of ~300 m thickness of metamorphic lower-plate rocks exist above the Mineral Ridge granite in the vicinity of the Mineral Ridge gold deposits. Beyond a ~1 km radius in all directions around the domal mass of Mineral Ridge, the collective sedimentary and metasedimentary cover above the Mineral Ridge granite is probably much greater. Two-mica granites are massive in shape and structure, which contrasts with the irregular bodies, sills, and dikes of the pegmatitic leucogranites. Tectonic foliation in the two-mica granites is more pronounced due to the consistent and relatively fine grain size and greater abundance of phyllosilicate minerals,

whereas the leucogranites often lack muscovite or biotite and contain coarse, equant crystals >5 cm diameter of feldspar and quartz. Strong shear foliation manifested by schistosity and asymmetric S-C fabrics occur in the mafic sills deep in the Drinkwater, whereas high-angle Miocene dikes are not foliated, despite their truncation by low-angle detachment faults.

Mafic Rocks

Two primary phases of mafic intrusions are observed in the Mineral Ridge area, Miocene hornblende-plagioclase diabase dikes and pre-Tertiary diabase sills. Miocene hornblende-rich diabase dikes crosscut the mineralized lower plate at high angles throughout the Mineral Ridge property and are the most abundant mafic intrusion in the study area. Pre-Tertiary diabase sills lie sub-parallel to bedding in the Wyman Formation and display a distinct S-C fabric not seen in Tertiary mafic dikes (Figure 9). In one location at the bottom of the Drinkwater pit, gold-bearing quartz veins occur along foliation in pre-Tertiary mafic sills, indicating that the sills were emplaced prior to mineralization. Except for this one occurrence, mafic intrusions at Mineral Ridge examined during this study are devoid of ore. Mineralogically both series of mafic intrusions are similar, hornblende phenocrysts up to 2 cm in length set in a plagioclase matrix. However, the pre-Tertiary sills contain minor amounts of pyroxene not found in Miocene dikes. Geochemically, both are medium- to high-K calc-alkaline series diabase intrusions (Figure 10).

Figure 9. Textures and relationships of pre-Tertiary diabase sills.

(a) S/C fabric developed in pre-Tertiary diabase. (b) Lit-par-lit texture in foliated mafic sills cutting leucogranite. (c) Brecciated and foliated diabase sill with mineralized (12.7 ppm Au) boudinaged quartz lens. (d) Boudinaged Fe-rich quartz body in pre-Tertiary hornblende-plagioclase sill.

Miocene hornblende-plagioclase dikes cut lower-plate stratigraphy, generally at angles greater than 50 degrees and up to sub-vertical, striking S35°W and dipping to the northwest. Dike

widths average about one meter, with a planar to slightly undulatory shape. Black to dark green, competent and crystalline cores grade out to pale to olive green friable margins. A post-gold hydrothermal alteration event is manifested by alteration of hornblende and plagioclase to smectite and/or sericite, chlorite, and calcite. Calcite and late, barren quartz veins cut altered dikes. In altered mafic dikes, pyrite, clay, and weathering-related iron oxide are ubiquitous. Miocene dikes show higher degrees of alteration and weathering, possibly because the high-angle dikes cut stratigraphy and foliation and provided conduits for late hydrothermal fluids. Alternatively, these dikes were originally glassy and were more susceptible to clay alteration on weathering and hydrothermal alteration. At the Brodie mine, clay-pyrite alteration in the Miocene dikes is much more extensive, and dikes are completely bleached and friable masses of swelling clays, pyrite and iron oxides, and quartz, with anomalous gold values reaching 26 ppb. As mentioned by Bercaw (1986), this end of the Mineral Ridge area contains brecciated "epithermal"-textured ores unlike the foliation-parallel milky quartz veins that typify the rest of Mineral Ridge and may be related to Neogene epithermal mineralization that occurs at the nearby Sixteen-to-One and Nivloc mines in the Red Mountain subdistrict. Ore-grade samples (MR1637, MR1618, MR1727) were recovered from a heavily gossanous, brecciated zone at the south end of Brodie pit. This younger, probably Miocene hydrothermal event, is the likely cause for the strong sericitic alteration in mafic dikes from the southwest area of Mineral Ridge.
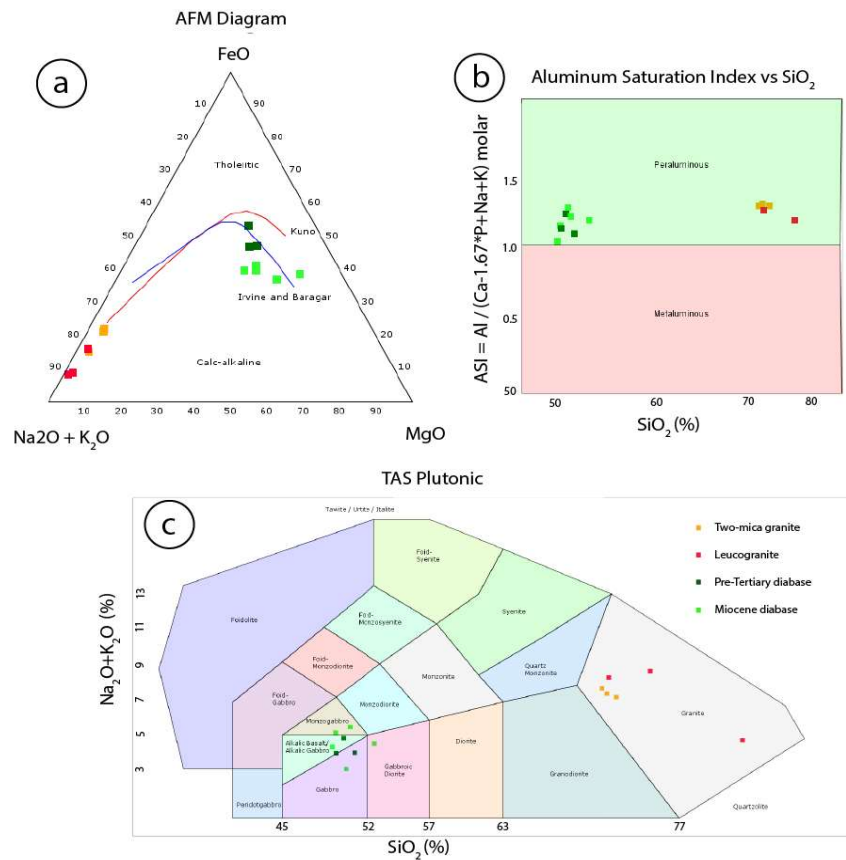
Figure 10. Geochemical classification diagrams for unaltered intrusions at Mineral Ridge.

A) Alkali-FeO-MgO (AFM) diagram showing calc-alkaline affinity of all igneous intrusions (From Irvine and Baragar, 1971). B) Aluminum saturation index (ASI) vs. SiO$_2$ (From Frost and Frost, 2008).C) Total alkalis -silica plutonic classification diagram (From Middlemost, 1994).

Pre-Tertiary diabase sills follow metamorphic foliation and dip shallowly, up to approximately 30 degrees, and although mineralogically very simple and similar to Miocene dikes, have a distinct tectonic foliation and lit-par-lit injection textures. These textures suggest magma migration along metamorphic foliation, and therefore a syn-tectonic timing. Gold-bearing quartz augens are found within and along the margins of foliated sills (Figure 9d). Pre-Tertiary mafic dikes share a simple mineralogy of variably sized hornblende phenocrysts in a very fine-grained, granular matrix of plagioclase with sparse secondary pyrite and chlorite. Pre-Tertiary diabase sills locally grade into chlorite schist with mm-scale shear bands and quartz augens. Greenschist sills react strongly to HCl and contain up to 11.4% CaO, in both calcic plagioclase as well as secondary

carbonate. Cross-cutting relationships show mafic sills cutting and being cut by Late Cretaceous granitic intrusions, suggesting mantle-derived diabase magmas were intruded during emplacement of the granite.

A third, undeformed and relatively more mafic intrusion dissimilar to hornblende-rich dikes and sills is a pyroxene-plagioclase diorite that crops out at the Bluelite mine at the northwest end of the mine site. This intrusion has a more massive geometry than the dikes and sills of diabase elsewhere and is of unknown age. The hydrothermally altered intrusion is composed of graphic mm-sized plagioclase and pyroxene, abundant 0.3 mm arsenopyrite, and some interstitial calcite growths.

Felsic Rocks

The Mineral Ridge pluton is composed of peraluminous two-mica granite, which is closely associated with coarse-grained to pegmatitic muscovite-bearing leucogranite sills and lenses concentrated in roof rocks above the pluton composed of banded biotite schist and paragneiss of the Wyman Formation. Granites at Mineral Ridge are restricted to the lower plate of the Mineral Ridge detachment. Granitic intrusions are peraluminous based on modal mineralogy, which includes major plagioclase and alkali feldspar, quartz, muscovite, and biotite, but also significant garnet, and rare topaz. The granites are also peraluminous based on the alumina saturation index (Figure 10), defined as the ratio of molar alumina to alkali elements (Al / (Ca-1.67*P+Na+K) exceeding 1.0 (Frost and Frost, 2008). Moving inward into the pluton away from its roof, the two-mica granites appear to inhabit the core of the Mineral Ridge anticline, grading upwards towards a dominance of leucogranites that texturally range from aplite to pegmatite. The leucogranites, locally referred to as alaskites after the usage of Spurr (1906), are gradational with the primary two-mica granite phase and are more commonly expressed in cm to tens of meter-scale-long veins or lens-shaped bodies, boudins, and small, irregular apophyses from the more massive two-mica granite bodies. Both felsic intrusions are concordant with wallrock foliation and migmatite layering. Felsic intrusions of the Mineral Ridge pluton are silica-rich (71-75% SiO_2), moderately to strongly peraluminous (alumina

saturation index 1.1-1.3), and alkali-rich, containing between 7.3 and 9.6% $Na_2O + K_2O$. On the plot of total alkalis-silica (TAS) (Middlemost, 1994), leucogranites plot well into the granite field (Figure 10). Feldspar-poor leucogranite bodies show silica values up to 82% with relatively strong depletions in $Na_2O + K_2O$ compared with two-mica granite. Some strongly altered leucogranites show an opposite trend of very low silica, that may be reflecting intense leaching and silica removal (e.g., ~63% SiO_2) and increases in alkalis elements, although this too may reflect difficulty in obtaining representative bulk analyses from such coarse-grained rocks.

A chondrite-normalized rare-earth element diagram (Figure 11) defines strong differences between the texturally and chemically homogenous two-mica granite and heterogenous and pegmatitic leucogranite. Two-mica granites show consistent steep negative slopes with light REEs ranging from 10-110x chondrite that are similar to the patterns of arc granites; heavy-REEs are only 2-10x chondrite, with least enrichment among the heaviest rare earths. Two-mica granites show a consistent slight negative Eu (and Sm) anomaly. In contrast, leucogranites display a wider spread of REE concentrations due to the heterogeneity of the unit in grain size and composition, from silica-rich to silica-poor and variably garnet-bearing. The leucogranite trend defines a significantly shallower negative slope than two-mica granites, with a strong negative Eu anomaly, weak enrichments in light-REEs (8-40x chondrite) and higher values of heavy REEs (4-9x chondrite). The depletion of heavy-REEs in non-garnet-bearing samples suggests that HREEs were concentrated in a garnet-bearing restite source, e.g., a source amphibolite or granulite, or garnet was fractionated from the melt.
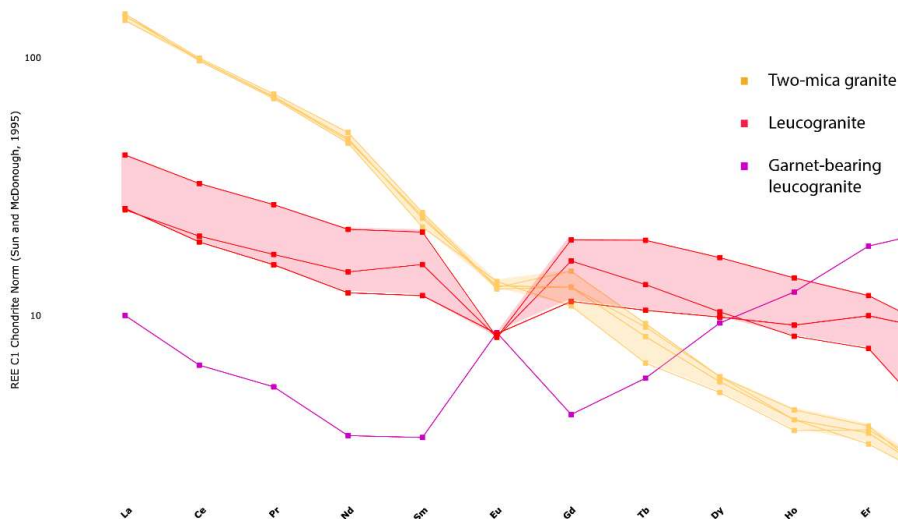
Figure 11. Chondrite-normalized rare-earth diagram of Mineral Ridge two-mica granite and pegmatitic leucogranites.

Two-mica granites are characterized by strongly foliated to gneissic textures defined by magmatic muscovite and biotite (~10-35% by mode) in a medium-grained, equigranular groundmass composed primarily of undulatory clear to gray quartz (30%), plagioclase (40%), and orthoclase and microcline (20%). Minor phases observed in thin section include calcite, magnetite with exsolved ilmenite, biotite locally replaced by chlorite, garnet locally replaced by chlorite and/or biotite, apatite, zircon, and sphene, with pyrite and chalcopyrite of probable secondary origin. Foliation varies from nil to schistose and gneissic (Figure 12), the latter occurring with inclusions of metasedimentary wall rock near the roof of the pluton. Locally, the foliation is planar and transposed in mylonitic granite (Figure 13). Lit-par-lit fabrics are abundant near contacts between roofs of intrusions and enclosing rocks of the Wyman Formation. Near the hinge of the Mineral Ridge anticline, two-mica granites commonly lack foliation and were likely at deeper levels prior to erosion in the anticline core. Quartz-hosted fluid inclusions in two-mica granite are very abundant but small (generally ≤15 µm), rich in vapor (>30%), have strong euhedral to subhedral negative

crystal shapes, CO_2-rich, and were low-salinity based on the absence of halide daughters. Fluid inclusions in foliated granites are similar to those in Au-bearing quartz veins **(**Appendix C-1**)**.
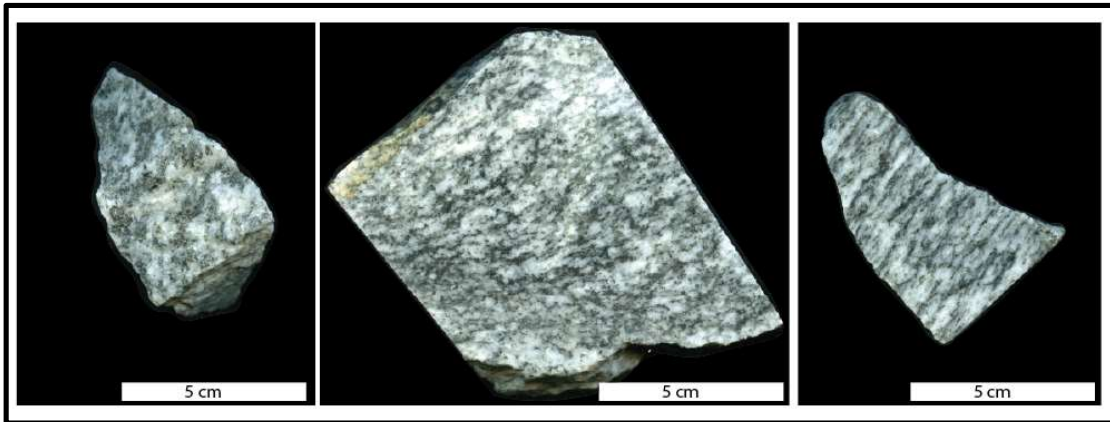
Figure 12. Progressive foliation development of two-mica granite from the Mineral Ridge pluton, from least-foliated (left) to strongly foliated (right).

Leucogranites of the Mineral Ridge area are composed of a strongly heterogeneous mixture of coarse grained to commonly pegmatitic primary minerals that include undulatory, anhedral gray to blue-gray quartz, myrmekite, microcline (1->20 mm), muscovite (to >15 cm dia.), uncommon biotite (to >5 cm dia.), and garnet and rare beryl; chlorite, calcite and muscovite after plagioclase; chalcopyrite, and pyrite are minor secondary minerals. Muscovite content in pegmatites varies in volume from ~0 to 30%. Large pinch and swell veins of milky white to gray quartz are common in leucogranites, which are correlated with the top of the Mineral Ridge pluton in a zone of intense shearing.

Figure 13. Mylonitic leucogranite migmatite sample from Custer Canyon area. Quartz-potassium feldspar (stained yellow with sodium cobaltinitrite) augens and planes of attenuated quartz, lit-par-lit with pre-Tertiary diabase.

Leucogranites are interlayered with chlorite and muscovite schists in lit-par-lit injection textures and boudinaged lenses of leucogranite within larger bodies of tectonized marble (Figure 14a). Strong shearing of leucogranite migmatite locally forms strongly foliated, even mylonitic bodies several meters thick at the top of the Mineral Ridge pluton. The volume of leucogranite migmatite decreases with distance from the roof of the pluton. Deformation conditions were above quartz plasticity of ~300°C, and bulging quartz recrystallization textures in thin section and undulose extinctions suggest minimum temperatures closer to 340°C (Stipp et al., 2002). Common fine-grained, blue-gray, quartz-rich clots and veins (**Error! Reference source not found.**b**)** emanate from the leucogranite bodies and cross cut two-mica granites, but are barren of gold or silver and do not have a clear spatial relationship to milky-white gold-bearing quartz. These blue-gray quartz veins decrease in feldspar content within tens of meters distance from the Mineral Ridge pluton, but unlike mineralized quartz veins, commonly contain books of euhedral muscovite and thus, are pegmatite-associated. Pegmatites at Mineral Ridge tend to grade in out of quartz-rich veins, ranging

from 71% to 82% silica in unaltered samples; silica drops to ~63% silica in altered samples where

plagioclase and orthoclase precipitated at the expense of quartz at high-temperatures. All unaltered

two-mica and leucogranite samples assayed below detection limits of 1 ppb Au.
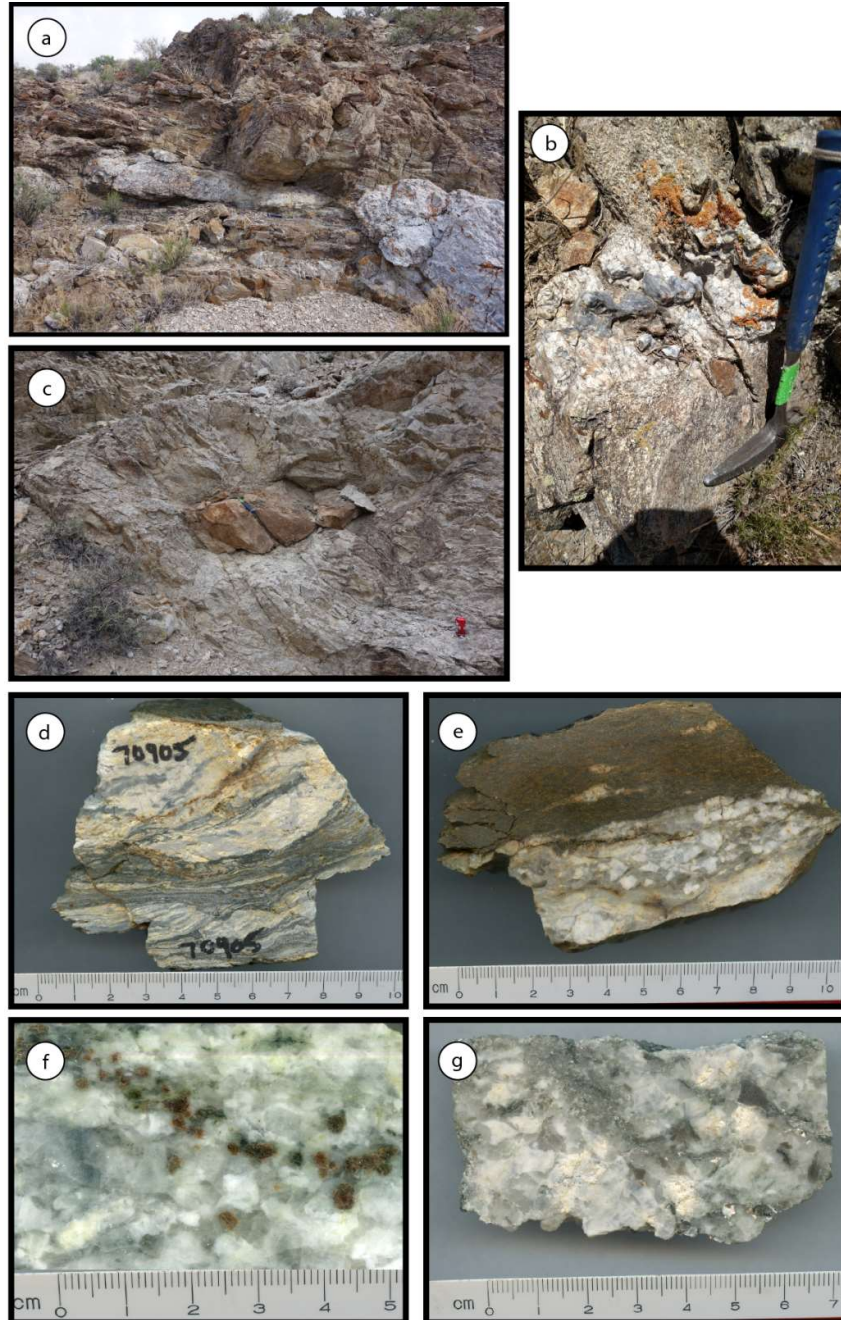
Figure 14. Field relationships and textures of leucogranite intrusions.

*(*a) Boudinaged leucogranite intrusion at Wyman (top) and Reed Dolomite (bottom) contact. (b) Leucogranite pod with gold-barren blue-gray quartz lens in two-mica granite. (c) Reed Dolomite boudin in mixed two-mica granite and leucogranite body, 12 oz can for scale. (d) Severely attenuated leucogranite migmatite. (e) Contact with Wyman schist, with leucogranite inclusions. (f) Garnet-rich leucogranite. (g) Typical leucogranite texture.

Igneous Geochronology

Previous studies have employed various isotopic methods for dating the Mineral Ridge granitoids with highly variable results (Table 1). Potassium-argon analysis of muscovite and biotite from the Mineral Ridge pluton (Albers and Stewart, 1972); Schilling, 1965) returned recalculated ages (Steiger and Jager, 1977) of 51 ± 2 Ma and 42 ± 2 Ma, respectively. These dates were supplemented by later $^{40}Ar/^{39}Ar$ stepwise-heating of biotite (Diamond and Ingersoll, 2002), which produced ages of 53 ± 1 and 55 ± 2 Ma. However, due to the complex thermal history at Mineral Ridge associated with exhumation of the once deeply buried lower plate of the metamorphic core complex, and the relatively low resetting temperatures of biotite and muscovite (300-400°C), these ages are regarded as cooling ages and clearly not the magmatic ages of granitic rocks. As an alternative to low-temperature resetting of micas, this study employed U-Pb zircon analysis to obtain crystallization ages of the Mineral Ridge pluton. Zircon closure temperatures are approximately 750°C, and thus are more likely to retain radiogenic lead despite later thermal events like high-temperature metamorphism. From the zircon dating, a Late Cretaceous age was determined for the Mineral Ridge two-mica granite and leucogranite, which is similar to ages for other peraluminous plutons in the area; including a Rb-Sr whole rock (Bohlke and Kistler, 1986) age of 86 Ma for the Lone Mountain pluton to the east, and 91 Ma age (Sullivan and Law, 2007) for the Pellisier Flats pluton to the immediate west in the White Mountains, California.

Further radiometric age determinations for the Mineral Ridge metamorphic core complex detail post-metamorphism and -mineralization intrusions, and likely exhumation ages. Hornblende-plagioclase dikes, which crosscut mineralized lower-plate metamorphic strata, were dated by whole rock $^{40}Ar/^{39}Ar$ stepwise-heating (Petronis, 2002), with resulting cooling ages of between 12-10 Ma. Hornblende Ar-Ar stepwise-heating ages obtained by this study targeted foliated, quartz vein-bearing hornblende-plagioclase sills, which run semi-concordant with tectonic foliation produced a non-isochron age of 22.10 ± 0.26 Ma. Due to cross-cutting relationships and the non-isochron spectra, this age is interpreted as a Miocene thermal reset rather than a post-mineral intrusion.

Table 1. Radiometric ages of Mineral Ridge lower-plate rocks. Asterisks denote dates interpreted as cooling ages.

Method	Mineral	Unit	Source	Age	Approximate closure temperature
Rb-Sr	Lepidolite	Two-mica granite	Schilling, 1965	700 Ma	-
U-Pb	Zircon	Two-mica granite	This study	91.7 ± 0.34 Ma	900-750°C
U-Pb	Zircon	Leucogranite	This study	89.9 ± 0.53 Ma	900-750°C
U-Pb	Monazite	Quartz vein	This study	76.0 ± 1.8 Ma	900-720°C
Ar-Ar	Biotite	Two-mica granite	Diamond and Ingersoll, 2002	55 ± 2 Ma *	300°C
K-Ar	Muscovite	Two-mica granite	Albers and Stewart, 1972	51 ± 2 Ma *	350°C
K-Ar	Biotite	Two-mica granite	Albers and Stewart, 1972	42 ± 2 Ma *	300°C
Ar-Ar	Hornblende	Pre-Tertiary diabase (?)	Petronis, 2002	50.0 ± 1.0 Ma *	450-500°C
Ar-Ar	Hornblende	Pre-Tertiary diabase (?)	Petronis, 2002	26.4 ± 2.2 Ma *	450-500°C
Ar-Ar	Hornblende	Pre-Tertiary diabase	This study	22.1 ± 0.13 Ma *	450-500°C
Ar-Ar	Groundmass	Miocene diabase	Petronis, 2002	12.4 ± 1.9 Ma *	~250°C
Ar-Ar	Groundmass	Miocene diabase	Petronis, 2002	11.6 ± 0.4 Ma *	~250°C
Ar-Ar	Groundmass	Miocene diabase	Petronis, 2002	11.4 ± 0.6 Ma *	~250°C
Ar-Ar	Groundmass	Miocene diabase	Petronis, 2002	11.3 ± 0.2 Ma *	~250°C
Ar-Ar	Groundmass	Miocene diabase	Petronis, 2002	10.9 ± 0.3 Ma *	~250°C
Ar-Ar	Groundmass	Miocene diabase	Petronis, 2002	10.5 ± 0.8 Ma *	~250°C
Fission track	Zircon	Felsic intrusive	Oldow, 1994	11.0 ± 0.7 Ma	200°C
Fission track	Apatite	Felsic intrusive	Oldow, 1994	5.8 ± 0.5 Ma	100°C

Granitic rocks selected for U-Pb zircon analysis (Figures 15, 16, 17, 18) were collected from an unaltered portion of granite exposed in the highwalls of the Brodie and in Drinkwater pits at Mineral Ridge (Figure 3). Cathodoluminescence imaging (CL) shows complex zircon morphology in the two-mica granite and severe uranium damage in the pegmatite, indicating a multi-stage thermal history and inherited grains in the two-mica granite, and excess original uranium (metamictization) in the pegmatite (Corfu et al., 2003). Nonetheless, both units returned interpretable ^{207}Pb/^{206}Pb ages. Zircon crystals from the leucogranite and two-mica granite are approximately 100 microns in diameter, with abraded and fractured xenocrystic cores in the two-mica granite generally 25-50

microns in diameter. Out of 75 zircon grains examined under CL for xenocrystic grains, 41 grains had

clear inherited cores with complex zoning, 23 had well-developed oscillatory zoning indicative of

igneous derivation, and 11 grains were ambiguous or exhibited metamict damage. Due to the

metamictization, no xenocrystic cores were observed from the leucogranite zircons under CL. Purely

igneous zircons with euhedral growth zonation and no inherited cores were also observed and

analyzed from the two-mica granite population (Figure 15).
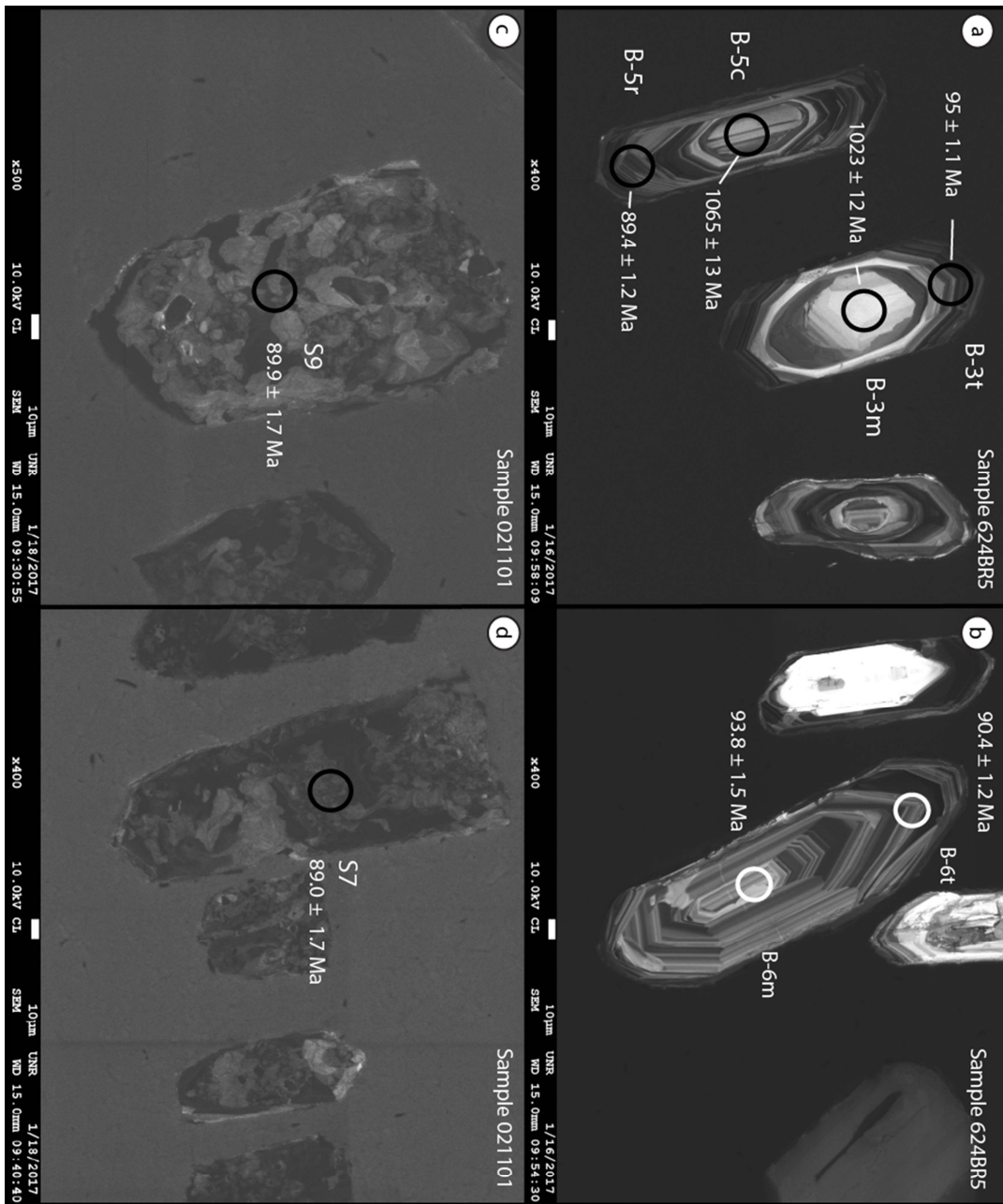
Figure 15. SEM cathodoluminescence images of zircons from two-mica granite (a,b) and leucogranite (c, d).

A majority of zircons from the two-mica granite contained inherited or xenocrystic zircon cores (a), although primary igneous crystals were also present (b). All leucogranite zircons show strong radiation damage (metamictization) and no apparent zoning or xenocrysts (c,d).

Zircons from two-mica granite sample 624BR5 (Brodie pit) yield a weighted mean $^{206}Pb/^{238}U$ age of 91.7 ± 0.34 Ma (2σ) for 21 of the 36 analyses. This includes both well-zoned core and rims as well as igneous zircon rims on inherited cores. Three inherited cores gave $^{206}Pb/^{238}U$ ages of greater than 1 Ga (1023 ± 12 Ma, 1089 ± 15 Ma, and 1426 ± 17 Ma), and five cores returned Jurassic ages with a mean of 167.9 ± 1.1 Ma. The Jurassic ages are consistent with inheritance from widespread Jurassic intrusions in the region, part of the Sierra Nevada batholith. Of the 21 zircons giving Late Cretaceous ages, the youngest individual age is 86.5 ± 1.5 Ma and the oldest is 101.5 ± 1.7 Ma.

Metamict zircons from leucogranite pegmatite sample 021101 (Drinkwater pit) yield a weighted mean $^{206}Pb/^{238}U$ age of 89.91 ± 0.53 Ma (2σ) for 11 of the 23 analyses. One grain interpreted to be inherited gave a $^{206}Pb/^{238}U$ age of 130.8 ± 2.5 Ma. Excluding the inherited outlier analysis, $^{206}Pb/^{238}U$ ages from 22 grains range from 105.3 ± 2.1 Ma to 82.6 ± 1.3 Ma. No inherited zircons were identified or analyzed in the leucogranite.
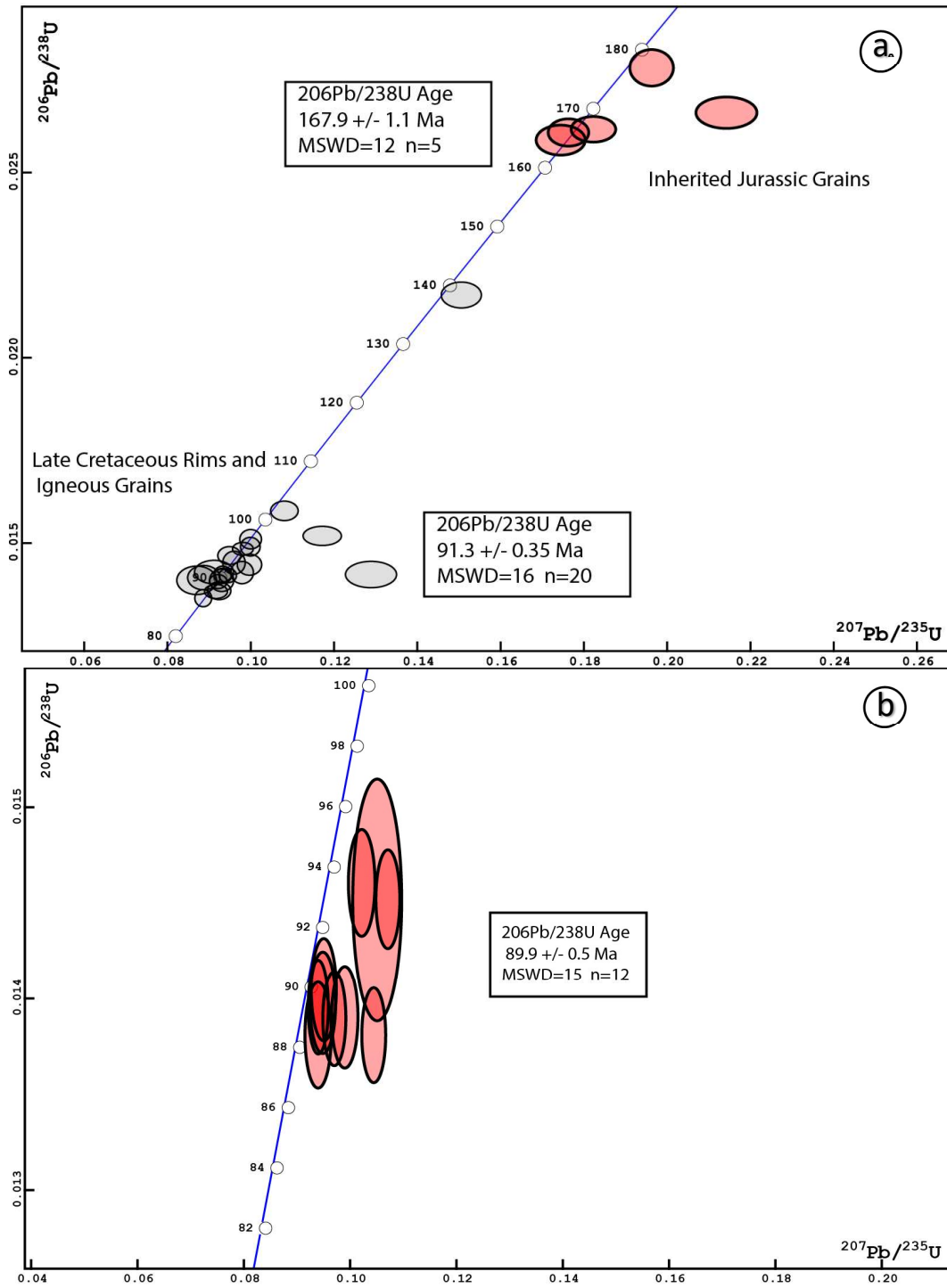
Figure 16. [206]Pb/[238]U vs. [207]Pb/[235]U concordia diagrams for two-mica granite (a) and leucogranite pegmatite (b). Two populations of zircon ages in two-mica granite sample 624BR5; inherited Jurassic cores and Late Cretaceous crystals or rims.

Because the weighted mean ages for both granitic units are within 2 m.y. of one another, at least two explanations are possible: 1) leucogranite pegmatite is the result of late crystallization of the muscovite-biotite granite, and therefore should have an age essentially the same as the two-mica granite and 2) an earlier age, most likely Jurassic, marks the true crystallization age for both granitic units, and the latest overprint age records a sustained high-temperature (>750° C) metamorphic event consistent with the near-gneissic texture in the two-mica granite and the boudinage in the leucogranite. The former interpretation is favored as most geologically reasonable, as Proterozoic and Jurassic cores were measured in several zircons. Zoning patterns and euhedral crystals strongly suggest an igneous rather than metamorphic zircon formation, and all analysis of zircon rims return Late Cretaceous dates, so our hypothesis is that the ages stated above reflect the main igneous crystallization age. The extended individual zircon crystallization ages (Figure 17), which in the two-mica granite ranges from ~97 to 86 Ma, and in the leucogranite pegmatite from ~97 to 83 Ma, suggest an extended period at elevated temperatures. We interpret this to represent a slow cooling or progressive crustal melting at depths likely below ~15-20 km. Magmatic muscovite
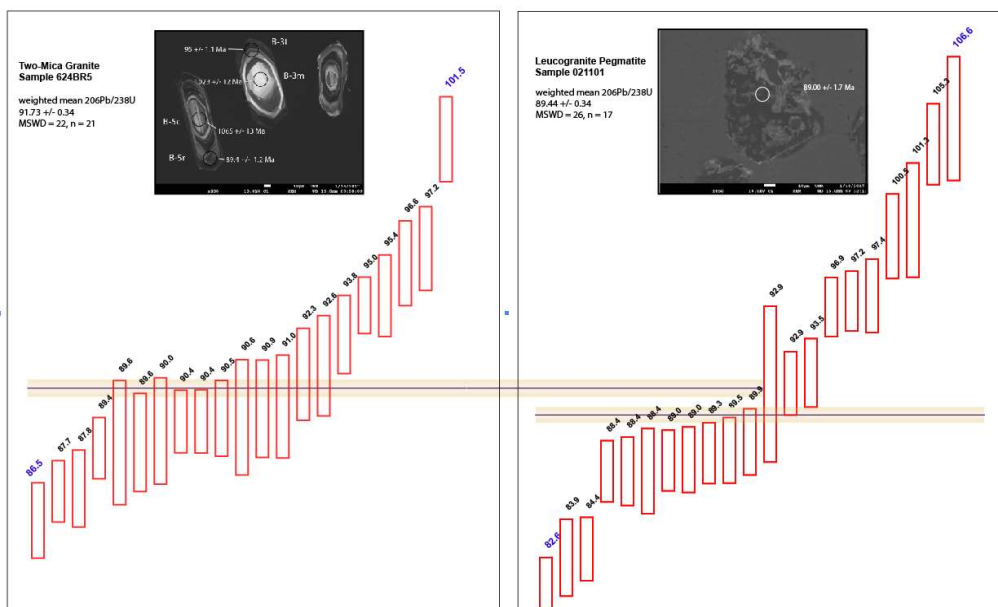
Figure 17. Plot of individual zircon grain ages. Two-mica granite zircon rims and igneous grains (left) and leucogranite pegmatite crystals (right).

suggests a specific pressure and temperature range during crystallization of 3-6 kbar (11-22 km) and 640-720°C (Kerrick, 1972; Schleicher and Lippolt, 1982), pointing to mid-crustal crystallization and protracted elevated temperatures during crustal melting and pluton formation. Similar extended crystallization periods of approximately 10 m.y. have been reported in Cretaceous Sierra Nevada granitic intrusions (Tikoff and De Saint Blanquat, 1997).

Hornblende diabase sample 71315 was collected in the Drinkwater Pit at Mineral Ridge and brought back to UNR for separation of hornblende phenocrysts, with attention paid to collecting crystals without obvious chlorite or attached groundmass aggregates. A 200-µm sample of separated amphibole was sent to the Nevada Isotope Geochronology Lab at the University of Nevada Las Vegas for $^{40}Ar/^{39}Ar$ stepwise-heating analysis.
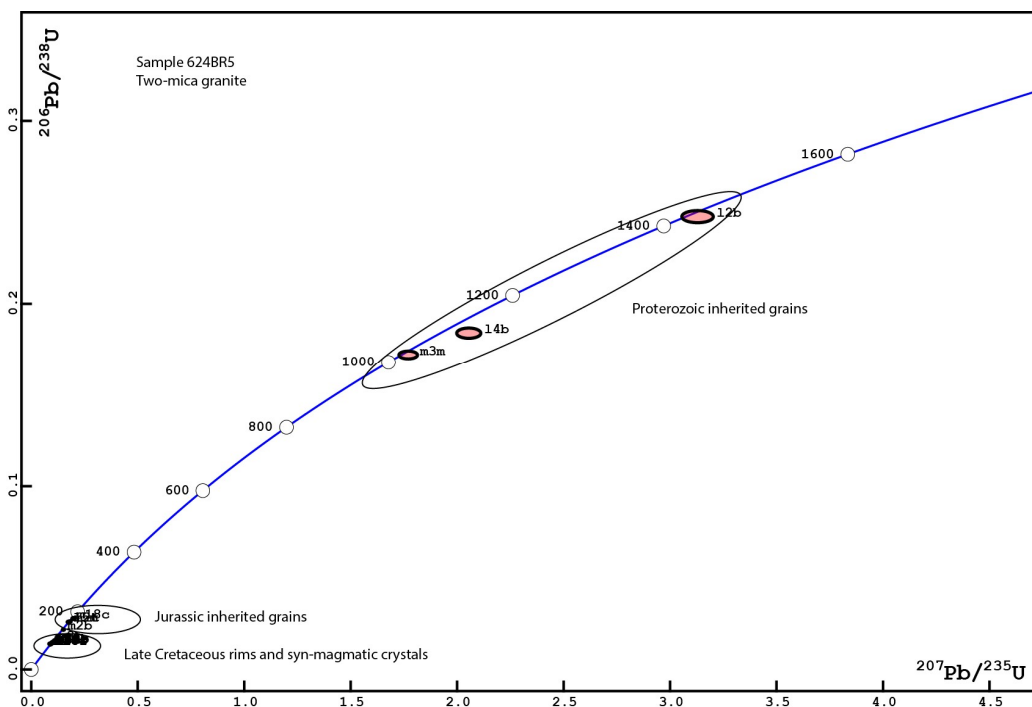
Figure 18. Concordia plot of inherited zircons from two-mica granite.

Ar-Ar analysis of the lamprophyre sill returned a disturbed "crankshaft" step-heating pattern (Figure 19) with a total gas age of 22.1 ± 0.2 Ma; except for the first two steps, which have higher calculated ages of ~31 and 63 Ma, the remaining 11 steps give consistent, although not overlapping ages of between ~16.8 and 21.2 Ma, with a weighted average of ~18 Ma. The foliated sill in question cross cuts the Late Cretaceous leucogranite, thus it postdates granites but predates metamorphism and deformation. An imprecise total gas age of ~22.1 Ma therefore is interpreted as post-intrusion cooling below ~550° C, the closure temperature of hornblende. Excess argon contamination is common in metamorphic rocks, hydrothermal systems, and shear zones (Kelley, 2002), any of which could be an issue in interpreting cooling histories from pre-exhumation rocks derived from the lower plate of the Mineral Ridge metamorphic core complex. Therefore, a valid emplacement age for the pre-Tertiary mafic sills was not determined; however, the derived age data are useful in interpreting the thermal history of the Mineral Ridge metamorphic complex and its association with gold deposits.
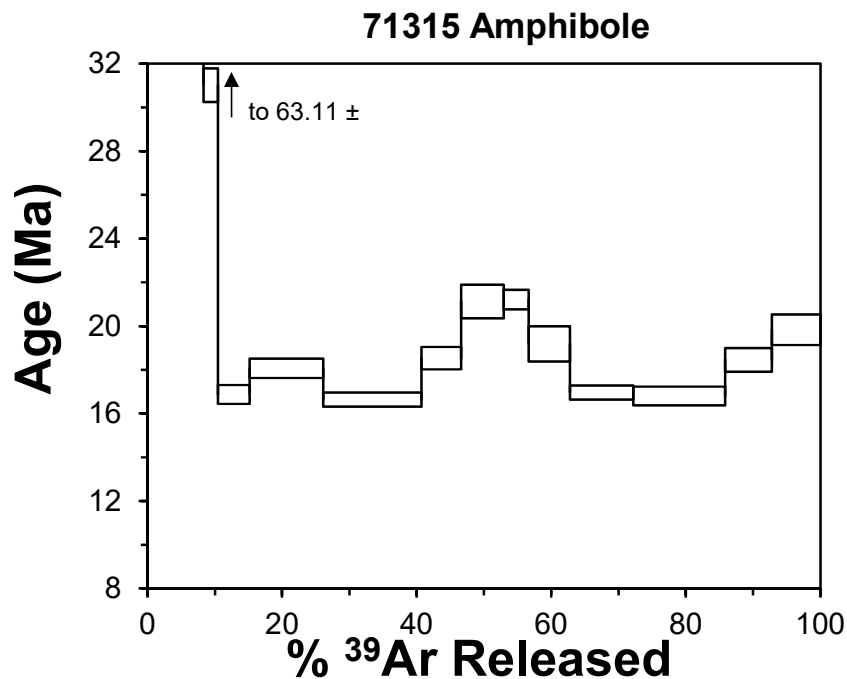
Figure 19. Ar-Ar hornblende step-heating analysis.

Mineralization

Gold mineralization at Mineral Ridge is related to milky white quartz veins and lenses that are locally ductilely deformed and hosted in Precambrian-Cambrian metasedimentary rocks and Late Cretaceous granitic rocks. In stark contrast to the silver-rich epithermal deposits that characterize the rest of the Silver Peak mining district, Mineral Ridge is a gold-rich system with gold:silver ratios between ~1 to 8, averaging 3.7. These coarsely crystalline, non-directional, milky white 'bull quartz' veins, boudins, and lenses are oriented parallel to the dominant tectonic foliation in the metasedimentary Wyman Formation which, in turn, mimics the large shear zone that defines the orientation of the major Drinkwater and Mary-LC zones (Figure 3) first mined underground, and later developed for open-pit mining. On the northeastern limb of the Mineral Ridge anticline, where Drinkwater and Mary-LC are located, the shear zone and ore zones strike northwest and dip to the northeast at 30-45 degrees. Productive quartz bodies were emplaced along areas of strong rheological contrast such as intrusive-metasedimentary contacts, marble-siliclastic contacts, or contrasts in metamorphic grade. Quartz veins range in size from mm-scale veinlets between bedding planes to multi-meter-scale boudins that displace less competent bodies of host rock. Textures in the ore zones range from opaque, milky white quartz bodies lacking fractures to less common, severely brecciated, gossanous zones. A variety of micro-fractures, stylolites, and discontinuous schistose wall rock inclusions (ribbon quartz) (Figure 20) are commonly observed in and near ore zones. The greatest shared features are an anastomosing shear fabric together with granoblastic texture of the quartz crystals. In thin section, these quartz grains are annealed and show a strong undulose extinction and are transected by anastomosing shear bands of fine-grained micro-mylonites containing abundant white mica and carbonate. Base-metal sulfides, native gold, and gold-bearing pyrite are found in the highest-grade ore samples, although on average the ore zones are relatively sulfide-poor, often with ≤1% modal sulfide and <1 wt.% sulfur. As noted by Spurr (1906), quartz bodies that are micro-fractured or brecciated and contain pyrite and iron oxides

appear to be an indicator of higher gold grades, suggesting a late-stage introduction of gold with

pyrite and base metals.

Figure 20. Ore vein textures at Mineral Ridge.

(a) Base-metal rich quartz bodies. (b) Fractured, iron-oxide breccia. (c) Schist-hosted quartz bodies. (d) Marble-hosted quartz veins and boudins. (e) Ribbon-quartz. (f) Limey-siltstone with quartz veinlets. Scale in cm.

A later stage of non-foliated microcrystalline to coarsely crystalline quartz veins, found across

Mineral Ridge but densely clustered east of the Solberry deposit (Figure 3), obliquely cuts schist of

the Wyman Formation, two-mica and leucogranites, and non-foliated Miocene mafic dikes (Figure

21). This late stage of quartz veining is distinctly different than the ore-hosting quartz veins. Late

quartz lacks any sort of foliation, and occurs as small sub-cm stockworks or sheeted vein sets, and as

planar veins generally 1-2cm in width but up to 13 cm in width. Textures encountered include ataxial

open-space crystals and saccharoidal quartz. The color of this vein quartz is white to blue, blue-gray,

and dark-gray. Multiple pulses of late quartz veining are recorded by brecciation with quartz vein

material and wall-rock clasts. Gold values are generally below 10 ppb in late vein material, and

entirely below 100 ppb. Late veins generally strike N60°W and mean dip of 58°NE, and crosscut ore-

bearing quartz veins by approximately 45 degrees of dip. Late veins more closely approximate

orientations of late normal faults and mafic dikes, both of which cut ductile foliation at a high angle.

These relationships suggest that the late veins were emplaced during a late extensional (post-detachment) regime associated with mafic magmatism.
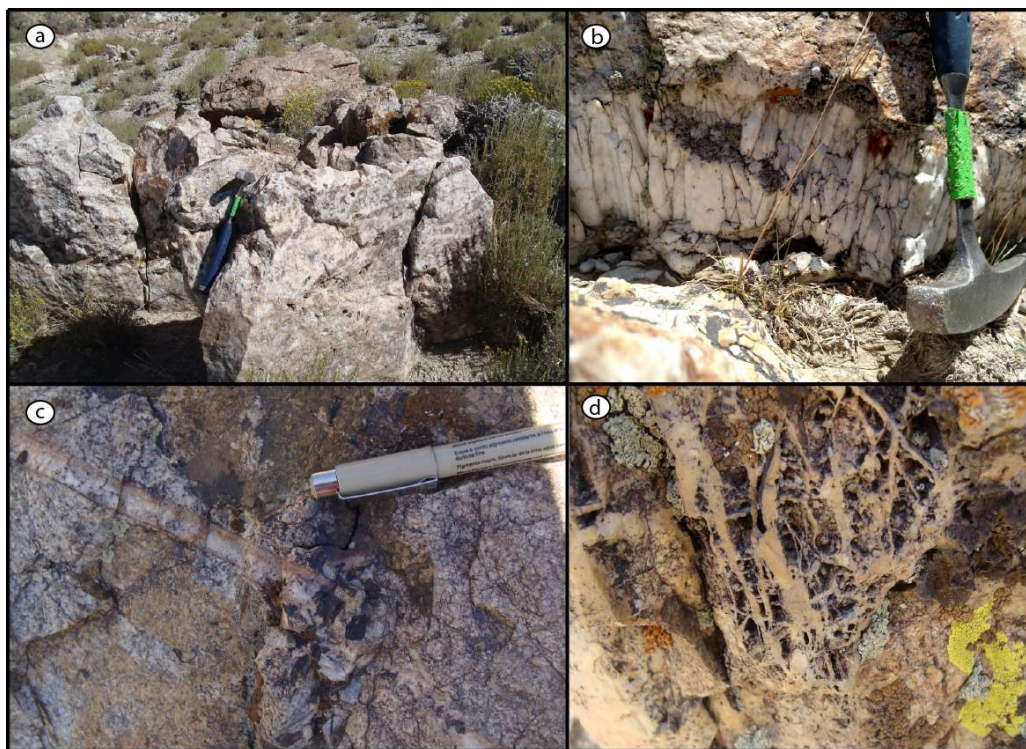
Figure 21. Textures of post-mineralization 'epithermal' quartz veins. (a, d) Stockworks, (b) ataxial veins, (c) planar veins.

Host Rocks

The major vein host for gold at Mineral Ridge is the metasedimentary Wyman Fm. In the lower levels of the Drinkwater mine, rocks of the Wyman are calcite marble dominant with subordinate schist interlayers and complex lit-par-lit leucogranite sills and quartz lenses. Ore-hosting marbles and calc-silicate schist are composed of interlocking calcite with minor muscovite, quartz mylonites, clinozoisite, oxidized pyrite, chalcopyrite, and 100-μm relict amphibole grains altered to chlorite and hematite. Calcite marbles give way to calcareous and chloritic schists and phyllites moving up-section, with phyllite and quartzite at higher stratigraphic levels of the Wyman Fm.

Metamorphism of the rocks of the Wyman Fm. were described by Kirsch (1968) as consisting of almandine-amphibolite facies with occasional sillimanite. Kirsch's findings were similar to findings in this study, which recognizes greenschist- (chlorite, biotite, muscovite schists and quartz-

clinozoisite-calcite calc-silicates) perhaps as retrograde assemblages to amphibolite facies

(muscovite-almandine-staurolite schists). Relict amphiboles altered to chlorite may represent the

retrograde amphibolite-greenschist path following granitoid generation. Late hydrothermal

alteration of host rocks to Ca-Fe carbonates, sericite, chlorite make determinations between

metamorphic and hydrothermal effects difficult. Bercaw (1986) attributes some of the metamorphic

effects in the lower plate to contact metamorphism from the Mineral Ridge pluton, although

thermal effects from a catazonal crustal melt granite would likely be minor due to relatively low

temperature and chemical contrasts.

Local Structural Control

Ore zones in the Drinkwater deposit, the most productive mine in the subdistrict, are hosted

in ductilely deformed metasedimentary layers that dip approximately 30° northeast (Figure 22, 23,

24). The northeast highwall shows some important structural relationships in the primary ore zone

delineated by the historic underground workings, which closely follow the contact between

Cretaceous granitoids in the footwall and marbles and schists of the Wyman Fm. in the hanging wall

(Figure 22, 23). The intervening 25-meter-thick shear zone is populated by calcite marble and calc-

silicate schist migmatite with sills of leucogranite and cm- to m-scale folded quartz veins and

boudins. High-grade gold (>10 ppm) mineralization is found along multiple structural anisotropies in

this shear zone from mm-wide quartz veins between schist foliations, decimeter-wide veins along

contacts of footwall leucogranites, to 1-m-long quartz lenses within marble-leucogranite migmatite.
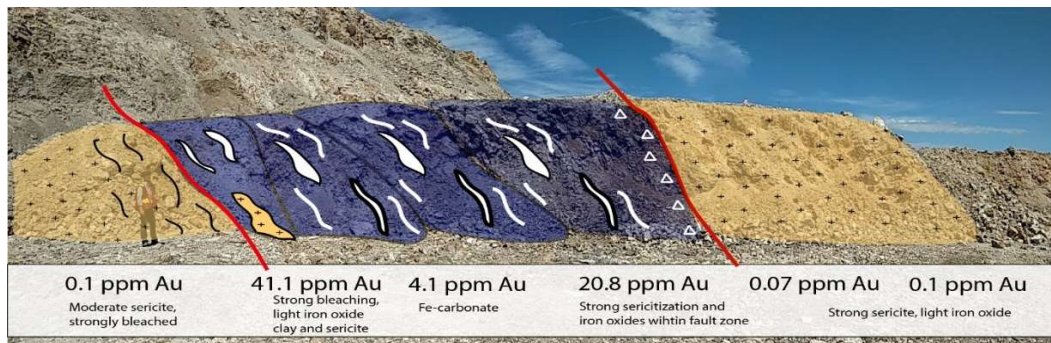
Figure 22. Schematic cross-section of ore zone from Mary mine in June 2016 looking south.

Felsic intrusive units (orange) bounding a limestone-rich Wyman Formation (purple) bench with concordant quartz veins.

Most of the mining targeted this northeast-dipping shear zone, which includes the Drinkwater and Mary deposits, extending approximately 1,400 meters of strike length (Hruska et al., 1996) southeast to the Custer Canyon area (Figure 3).

Strong competency contrasts between lithologies are a consistent control on ore zones at Drinkwater and elsewhere at Mineral Ridge. In particular, contacts between intrusions and marbles are favored, where zones of dilation were more easily accommodated by differential strain. In general, ore zones occur in ductile or brittle-ductile high-strain zones characterized by imbrication and rotation of feldspars, boudinage, and foliation-parallel gold-quartz lenses connected by severely attenuated veins, commonly with refolded folds that are oriented sub-parallel to foliation. Foliation-parallel shear veins in orogenic gold deposits have been linked to large-scale reverse faulting (Roering and Smit, 1987; Cox et al., 1991), but no strong evidence of thrusting such as stacking or repetition of units is visible at Mineral Ridge. Because of an interpreted deep exposure level and ductile fabrics, shear-related gold deposits at Mineral Ridge likely represent deeper and hotter variations of orogenic gold deposits (>400°C and 2.5 kbars) such as deposits of the Yilgarn Craton of Western Australia, which are typified by foliation and bedding-parallel veins and ductile shear zones (Goldfarb et al., 2005).

Orientations of planar features such as gold-bearing quartz bodies, schistose foliation in rocks of the Wyman Fm., and the dip of the shear zone are sub-parallel to one another (Figure 24) along the entire northeast limb of the Mineral Ridge anticline, dipping northeast approximately 30 degrees. However, due west of Drinkwater and towards the hinge of the Mineral Ridge anticline, orientations of the ore zones and tectonic foliations in the Oromonte mine level out to nearly flat, or dip towards the E/NE only ~10 degrees (Bercaw, 1986; Hruska et al., 1996). Orientations of quartz veins and granitic sills dip to opposite direction on the west limb at Brodie pit, dipping moderately to the southwest. On a broad scale, ore zone orientations follow the general tectonic foliations of the host rocks, which align with the NW fold axis of the Mineral Ridge anticline. Because the ore bodies
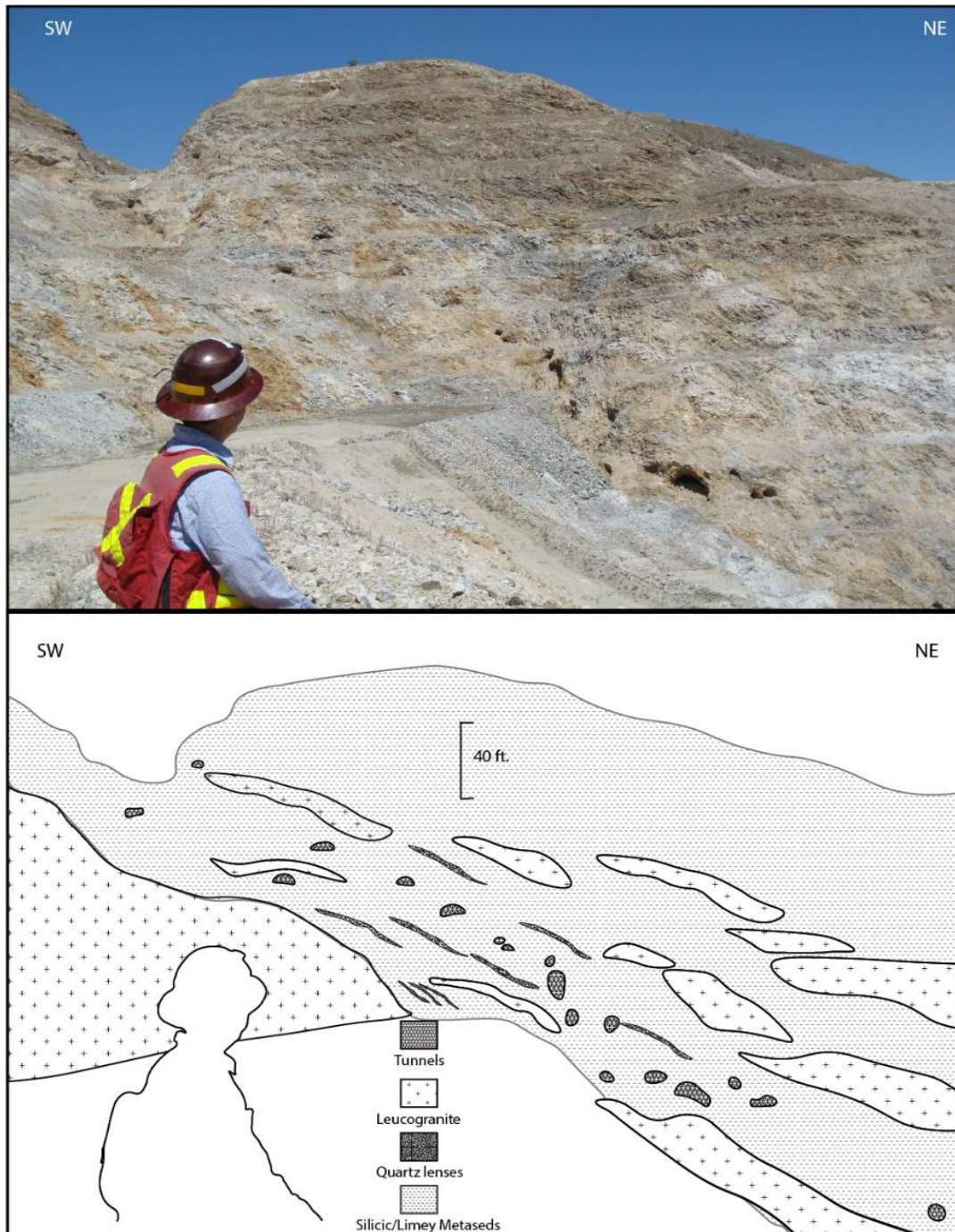
Figure 23. Northwest view of Drinkwater shear zone.

themselves are folded and do not form parallel to the fold-axis (Cheong, 2000) or form saddle reef

geometries (Cox et al., 1991), it is assumed that gold mineralization occurred prior to the broad

folding event. Alternatively, strongly deformed ductile shear zones with shallow geometries were

the first-order control across the field area, and were later folded into a NW-trending anticline, and

dismembered by late normal faults.
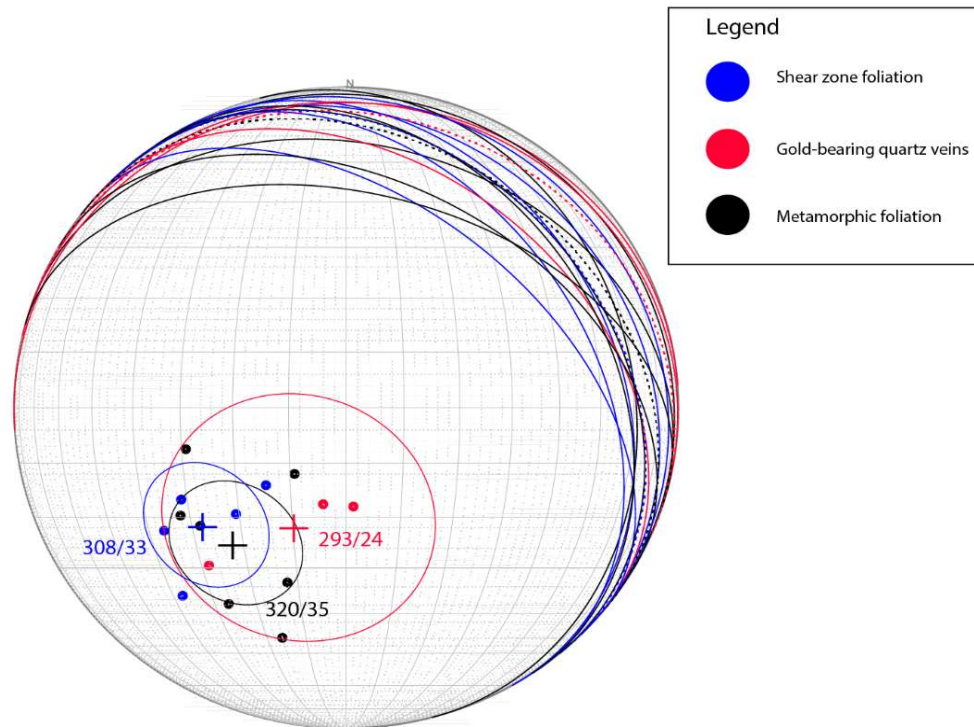
Figure 24. Structural measurements from ore zone of Drinkwater mine. Crosshairs and associated values represent mean strikes/dips for various structural features.

Vein Description and Mineralogy

After two field seasons at Mineral Ridge utilizing the on-site fire assay lab as well as ALS

Minerals for trace-element geochemistry and Au/Ag assays, it is apparent that the gold

mineralization is restricted to quartz veins and bodies and that very little gold occurs in non-veined

wall rock. Gold-bearing quartz bodies coincide with a weakly developed carbonate-muscovite

alteration halo in adjacent rocks, which can go almost undetected in the greenschist-facies

metamorphic host rocks.

Prospective mineralized zones range from mm-scale bedding-plane quartz replacements in phyllitic to schistose Wyman Fm. rocks to m-scale quartz boudins varying from milky white and sulfide-poor, to mild limonite staining and crackle breccia, to completely decomposed, gossanous breccia zones filled with clasts of quartz lenses with limonite and later cemented by open space quartz. Within a specific breccia zone at the south end of the Brodie mine, the highest grades seem to follow zones of maximum brecciation and highest concentrations of hematite and goethite after base-metal sulfides, (e.g., 32.8 ppm Au), whereas the more common sulfide-poor, pure white veins are lower grade (6.25 ppm Au). The relation between quartz vein density and gold grade is difficult to quantify, possibly due to the 'nugget effect' of free gold in quartz. Leucogranites with ~40% milky quartz veins commonly contain less than 70 ppb Au, whereas calc-silicate schists with inter-layered, boudinaged, and sheared quartz with <20% vein density may carry >5 ppm Au.

Ribbon quartz textures are a common indicator of gold mineralization. The vein-parallel thin, dark bands of schistose wall-rock are discontinuous, mm-scale likely derived from enclosing Wyman metasedimentary rocks. In thin section (Figure 25)**,** ribbons mostly contain muscovite, calcite, and
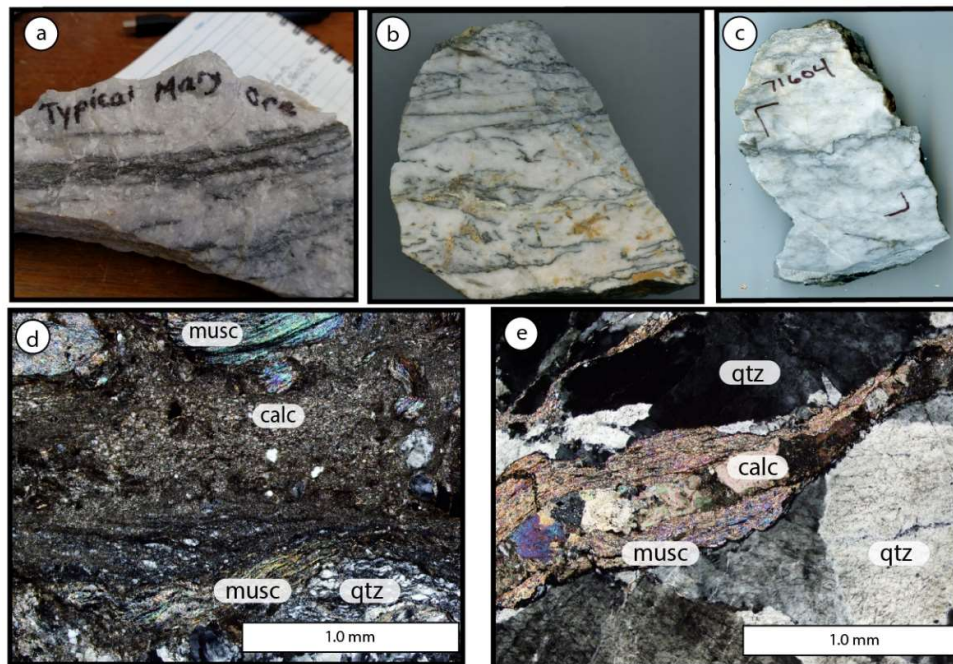
Figure 25. Hand samples of ribbon-quartz textures in quartz veins (a,b,c). From linear bands (a) to stylolites (c). Thin section photomicrographs of ribbon material (d,e).

chlorite, with abundant siderite or other carbonate, actinolite, pyrite, and lesser chalcopyrite, hosted

in quartz deformation bands grading out to coarser quartz grains. Gold is peripheral to the ribbons

as free grains within quartz or as inclusions in pyrite along foliation. Laminated textures parallel to

wall rock are suggested to represent episodic fluid flow during tectonic events and movement along

the shear zone (Taylor et al., 2015), occurring near the brittle-ductile transition (Vearncombe, 1993).

It is not completely clear whether the ribbons are truly slivers of wall-rock removed during episodic

crack-seal events or rather pressure-induced deposition of ore minerals. In either case, the minerals

composing the ribbons are consistent with greenschist-facies metamorphism, and likely reflects the

pressure-temperature-chemical conditions during vein formation.

Thin-section petrography and scanning electron microscope study of gold-quartz bodies

(Figure 26) indicates that free gold exists in quartz with muscovite and carbonate, typically as grains

that are 7 to 75 microns in diameter. Blebs of gold and/or electrum occur in euhedral to subhedral

grains of pyrite (Figure 27), which are often mantled or embayed by sphalerite, galena and/or

supergene anglesite, indicating that the precipitation of base metals occurred after some gold

deposition. Silver concentrations of the gold grains average between 15-20% using SEM-EDS

analysis, which approximately matches with gold:silver ratios of 1 to 8 found in assay results. Visible

Figure 26. Typical example of ductile marble-hosted gold-bearing milky quartz vein mineralization. Dark bands contain chlorite, muscovite, carbonate, and pyrite.

gold is rare, but is observed most commonly in high-grade samples (>30 g/t Au) associated with

base-metal sulfides as inclusions within galena (Bercaw, 1986).
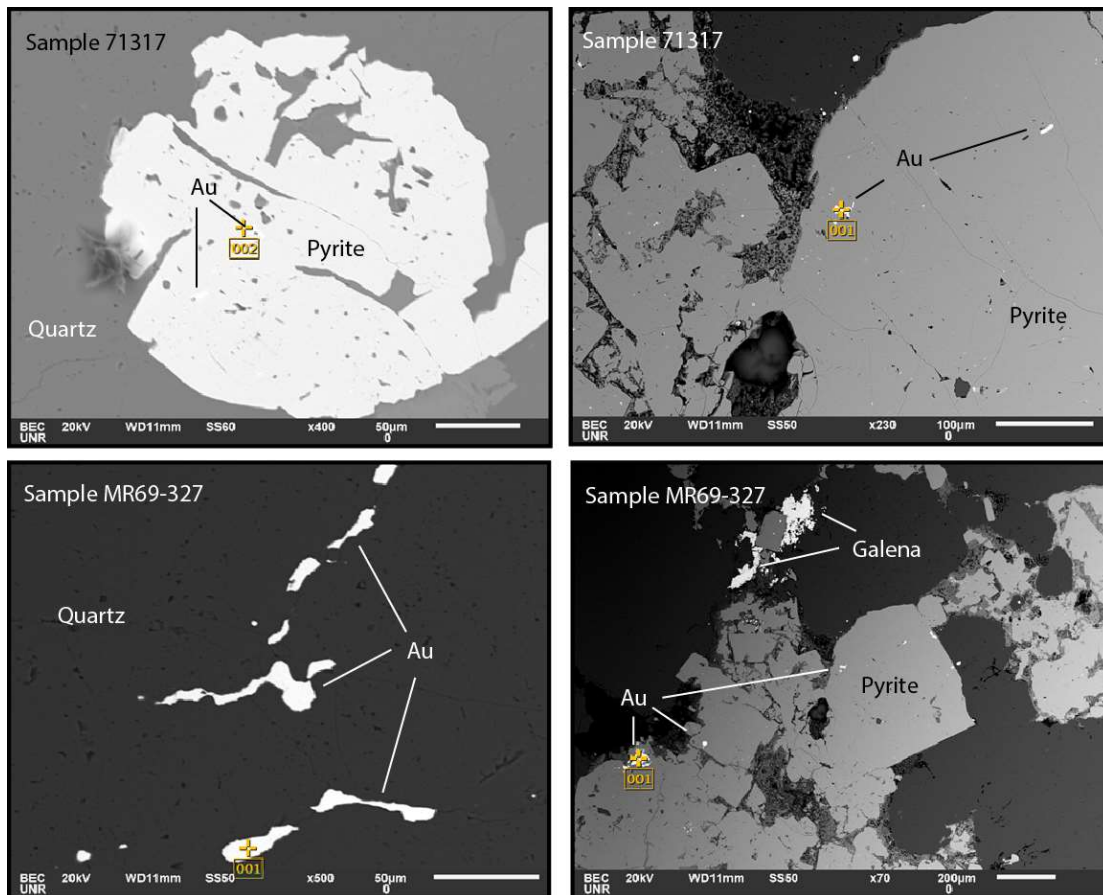
Figure 27. SEM images of gold occurences.

Quartz associated with gold is severely deformed in thin section with strongly undulatory

grains and shear bands of micro-quartz mylonites. Quartz grains range from sub-micron mylonites to

coarse granoblastic grains up to 5.0 mm in size. Fine-grained quartz mylonite is common and always

associated with mineralization, however free gold tends to be within larger, undulatory, non-

mylonitized grains. Gold-bearing quartz veins are dense with fluid inclusions, generally 5-20 μm in

diameter, lacking daughter crystals, and containing approximately 30% vapor on average, with some

having a thin outer rind of CO_2 vapor encircling the vapor bubble.

Muscovite and sericite are common accessory minerals in veins, but are not always present in mineralized samples. Samples with high base-metal contents from the Brodie pit, which may represent late- or remobilized mineralization, contain free gold up to 35 um in diameter, but no muscovite. Calcite and siderite, generally sub-mm in size, occur as replacements of plagioclase, selvages mantling quartz veins and augens, aggregates with muscovite and pyrite, and as late veinlets. Larger calcite grains may exhibit undulatory extinction. Hydrothermal monazite occurs alongside quartz-muscovite-pyrite-carbonates in small single grains (5-25 μm) and larger mossy aggregates up to 60 μm in diameter. Monazite is often entrained in high-relief, highly birefringent calcite, which makes identification without SEM-EDS difficult.

Base-metal sulfides seem to be more common in the western deposits, near where the 'epithermal' overprint occurs, and rare in the eastern deposits. It is not clear if base-metal mineralization is due to location on west limb of Mineral Ridge anticline closer to Silver Peak Neogene volcanism and/or the higher structural levels of the western limb deposits reflecting metal zonation in the main-stage gold event. Gold to silver ratios in the base-metal rich ores are consistent with typical Mineral Ridge samples (Au:Ag >1), and base metals correlate positively with Au in the western deposits, suggesting the base-metal sulfides are not an epithermal overprint. Galena and sphalerite mantle gold-bearing pyrite and follow brittle planar fractures cutting sheared vein quartz (Figure 28); the base-metal sulfides are only found in some sheared Au-bearing milky quartz veins, not in wallrocks or in the younger, crosscutting quartz veins at the Brodie mine. Pyrite is common but not abundant, generally less than 1% modal and less than 1% molar S. Pyrite can form anhedral blebs or euhedral/subhedral crystals with Au inclusions. Arsenopyrite is rare in samples from the

Drinkwater and Brodie, mines, but Bercaw (1986) reported arsenopyrite to be the most important

ore sulfide at the Oromonte mine (Figure 3).
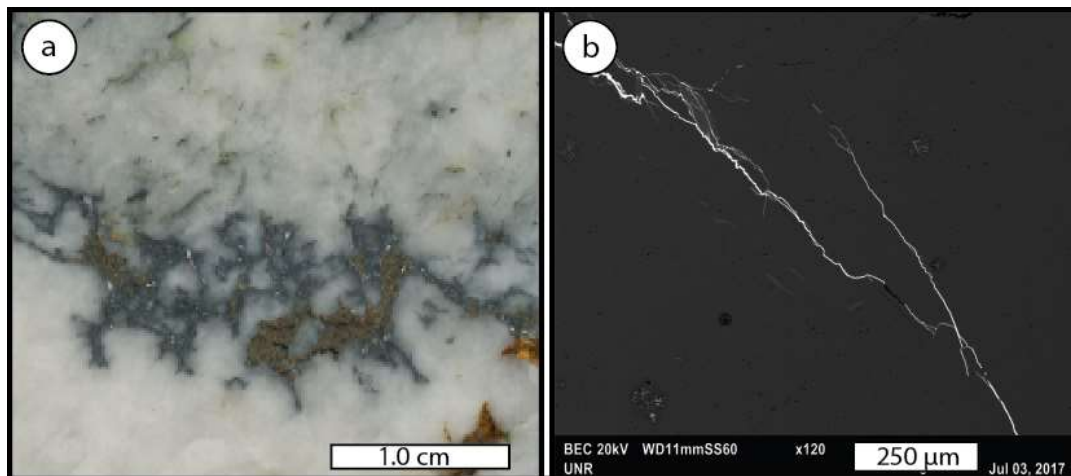
Figure 28. Late base-metal sulfides.

Brittle discordant veins of galena and sphalerite in hand sample scale (a) and late fracture infillings of galena under SEM backscattered electron imagery (b).

Trace-element Geochemistry

Fifty-three samples of quartz vein material or host rock containing ore veins were collected

from the Brodie, Drinkwater, Mary, Bluelite, and Solberry mines at Mineral Ridge and analyzed using

a commercial four-acid digestion and ICP trace-element multi-element and fire-assay gold analysis.

Of the fifty-three, thirty samples contained gold contents greater than 100 ppb, and were studied

further. Trace-element geochemistry of ore-grade samples (~>1 ppm Au) is listed in Appendix A-1.

The limited number of mineralized samples analyzed for trace-element geochemistry limits

characterizations of metal associations and correlations, and this is further hampered by a late

overprint or zonation of base metals in the western deposits. The overprint is not recognized at the

main Drinkwater and Mary mines on the eastern limb of the Mineral Ridge anticline. Pb and Zn

values in the 100-10,000 ppm range are associated with high-grade gold mineralization in the Brodie

and Bluelite pits with visible galena and sphalerite situated along brittle fractures in milky quartz

lenses, whereas individual Pb and Zn values in the Drinkwater/Mary mines rarely reach above 200 ppm. Using a rank Spearman correlation for all mineralized samples (n=30), Au strongly correlates with Ag (0.8) and moderately with Bi (0.6) (Figure 29), but further metal associations by individual deposit lack a large enough dataset for robust correlations.

Gold has no discernible correlation with sulfur, and total sulfur content of auriferous quartz bodies is generally less than one percent despite the abundance of Au-bearing pyrite. The lack of a correlation between sulfur and gold is likely due to multiple stages of pyrite introduction, most of which is barren of gold. During sampling, modal pyrite did not appear to be a direct pathfinder. However, the presence of base-metal sulfides usually signifies high gold grades. Silver directly correlates with gold, because the silver occurs in electrum or at least as a component of native gold. No silver-bearing minerals other than electrum and argentiferous galena were observed. In ore-grade samples over 1 ppm Au, gold to silver ratios range from 1 to 8, with an average of 3.7. There is a very low abundance of Sb, Te, and W in quartz veins, between 0-5 ppm, and no strong correlation between these elements and Au exists. Cu displays minor correlations with Au, but shows no values much over average crustal abundance (42 ppm; Rose et al, 1979). Arsenopyrite is not a common ore mineral at Drinkwater or Brodie mines, and likewise As does not correlate with Au in these deposits. Arsenic averages 29 ppm across Mineral Ridge, spiking to 310 ppm in a 0.5 ppm Au sample from the Bluelite deposit, a northwest satellite. Bi and Mo correlate strongly with Au (Figure 29), despite lack of identified Au-Bi minerals or molybdenite; Mo values are less than 10 ppm, whereas Bi values range from <1 to nearly 50 ppm (Appendix A-1). Zn and Pb show a moderate positive correlation with Au in the western deposits but Pb and Zn are lacking in the Drinkwater or Mary mines.

Hydrothermal Alteration

Alteration associated with ore zones is limited in intensity and range, likely due to near thermal and chemical equilibrium and time of deposition. Within meters of productive ore zones, granites are fresh and have unaltered plagioclase. Adjacent to ore zones, plagioclase and microcline alter to mixtures of fine-grained white micas and calcite, and biotite alters to coarse chlorite and

sericite. Chlorite, muscovite, and carbonate replacements of garnet emanate at crystal boundaries, which may be attributable to coeval retrograde metamorphism and hydrothermal alteration.
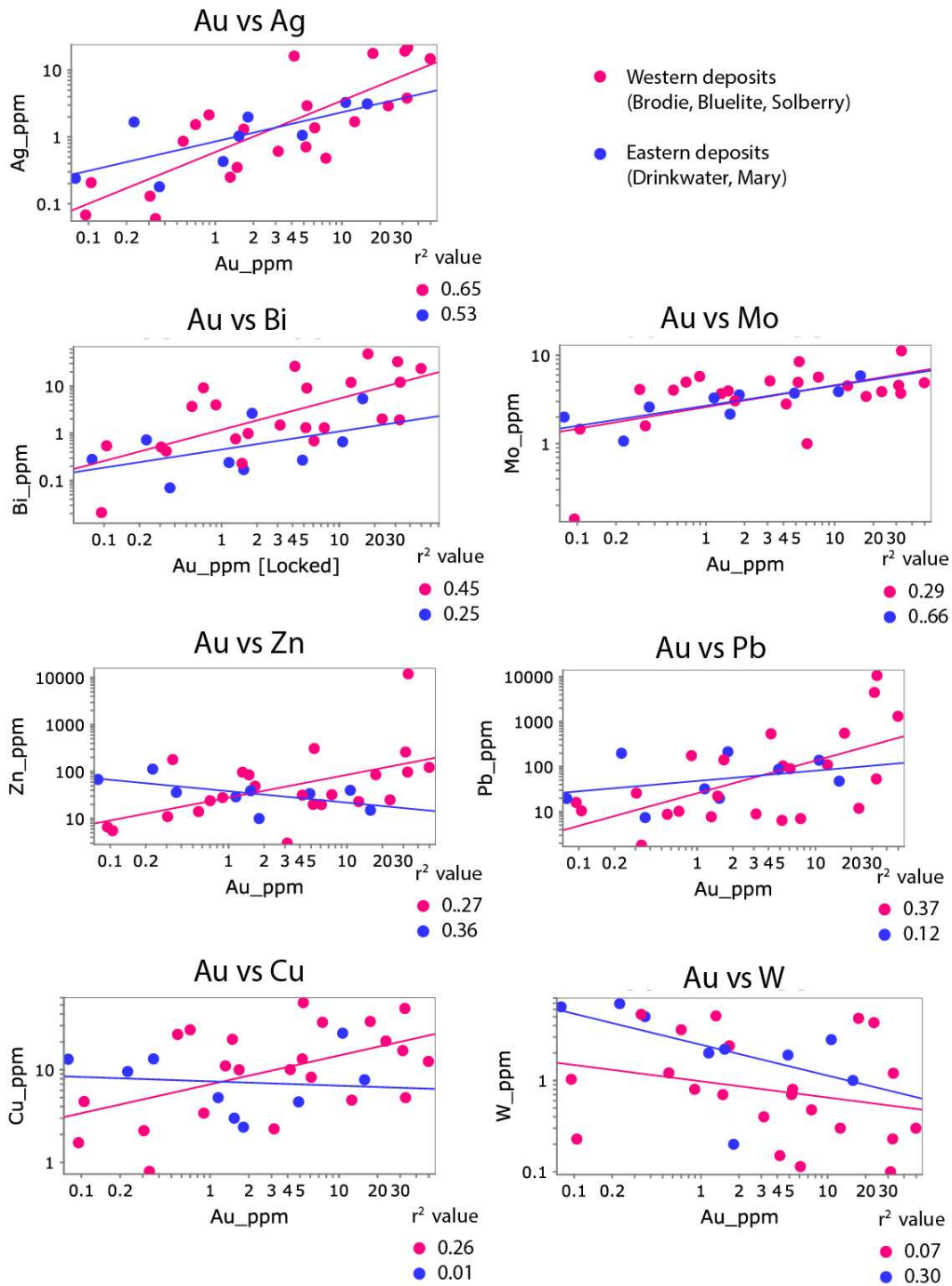
Figure 29. Log-log scatter plots of elemental correlations with gold.

Strong argillic and sericitic alteration occurs in the footwall of high-angle normal faults in the Brodie pit, completely altering feldspars and coarse micas to illite and montmorillonite. Heavily oxidized iron sulfides are associated with this late stage alteration particularly in the Miocene diabase dikes. Broad bleached zones of light-colored clays, pyrite, carbonate, goethite, and hematite occur adjacent to breccia that also are related to hydrothermal activity. Intense clay alteration is present in high-angle structures and affects intrusions in the Brodie pit but is not common elsewhere. However, clay alteration cuts quartz-sericite-carbonate alteration, and therefore postdates main stage gold mineralization. Illite alteration may be associated with the minor epithermal-like gossanous breccias of the Brodie mine. Neogene low-sulfidation epithermal mineralization is widespread in the neighboring Red Mountain subdistrict, 10 km west, although the abundance of base metals is not known but considered to be low (Cline, 1986).

Carbonation alteration is pronounced in all ore zones, most often occurring as fine- to coarse-grained calcite and siderite replacements of plagioclase, in veins containing muscovite and pyrite, and as fine-grained selvages along quartz body boundaries. Strong reaction to HCl is ubiquitous in ore zones. Sericitization of feldspars, mostly as muscovite, is common in proximity to ore zones, although intensity is limited. Localized overprinting clay alteration (likely smectite-illite) at the Brodie pit and surrounding areas may relate to Miocene hydrothermal activity particularly to deposits on the west limb of Mineral Ridge, and deep sericitization with pyrite occurs in the Drinkwater pit along high-angle faults, with no associated Au-Ag mineralization or quartz veining. Chloritization of biotite and hornblende in mafic dikes and sills is common. Variable pyritization occurs near mineralized zones and extends into the Wyman Formation.

Mineralization Age

A maximum age of mineralization for gold mineralization at Drinkwater based on field relationships is constrained between 89.7 ± 0.5 Ma leucogranite and crosscutting gold-bearing quartz veins. In addition, non-foliated post-mineral dikes with $^{40}Ar/^{39}Ar$ whole-rock cooling ages ranging from 14 to 10 Ma (Petronis et al., 2002) require gold mineralization to be older than mid-

Miocene. However, this leaves an approximately 76 m.y. 'mineralization window'. From field

relationships of the ductile nature of the auriferous quartz veins at Mineral Ridge, we hypothesize

that the mineralization is further limited based on lower-plate cooling ages of various minerals and

an assumption that gold mineralization occurred both at and possibly above, brittle-ductile

conditions (~400°C) (Fournier, 1991). Using the 300°C closure temperature of biotite in the Ar-Ar

system (Harrison et al., 1985), a temperature-time of 300°C at 55 ± 2 Ma can be approximated using

published geochronology of the Mineral Ridge pluton (Diamond and Ingersoll, 2002). This narrows

the possible mineralization age between approximately 89.7 and 55 Ma. However, to understand

the temporal relationship between the granitic intrusions and gold mineralization at Mineral Ridge,

much better resolution is required.

Gold mineralization at Mineral Ridge is closely associated with narrow zones of quartz-

sericite-pyrite alteration adjacent to quartz veins and with irregular vein-like segregations of sericite-

carbonate in Au-bearing vein quartz. However, the complex Cenozoic thermal history of the

mineralized lower-plate of the Mineral Ridge metamorphic core complex yields additional data for

the Ar-Ar system because of the wide range of closure temperatures in K-bearing minerals

(hornblende = 550° C; muscovite = ~300° C; plagioclase = ~250° C). This lack of Ar retentivity under

metamorphic conditions, which may preclude assessment of crystallization ages, yields important

post-crystallization time-temperature information (i.e., thermal histories) that is useful. At Mineral

Ridge, abundant coarse muscovite and fine-grained sericite occur as both igneous and hydrothermal

minerals. For this study, no attempt was made to date hydrothermal phyllosilicates that ideally could

constrain the timing of gold mineralization. Because gold mineralization appears to have occurred

post-peak metamorphism under greenschist conditions, the possibility remains that white mica may

produce meaningful results in dating mineralization.

An alternative to dating white mica to constrain the timing of gold mineralization at Mineral

Ridge is the dating of the REE phosphate, monazite, which somewhat surprisingly occurs as small (5-

25 μm) disseminated grains and in clusters of apparent hydrothermal origin in Au-bearing quartz veins. Monazite (Ce, La, Nd, Th) PO_4) is one of the main repositories for Th and rare earth elements (REE) (Poitrasson et al., 1996), and more importantly, accepts U and Th but not Pb, allowing its use as a stable U-Pb geochronometer (Sindern et al., 2012). Monazite is widespread in igneous, metamorphic, and hydrothermal systems (Kempe et al., 2008), readily retains radiogenic lead, has a closure temperature (~720-950°C), much higher than temperatures of hydrothermal fluids that form orogenic gold deposits (Cherniak et al., 2004), is resilient against radiation damage (metamictization), and can be analyzed through in-situ methods such as secondary-ion mass spectrometer (SIMS), laser ablation inductively coupled mass spectrometry (LA-ICP-MS), and sensitive high-resolution ion microprobe (SHRIMP) directly from petrographic thin sections (Harrison et al., 2002).

Although not as common as other direct-dating methods for hydrothermal events, U-Pb monazite has been shown to be a suitable method for certain ore deposits where other datable materials may not be available or are unsuitable due to low closure temperatures, such as orogenic gold systems (Brown, et al., 2002; Rasmussen et al., 2006; Sarma et al., 2008). Only recently has REE-phosphate (e.g. xenotime or YPO_4) been used to date young orogenic deposits, such as the Mother Lode in Grass Valley, California (Taylor et al., 2015). In contrast to igneous and metamorphic monazites, hydrothermal monazite contains very low concentrations of thorium (Kempe et al., 2008; Taylor et al., 2015) and uranium (Brown et al., 2002) which can complicate dating attempts and yield less precise ages. In addition, hydrothermal monazite crystals are scarce and generally very small making separation and laser analyses challenging. Due to the chemical and isotopic robustness of monazite, careful selection of samples for analysis is crucial to avoid detrital or restite grains, which is why in-situ methods are popular for hydrothermal studies.

Using the JEOL-JSM 6010LA scanning electron microscope in back-scattered electron (BSE) mode and employing energy dispersive X-ray spectroscopy (EDS), monazite grains were identified

within gold-bearing quartz veins. The monazite crystals often occur in clusters of 5-20 irregularly shaped grains within a small area (**Error! Reference source not found.** 30), characteristic of hydrothermal monazite (Schandl and Gorton, 2004), and are situated within the ore assemblage of foliated muscovite-calcite-pyrite-gold. Grains are generally 8-25 microns in diameter and inclusion free, with the largest grains approximately 50 microns in diameter. Using BSE imaging, no zonation was noted in the monazite crystals which suggests the grains are not inherited and have undergone a relatively simple pressure-temperature-time history after crystallization (Sindern et al., 2012).

After identification and selection of hydrothermal monazite grains in gold-bearing quartz veins using the SEM-EDS, grains were mapped and photographed using a petrographic microscope in transmitted and reflected light to aid in locating individual monazite grains at the laser ablation laboratory. Polished thin sections containing Au-bearing quartz veins with monazite were analyzed at the Peter Hooper GeoAnalytical Laboratory at Washington State University in Pullman, Washington using a Finnigan Element2 quadrupole ICP-MS and New Wave UP-213 laser ablation system.

Results of the analysis show that the bulk of monazite grains analyzed lacked sufficient thorium, uranium, and radiogenic lead for age determinations. Out of 41 grains analyzed, only five contained sufficient U and Pb for an age determination, of which four contained excessive common lead relative to radiogenic lead and were therefore inconclusive. One monazite grain did not have significant common lead or low uranium, and returned a concordant Pb_{206}/U_{238} age of 76.0 ± 1.8 Ma (Figure 31). Two of the rejected grains show non-concordant Pb_{206}/U_{238} ages of 72.9 ± 3.2 and 76.6 ± 4.3 Ma. The small grain size, characteristic of hydrothermal monazite, further complicated in-situ analysis as the grains are difficult to find amongst high-relief carbonates and the small size approached the 12-micron laser spot size, making multiple ablations of single grains impossible. Using a system with higher resolution such as SIMS or preparing a grain mount from a large sample

of vein material would likely increase success of analysis, although at a loss of picking in-situ

monazites with visible relationships with gold mineralization.
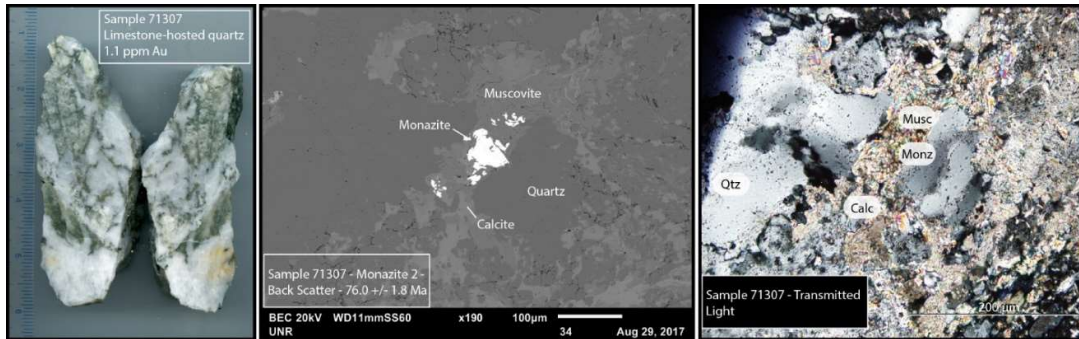
Figure 30. In-situ LA-ICP-MS U-Pb monazite sample.

From left to right; hand sample of quartz vein ore examined for hydrothermal monazite; backscatter image of monazite within muscovite and calcite; transmitted light image at similar scale, showing location of analyzed monazite with gold-bearing assemblage of muscovite-carbonate-pyrite-strained quartz.

Although the U-Pb monazite analysis was less robust than hoped for, when considering the

morphological and chemical characteristics of the individual grains, the spatial and textural

relationship of monazites within the ore assemblage, the high isotopic resilience of monazite, and

the geologically reasonable age returned for the one grain without major issues, the approximately

76 Ma date returned from analysis is interpreted as the age of gold mineralization. If the monazite

was indeed plucked from wallrock, a mechanism for depositing or resetting the monazite within the

ore assemblage would be needed to explain its young age.
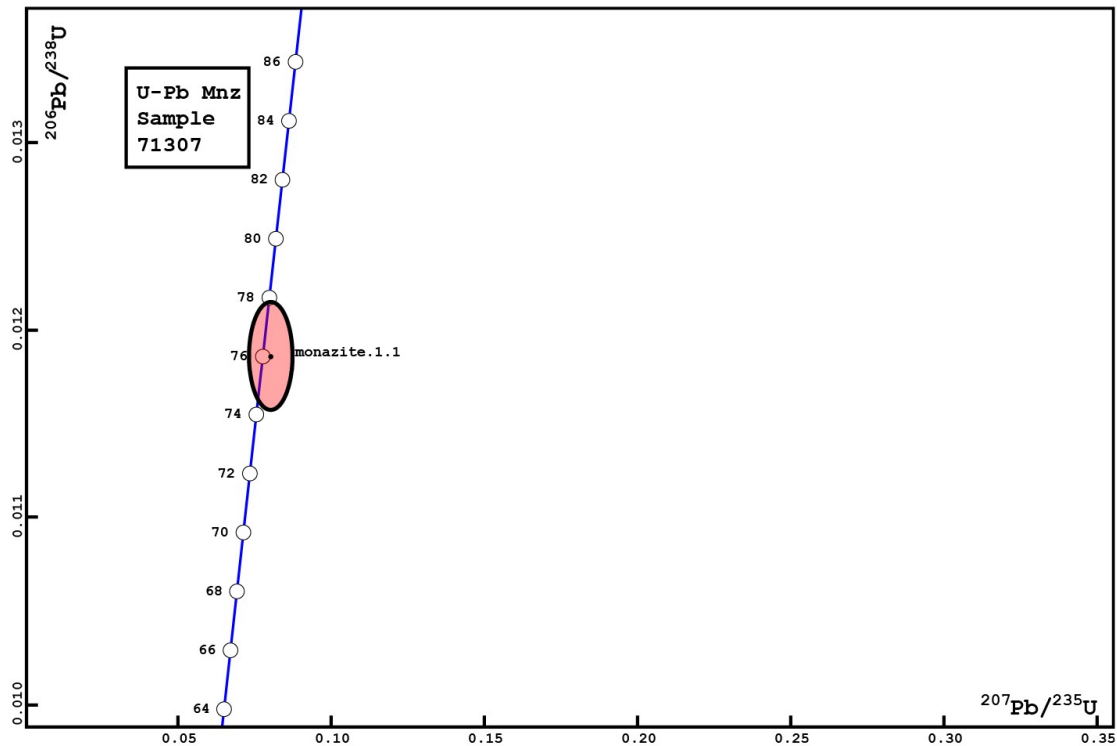
Figure 31. Concordia diagram of successful in-situ U-Pb monazite analysis.

Using the 76.0 ± 1.8 Ma monazite age as the gold mineralization event has several

implications for the geologic and mineralization history at Mineral Ridge. The Late Cretaceous age

falls within the post-granite to pre-mafic dike age, and within the >300°C mineralization window

defined by biotite Ar-Ar analysis. More importantly, a 76 Ma mineralization age creates a ≥13 m.y.

gap between granitic intrusion and gold mineralization. Even the youngest igneous zircons dated

(~86.5 Ma for two-mica granite, and 82.6 Ma for leucogranite) are substantially older than the age of

hydrothermal monazite to attribute mineralization to known magmatic activity, and arc magmatism

largely ceased by ~80 Ma throughout the Sierra Nevada and western Nevada. Geochronological data

from Precambrian orogenic deposits often describe a gap of approximately 20-70 m.y. between the

youngest local magmatism and mineralization (Groves et al., 2000), in contrast to a <2-3 m.y. gap

between arc magmatism and intrusion-related hydrothermal systems (Hart, 2007). If local

magmatism had ceased 13 m.y. prior to mineralization, Au-related hydrothermal activity must be related to a separate, non-magmatic process.
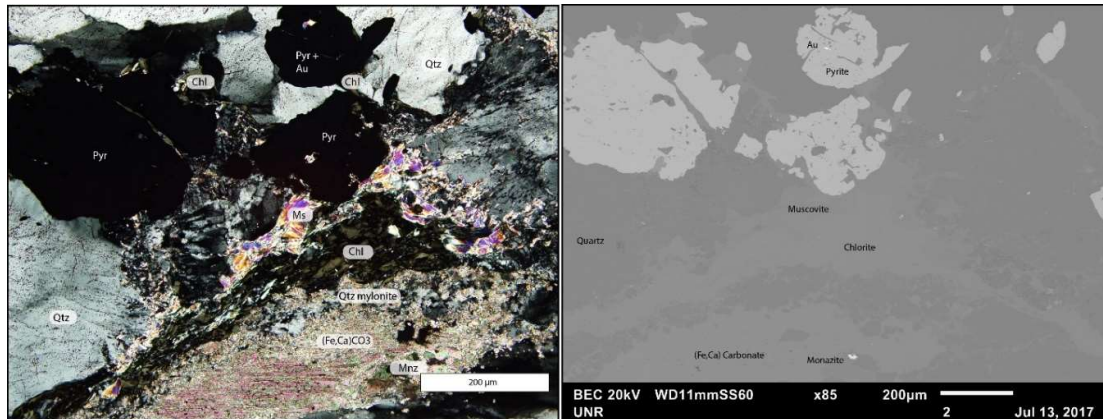
Figure 32. Petrography of hydrothermal monazite.

Crossed-polar view of a thin section of Au-bearing quartz vein (left) and corresponding BSE image (right) of hydrothermal monazite with chlorite, muscovite, carbonates, and gold-bearing pyrite in quartz mylonite ore.

Discussion

Late Cretaceous Peak Metamorphism Leading to Crustal Melting

Both felsic intrusive phases at Mineral Ridge are peraluminous (**Error! Reference source not found.**Figure 10), garnet- and muscovite-bearing, S-type granites. S-type granites are suggested to derive, in part or whole, from crustal melting of aluminous metasediments; strongly peraluminous magmas likely remain near the source of melting (White and Chappell, 1988; Villaros et al., 2009) due to high viscosities and relatively low melt temperatures. Muscovite-bearing granites and garnet-bearing leucogranites of Cretaceous to early Tertiary age, like those of Mineral Ridge, are typical of the Cordilleran metamorphic core complexes (MCCs) that form a wide belt along the deformed and metamorphosed Precambrian craton edge of North America (Howard et al, 2011) . MCCs are hypothesized to form through gravitational collapse of tectonically overthickened crust following

contraction, lower-crustal anatexis, and peak regional metamorphic conditions (Miller and Bradfish, 1980; Armstrong, 1982; Miller and Gans, 1989; Wells et al., 2012).

Cathodoluminescence (CL) imaging of zircons in Mineral Ridge two-mica granite and coarse-grained leucogranite shows that >50% (n=75) of zircons have xenocrystic cores, meaning that most of the zircons have grown from an inherited grain (either 162.2 +/- 1.1 Ma, or ~1.0-1.4 Ga). Jurassic ages from inherited cores overlap with known arc or back-arc magmatism in western Nevada (Doebrich et al., 1996), and the Proterozoic ages may represent Grenville orogeny magmatic zircons shed westward onto the western passive margin of North America after Neoproterozoic rifting (Dickinson, 2006). Mesoproterozoic zircon cores are younger than the Paleoproterozoic and older crust thought to underlie this part of the North American craton. The Mineral Ridge pluton is therefore likely derived from a large component of mixed metasedimentary and igneous crustal sources, similar to Late Cretaceous leucogranites from the White Mountains (Ernst, 1996).

Emplacement of granitic melts at Mineral Ridge was controlled by the dominant shallow-dipping tectonic foliation in the Wyman Formation, with intrusive contacts generally concordant with wall rock foliation including where foliation does not affect intrusions. Intrusions near the contact with overlying metamorphic rocks are variably deformed from a slight foliation to schistose and gneissic, and migmatites are abundant. The Mineral Ridge pluton exhibits petrologic and morphologic features such as an intimate association with amphibolite-grade regional metamorphism, indicating formation at considerable depths. The pluton and other sheet-like intrusions were deformed under ductile conditions and contacts are concordant to country rock foliation; thermal effects recorded in the host rocks are minimal, and the presence of magmatic muscovite suggests crystallization depths of at least 9-18 km (Figure 33) prior to Miocene extension (Diamond and Ingersoll, 2002). Three K-Ar ages from biotite and muscovite of leucogranite and two-mica granite from Mineral Ridge give cooling ages of ~42.1, 50.6, and 60.9 Ma (Albers and Stewart, 1972; Marvin, 1968), which imply burial depths of between 15 and 30 km in the early Cenozoic

based on Diamond and Ingersoll's (2002) assumptions for a geothermal gradient of between 10-20°/km. The fluids required to initiate melting may have been sourced from metamorphic breakdown of muscovite in more deeply buried rocks of the Wyman Fm. during prograde metamorphism (Miller and Gans, 1989), and/or transported along the major ore controlling shear zone (Reichardt and Weinberg, 2012). Neither this study nor previous reports have identified mafic xenoliths to suggest mafic input in crustal melting.

Pluton and Mineralization Ages

New U-Pb zircon dating (Table 1) establishes a Late Cretaceous crystallization age for both felsic intrusive phases at Mineral Ridge. Previous K-Ar and Ar-Ar biotite analyses for the pluton have reported Early Eocene crystallization ages, which are clearly cooling ages instead of approximating the age of intrusion, and suggest a prolonged duration between granite crystallization (~91.7 to 89.9 Ma) and the age that rocks cooled to below mica closure at ~300°C (~42 to 60 Ma). An Rb-Sr lepidolite age of ~700 Ma likely reflects lithophile mobility and is therefore, erroneous.

Cretaceous igneous ages on the Mineral Ridge and related intrusions expands the timing of gold mineralization to between ~90 and 13 Ma, the latter when post-mineralization dikes that cut ore zones cooled below $^{40}Ar/^{39}Ar$ groundmass feldspar closure temperatures in mafic dikes of approximately 250°C. Due to the indications that mineralization occurred at deep crustal depths and high temperatures, such as greenschist-facies wall rock inclusions and ductile to brittle-ductile ore textures, the age of mineralization is constrained to between the late Cretaceous (~92-90 Ma) and Eocene before the pluton cooled below the biotite and muscovite blocking temperature. A 76.0 ± 1.8 Ma U-Pb age from hydrothermal monazite analyzed in-situ from a mineralized quartz vein agrees with the time-temperature data, and constrains the gold event to the retrograde path of metamorphism in the western Sevier hinterland.

Orogenic Gold Mineralization

The main stage of gold mineralization at Mineral Ridge is defined by centimeter- to meter-scale, foliation-parallel, milky white quartz veins, deformed and attenuated by crustal-scale shearing. Intense shearing, including mylonitization, affects most of the lower plate-rocks including rocks of the Wyman Formation at and near its contacts with rheologically strong intrusive rocks and quartz bodies. Ore quartz is coarse grained and granoblastic, and contrasts from the late, barren, cryptocrystalline and post-deformation quartz veins that cut obliquely across foliation and have markedly different textures. Ribbon quartz and stylolite textures are formed by multiple phases of vein growth within brittle-ductile fractures are strong indicators of gold at Mineral Ridge and are characteristic of orogenic-type gold deposits worldwide (Vearncombe, 1993). These crack-seal quartz veins within and parallel to major ductile shear zones suggests that the fluid was channeled and focused through the shear zone during multiple seismic events (Sibson et al., 1988; Micklethwaite and Cox, 2004; Micklethwaite et al., 2015) that may have induced short intervals of dilatancy. Excepting the base-metal-rich, gossanous breccia zones in milky quartz veins at the Brodie pit, ore zones are less affected or unaffected by brittle deformation. It appears that gold-bearing fluids were transported mostly along shear planes during crustal-scale deformational events, eventually forming lens-shaped quartz bodies or lodes in areas the experienced the highest strain gradients, which commonly are granite-metasedimentary contacts and other areas of high rheological contrast. In a study of gold deposits in metamorphic terranes, the higher pressure and temperature orogenic gold deposits (≥400°C and ≥ 2.5kbars) are dominated by ductile deformation in broad shear zones and bedding-parallel veins, with common quartz recrystallization (Goldfarb et al., 2005). Brittle-ductile textures such as the ribbon-quartz (crack-seal) laminated veins common to Mineral Ridge suggest episodic growth at a shallower depth (Goldfarb et al., 2005; Pitcairn et al., 2014) than the ductile and bedding-parallel veins, and may represent continued activity as the deposit was being exhumed during cooling and crustal relaxation. However, gold deposition had ceased before reaching a brittle regime as no purely brittle features containing precious metals (i.e., discordant or tensional veins) are recorded at Mineral Ridge.

The Late Cretaceous between ~100 and 70 Ma was a dynamic time in eastern California and western Nevada that reflects the eastward propagation of Sevier crustal deformation. Large-scale contraction and associated deformation, metamorphism, and magmatism is documented in the eastern Sierra Nevada (Schweickert and Lahren, 1990; Greene and Schweickert, 1995; Tikoff and De Saint Blanquat, 1997; Coleman et al., 2003) as well as the region immediately to the east of the Sierra Nevada batholith, particularly in the White-Inyo Range and very near the Silver Peak Range (Sullivan and Law, 2007). In the White-Inyo, greenschist-facies regional metamorphism accompanied Cretaceous contractional and transpressional deformation between ~90 and 73 Ma, affecting ~91.7 Ma peraluminous granites and Wyman Formation metasedimentary rocks (Sullivan and Law, 2007), a nearly identical history to Mineral Ridge. Greenschist- to lower-amphibolite facies rocks affecting Wyman metasedimentary rocks at Mineral Ridge with tectonic foliations parallel to the foliated micas in two-mica granites are evidence of major tectonism, which is bracketed by the ~91.7 Ma U-Pb zircon age for the granite and the 55 Ma Ar-Ar biotite and 51 Ma K-Ar muscovite cooling ages that are interpreted as the time during which granites of the Mineral Ridge pluton passed below the ~300°C isotherm. Similar to other Cretaceous two-mica and leucocratic intrusions in the hinterland of the Sevier fold-and-thrust belt (Miller and Bradfish, 1980; Coney and Harms, 1984; Miller and Gans, 1989; Lee et al., 2003; Long and Soignard, 2016), a strong relationship is seen between mid to late Cretaceous deformation, metamorphism, magmatism, and in the case of Mineral Ridge, gold mineralization. Because gold mineralization at Mineral Ridge is related to regional lower-crustal processes of contractional deformation, metamorphism, and crustal partial melting, other orogenic gold deposits should exist where low- and mid-crustal rocks exhibiting late Mesozoic greenschist-grade metamorphism have been exhumed. Following a trend in orogenic gold systems of gold deposition occurring late in an evolving orogen (Saunders et al., 2013), a U-Pb monazite age suggests gold mineralization at Mineral Ridge occurred at approximately 76.0 ± 1.8 Ma, thus ~10-15 Ma after peak metamorphism and crustal partial melting. Gold deposition was contemporaneous with deformation during ductile to brittle-ductile conditions, as lodes are folded sub-parallel with large

(~300 m) open folds, and later overprinted by Miocene detachment faulting. and all gold-bearing quartz grains show deformation form undulatory extinction to shear bands with severe grain-size reduction. Isoclinal folds in gold-quartz veins, foliations in two-mica granites, and the deformation of mylonites are concordant with large-scale shear zones at Mineral Ridge. Mineralization occurred at elevated temperatures during retrograde greenschist-facies metamorphic conditions, and under conditions of brief thermal and chemical disequilibrium during gold-deposition perhaps induced by fault slip. Therefore, widespread metal zonation or alteration halos were not developed, and alteration and mineralization were largely restricted to ductile faults.
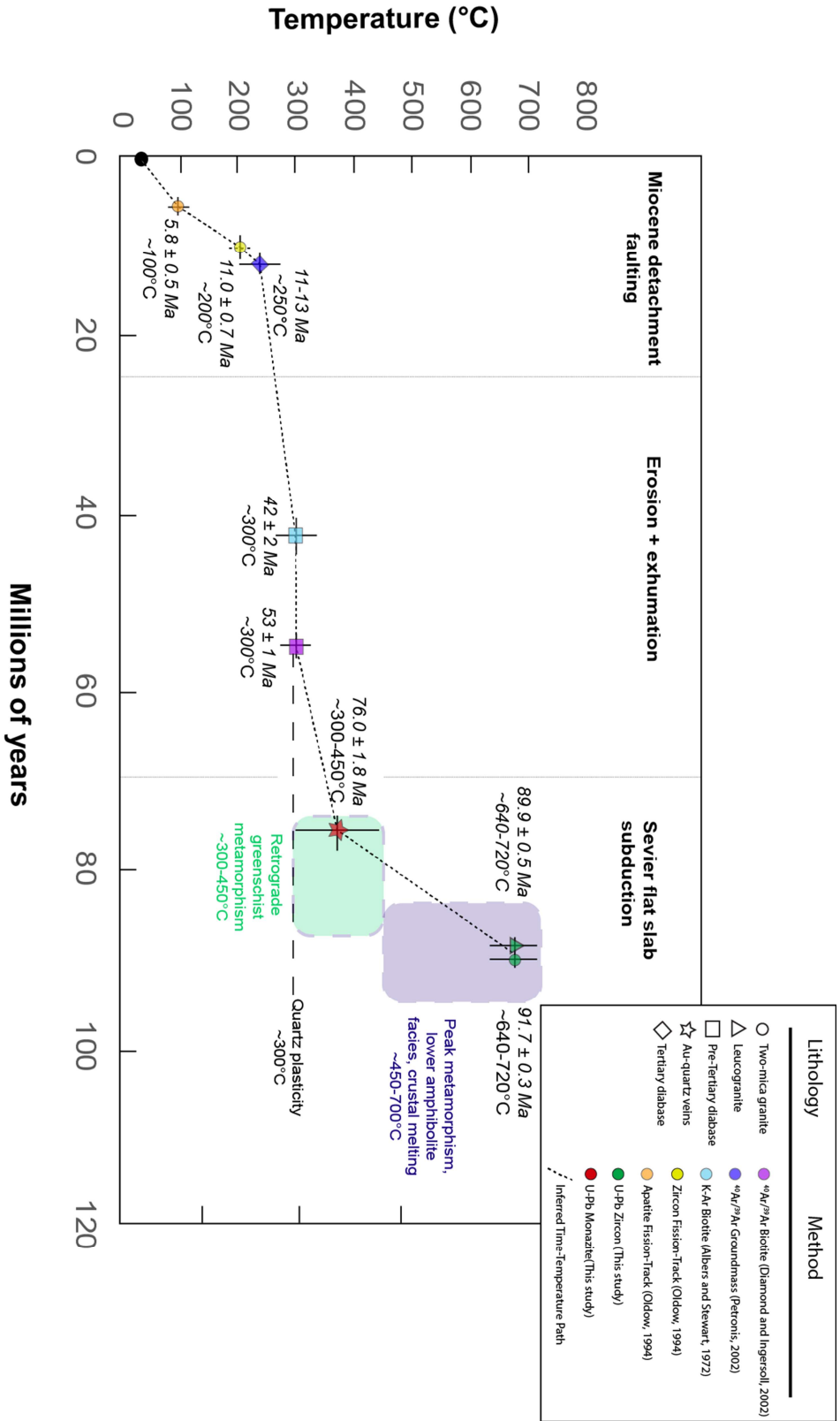
Figure 33. Time-temperature diagram for lower-plate rocks at Mineal Ridge. Pertinent U-Pb, Ar-Ar, fission-track age,s and closure temperatures plotted with estimated granite crystallization and regional metamorphic time-temperature ranges.

Comparison of Orogenic Gold Deposits Versus Reduced Intrusion-Related Gold Deposits

Gold mineralization characteristics at Mineral Ridge share common features with typical Phanerozoic orogenic gold systems, many of which are identified throughout the North American Cordillera from western Alaska to Sonora, Mexico. Orogenic gold deposits formed between the Early Cretaceous and the late Eocene (Izaguirre et al., 2017), including deposits in western Nevada dated between 90-70 Ma (Cheong, 2000). Commonalities with typical orogenic gold systems include their principal control by ductile or brittle-ductile shear zones, gold-dominant or gold-only character, sulfide-poor ore mineralogy, and foliation-parallel milky white quartz veins (Groves et al., 2003; Goldfarb and Groves, 2015). At Mineral Ridge, ore zones are hosted in Neoproterozoic passive margin carbonates and greenschist metamorphosed siliciclastic rocks, and Late Cretaceous peraluminous granitoids. Cordilleran orogenic deposits elsewhere most commonly occur in similar settings containing tight, well-foliated, siliceous metamorphic rocks derived from protoliths ranging from Proterozoic through Cretaceous in age (Goldfarb et al., 1998; Goldfarb et al., 2008). Typical quartz bodies at Mineral Ridge contain ubiquitous calcium-iron carbonates (ankerite, siderite), sericite and muscovite, chlorite, pyrite, and free gold, with variable amounts of galena, sphalerite, pyrrhotite, and monazite. Gold to silver ratios in orogenic gold systems are commonly 1 to 10 (Saunders et al., 2013), and Mineral Ridge averages 3.7. Foliation-parallel veins and ductile-shear zones are suggestive of a deep and hot (≥400°C and ≥ 2.5kbars) orogenic environment (Goldfarb et al., 2005), and ore zones lack mineralized veins that are discordant to foliation.

Orogenic gold systems in western Nevada are abundant and are associated with milky-white "mesothermal" quartz veins, Mesozoic or older metamorphic rocks, quartz-sericite-pyrite-carbonate alteration, and pre-mineral granitic intrusions (Cheong, 2000; Johnston et al., 2015). These deposits are Late Cretaceous in age; K-Ar and Ar-Ar ages of vein mica and potassium feldspar indicate mineralization ages between 114-72 Ma (Cheong, 2000). This timeframe is a good fit for the

mineralization age interpreted for Mineral Ridge, which occurred between granite intrusion at ~91.7 Ma and within the period of quartz plasticity (~300°C) until ~55 Ma. The 76.0 ± 1.8 Ma U-Pb monazite mineralization age further supports this interpretation. Like the tectonic implications hypothesized in this study, the Late Cretaceous shear-hosted deposits interpreted as orogenic Au-Ag deposits elsewhere in western Nevada are suggested to have formed during Sevier-related flat slab subduction, orogenesis, and metamorphism (Johnston et al., 2015) when arc magmatism was lacking.

Prior studies of gold mineralization at Mineral Ridge have focused on the granitic Mineral Ridge pluton as the source or driver of gold mineralization, citing pegmatite-derived gold (Spurr, 1906; Bercaw, 1986) or base-metal skarn system (Noland et al., 2014). These interpretations are primarily based on the close spatial relationship between ore bodies and granitic intrusions, tendency of pegmatites to grade into silica-rich veins, and associations between gold and base metals. In addition, the high bismuth contents of ores (generally, 1-50 ppm) at Mineral Ridge is commonly considered characteristic of deposits formed from magmatic fluids and has reinforced some interpretations that the deposits are skarns and/or of the reduced, intrusion-related type. However, bismuth is also a characteristic of many major orogenic deposits such as those in Kalgoorlie, western Australia and the Abitibi, eastern Canada, and is not regarded as proof of a magmatic source (e.g., Groves et al., 1998; Goldfarb and Groves, 2015). In addition, no direct transition from pegmatite veins to gold-bearing quartz veins have been observed in this study nor any evidence of skarn-type mineralization. The ubiquitous silica-rich pegmatite veins, which have a distinctive blue-gray color and often contain coarse muscovite, are in nearly all cases, barren of gold, except rarely where overprinted with Au-stage quartz.

Comparing Mineral Ridge to intrusion-related gold deposits is difficult because of the apparent continuum or overlap between deep-seated reduced intrusion-related gold (RIRG) systems and orogenic gold systems. Both systems may have ductile replacement quartz veins (Lang and

Baker, 2001), quartz-sericite-pyrite-carbonate alteration and mineralization assemblages, similar

elemental correlations to gold, small discrete alteration zones, and close spatial relationships with

granitic plutons (Hart, 2007). However, contrasting with typical RIRG deposits, Mineral Ridge

completely lacks sheeted vein systems or stockworks, disseminated ores, or known satellite deposits

of tungsten, molybdenum, or base-metal skarns. Typical intrusion-related gold granitoids are

reduced I-type (arc-type) intrusions with evidence of high volatile contents including an abundance

of hornblende, tourmaline, greisen alteration, and aplites (Hart, 2007), whereas the associated two-

mica granite and leucogranite at Mineral Ridge is a strongly peraluminous, S-type granite lacking

tourmaline, but does include ubiquitous pegmatite phases in its roof zone. Despite thick beds of

calcareous metasedimentary rocks capping the granitic intrusion at Mineral Ridge, no demonstrable

metasomatic skarns, bulk replacements of carbonate, or garnet-pyroxene or other calc-silicate

assemblages are found surrounding the pluton.

Table 2. Comparison of Mineral Ridge to possible deposit models. Sources for table: Bierlein and Crowe (2002), Goldfarb et al (1998), Goldfarb et al (2008), Groves (1998), Baker (2002), Hart (2007)

	Mineral Ridge	Cordilleran orogenic gold	Cordilleran (Deep) intrusion-related
Ore host rocks	Ductily deformed Neoproterozoic metamorphic (greenschist- to amphibolite-facies) miogeoclinal rocks and Late Cretaceous peraluminous leucogranites	Thick marine sequences at low-medium metamorphic grade	I-type felsic intrusions, metamorphic country rock
Hydrothermal minerals	Quartz, calcite, fe-carbonates, muscovite, pyrite, galena, sphalerite, monazite, native gold	Quartz, (Fe, Mg,Ca) carbonates, feldspar, mica, pyrite, arsenopyrite, native gold, base metal sulfides	K-spar, albite, muscovite, tourmaline, chlorite, cabronate, pyrrhotite, pyrite, loellingite, arsenopyrite,
Alteration	Carbonantization, chloritization, sericitization, desilicifation	Carbonitization, sericitization, sulfidation, albitization, chloritization	Albitization, greissen, silicification, carbonate, potassic
Mineralization styles	Concordant low-sulfide shear-hosted milky-white quartz bodies	Gold-quartz lodes in brittle-ductile to ductile shear systems	Low sulfide quartz forming sheeted vein systems, disseminated Au, stockwork, breccia, skarns
Tectonic control	Contractional/transpressional	Transpression and related uplift	Post-collisional extension (?)
Gold:Silver	4:1	1-10:1	1-5:1
Associated intrusions	S-type, catazonal, two-mica granite and pegmatitic leucogranite, high SiO$_2$	Granitic intrusions without clear connection to mineralization	I-type, metaluminous, moderately reduced, felsic intrusions
Mineralization age	Late Cretaceous (90-55 Ma, likely 76 Ma)	70-114 Ma (W. Nevada deposits), 52- 114 (North American Cordillera)	Jurassic-Eocene (Nevada deposits), Late Cretaceous (Alaska/Yukon)
Mineralization conditions	>10 km, 300-400°C	2-20 km, 250-400°C	2-8 km, >600 - <200°C

Exploration Potential

The recognition of Mineral Ridge as an orogenic gold system suggests that Sevier-related, amagmatic mineral deposits hosted in metamorphic terranes are a viable exploration target in western Nevada, at least where mid-crustal rocks have been exhumed to near the present surface in core complexes and other areas wherein greenschist and higher metamorphic grade rocks are exposed. Deformed metamorphic terranes in the western margin of the Sevier hinterland, especially greenschist-facies passive margin and volcanogenic rocks (Groves et al., 2003) such as the deeper parts of the Jurassic arc, are viable areas of exploration interest. Exploration for these terranes in the Walker Lane are aided by extensional tectonics necessary to exhume deep-crustal mineralization. The domal shape of many metamorphic core complexes should be regarded as structural highs bound by ductile shears that have a contractional history that predates Cenozoic detachment; such configurations are considered ideal for transporting and localizing deep-seated hydrothermal fluids. In addition, it seems that crustal melt granites of Late Cretaceous age in the western Sevier hinterland are a result of interactions between Sevier deformation, shear zones, and related metamorphism (Sullivan and Law, 2007), so one hypothesis is that coeval peraluminous granites in the Sevier tract may have undergone similar processes which contributed to gold mineralization at Mineral Ridge. Although this study suggests the gold mineralization occurred approximately 15 m.y. after granitic intrusions, the rheological contrast created by the intrusions was important to gold deposition and may create a similar contrast elsewhere. In addition, the broad processes that formed crustal-derived granites, namely deep burial and shear deformation, also relate to the orogenic gold deposits.

At the deposit scale, exploration targeting the shear zone should be further explored down-dip and along strike. The doubly plunging morphology of the Mineral Ridge anticline, especially to the north where not covered by upper-plate rocks, should be tested for continuation of the shear zone. Metamorphic gradients, changes in lithology and rheology, contacts with peraluminous

granites and shallowly-dipping pre-Tertiary diabase sills, and strong shear fabrics continue to be the main criteria for targeting ore zones.

Future Work

Future work on the Mineral Ridge gold deposit should focus on constraining the pressure, temperature, and chemical conditions at time of mineralization based on study of fluid inclusions, mineral assemblages, and stable isotopic analysis of ore-stage quartz. Gold-bearing quartz veins at Mineral Ridge are dense with small, 5-20 μm fluid inclusions and therefore, applicable for quantitative fluid inclusion studies, which would be a valuable contribution to understanding the fluid conditions of ore formation. Titanium in quartz thermometry (Wark and Watson, 2006) may also be a viable method for calculating temperatures of quartz formation. The estimation of a mineralization age was complicated by a complex thermal history (demonstrated by this study and Ingersoll and Diamond's (2002) analysis of Ar^{40}/Ar^{39} hornblende from a pre-mineral mafic sill) and low U and Th hydrothermal monazites. However, bulk separation of monazites and muscovite from quartz veins could result in a robust mineralization ages for the deposits. Constraining the timing and conditions of metamorphism in the lower plate at Mineral Ridge and conditions of crustal melting would be beneficial in making the link between Sevier deformation, metamorphism, magmatism, and gold mineralization in western Nevada.

Conclusions

Foliation-parallel Au-quartz veins at Mineral Ridge were emplaced in the Late Cretaceous, approximately 76.0 Ma, in a middle to deep crustal ductile shear zone under greenschist (muscovite ± chlorite ± epidote) metamorphic conditions that postdate and overprints amphibolite metamorphism. Gold mineralization was likely coincident with the late stages of Sevier orogenesis, which occurred over broad areas of the western U.S. between ~100 and 70 Ma, although Sevier deformation is not widely recognized in western Nevada. Thrusting and folding was accompanied by metamorphism of Cambrian and older rocks, folding and thrusting, magmatism, and development of ductile shear zones, and contemporaneous crustally derived peraluminous granites in the eastern

Sierra (Saleeby, 2003; Sullivan and Law, 2007). Brittle-ductile deformation was ongoing throughout gold deposition, evidenced by episodic crack-seal textures hosting gold and locally strongly deformed and mylonitized quartz veins, which are commonly folded and boudinaged. Previous paleobarometric analysis (Oldow et al., 1994; Diamond and Ingersoll, 2002) suggest the mineralized lower-plate exposed at surface at Mineral Ridge was between 9 and 18 km crustal depth prior to Miocene extension, although Au-bearing veins likely formed at even deeper levels in the late Cretaceous. Ductile to brittle-ductile textures in ore zones include foliation-parallel veins, ubiquitous mylonitzed quartz, stylolites, and ribbon-quartz. Ore zones are cm- to m-scale, low-sulfide, milky-white "bull quartz" veins and augens containing free gold and as inclusions in pyrite. Hydrothermal alteration associated with Au-bearing veins is limited to within a few meters of quartz bodies, and contains a consistent assemblage of quartz-sericite-pyrite-calcite ± chlorite ± siderite. Quartz veining post-dates the crustal derived catazonal 91.7 Ma Mineral Ridge two-mica granite and related leucogranite pegmatites, which likely formed during peak metamorphism (garnet-staurolite amphibolite) and prior to major NE-directed folding. Rheological anisotropies leading to intense shearing between the Mineral Ridge granite in the footwall and limy siliciclastic metasedimentary rocks of the Wyman Formation, are particularly evident along the NE-dipping east limb of the Mineral Ridge anticline and controlled emplacement of Au-bearing quartz bodies.

References

Albers, J.P., and Stewart, J.H., 1972, Geology and Mineral Deposits of Esmeralda County, Nevada: Nevada Bureau of Mines and Geology Bulletin 78, p. 80.

Armstrong, R.L., 1982, Cordilleran Metamorphic Core Complexes: Annual Reviews in Earth and Planetary Science, v. 10, p. 129–154.

Bailly, P.., 1951, Geology of the southeastern part of Mineral Ridge, Esmeralda County, Nevada: Unpublished PhD Dissertation: Stanford University, 186 p.

Barton, M.D., Girardi, J.D., Kreiner, D.C., Seedorff, E., Zurcher, L., Dilles, J.H., Haxel, G.B., and Johnson, D.A., 2011, Jurassic igneous-related metallogeny of southwestern North America: Great Basin Evolution and Metallogeny, p. 373–396.

Bercaw, L.B., 1986, Geology and gold deposits of central Mineral Ridge, Esmeralda County, Nevada: Unpublished M.S. Thesis: University of Colorado, Boulder, 156 p.

Bohlke, J.K., and Kistler, R.W., 1986, Rb-Sr, K-Ar, and stable isotope evidence for the ages and sources of fluid components of gold-bearing quartz veins in the northern Sierra Nevada foothills metamorphic belt, California.: Economic Geology, v. 81, no. 2, p. 296–322.

Bowring, J.F., McLean, N.M., and Bowring, S.A., 2012, Engineering cyber infrastructure for U-Pb geochronology: Tripoli and U-Pb-Redux: Geochemistry, Geophysics, Geosystems, v. 12, no. 6, 12 p.

Brown, S.M., Fletcher, I.R., Stein, H.J., Snee, L.W., G., and Groves, D.I., 2002, Geochronological Constraints on Pre-, Syn-, and Postmineralization Events at the World-Class Cleo Gold Deposit, Eastern Goldfields Province, Western Australia: Economic Geology, v. 97, p. 541–559.

Chang, Z., Vervoort, J.D., McClelland, W.C., and Knaack, C., 2006, U-Pb dating of zircon by LA-ICP-MS: Geochemistry, Geophysics, Geosystems, v. 7, no. 5, 14 p.

Cheong, S., 2000, General characteristics and structural evolution of metamorphic gold quartz veins in northwestern Nevada, U.S.A.: Geosciences Journal, v. 4, no. 2, p. 135–152.

Cherniak, D.J., Watson, E.B., Grove, M., and Harrison, T.M., 2004, Pb diffusion in monazite: A combined RBS/SIMS study: Geochimica et Cosmochimica Acta, v. 68, no. 4, p. 829–840.

Cline, J., 1986, The Sixteen-to-One epithermal silver-gold deposit, Esmeralda County, Nevada: a wall rock alteration and fluid inclusion study. Unpublished M.S. Thesis: University of Arizona, 102 p.

Coleman, D.S., Briggs, S., Glazner, A.F., and Northrup, C.J., 2003, Timing of plutonism and deformation in the White Mountains of eastern California Timing of plutonism and deformation in the White Mountains of eastern California: GSA Bulletin, v. 115, no. 1, p. 48–57.

Colgan, J.P., Howard, K.A., Fleck, R.J., and Wooden, J.L., 2010, Rapid middle Miocene extension and unroofing of the southern Ruby Mountains, Nevada: Tectonics, v. 29, 38 p.

Coney, P.J., and Harms, T.A., 1984, Cordilleran metamorphic core complexes: Cenozoic extensional relics of Mesozoic compression: Geology, v. 12, no. 9, p. 550–554.

Corfu, F., Hanchar, J.M., Hoskin, P.W.O., and Kinny, P., 2003, Atlas of Zircon Textures: Reviews in Mineralogy and Geochemistry, v. 53, no. 1, p. 32.

Cox, S.F., Wall, V.J., Etheridge, M.A., and Potter, T.F., 1991, Deformational and metamorphic processes in the formation of mesothermal vein-hosted gold deposits - examples from the Lachlan Fold Belt in central Victoria, Australia: Ore Geology Reviews, v. 6, no. 5, p. 391–423.

Diamond, D.S., 1990, Structural and Sedimentologic Evolution of an Extensional Orogen, Silver Peak Range and Adjacent Areas, West-Central Nevada: Unpublished PhD Dissertation: University of California, Los Angeles, 338 p.

Diamond, D.S., and Ingersoll, R. V., 2002, Structural and sedimentologic evolution of a Miocene supradetachment basin, Silver Peak Range and adjacent areas, west-central Nevada: International Geology Review, v. 44, no. January, p. 588–623.

Dickinson, W.R., 2006, Geotectonic Evolution of the Great Basin: Geosphere, v. 2, no. 7, p. 353–368.

Doebrich, J.L., Garside, L.J., and Shawe, D.R., 1996, Characterization of Mineral Deposits in Rocks of the Triassic to Jurassic Magmatic Arc: U.S. Geological Survey Open File Report 96-9.

Ernst, W.G., 1996, Petrochemical study of regional / contact metamorphism in metaclastic strata of the central White-Inyo Range, eastern California: Geological Society of America Bulletin, v. 108, no. 12, p. 1528–1548.

Faulds, J.E., and Henry, C.D., 2008, Tectonic influences on the spatial and temporal evolution of the Walker Lane: An incipient transform fault along the evolving Pacific – North American plate boundary: Arizona Geological Society Digest, v. 22, p. 437–470.

Fournier, Robert, O., 1991, The transition from hydrostatic to greater than hydrostatic fluid pressure in presently active continental hydrothermal systems in crystalline rock: Geophysical Research Letters, v. 18, no. 5, p. 955–958.

Frost, B.R., and Frost, C.D., 2008, A geochemical classification for feldspathic igneous rocks: Journal of Petrology, v. 49, no. 11, p. 1955–1969.

Goldfarb, R.J., and Groves, D.I., 2015, Orogenic gold: Common or evolving fluid and metal sources through time: Lithos, v. 233, p. 2–26.

Goldfarb, R.J., Hart, C.J.R., and Marsh, E.E., 2008, Orogenic gold and evolution of the Cordilleran orogen: Arizona Geological Society Digest, v. 22 , p. 311–323.

Goldfarb, R.J., Phillips, G.N., and Nokleberg, W.J., 1998, Tectonic setting of synorogenic gold deposits of the Pacific Rim: Ore Geology Reviews, v. 13, p. 185–218.

Goldfard, R.J., Baker, T., Dubé, B., Groves, D., Hart, C., and Gosselin, P., 2005, Distribution ,character, and genesis of gold deposits in metamorphic terranes: Economic Geology 100th Anniversary Volume, p. 407–450.

Greene, D.C., and Schweickert, R.A., 1995, The Gem Lake shear zone: Cretaceous dextral transpression in the Northern Ritter Range pendant, eastern Sierra Nevada, California: Tectonics, v. 14, no. 4, p. 945–961.

Groves, D.I., Goldfarb, R.J., Gebre-Mariam, M., Hagemann, S.G., and Robert, F., 1998, Orogenic gold deposits: a proposed classification in the context of their crustal distribution and relationship to other gold deposit types: Ore Geology Reviews, v. 13, no. 1–5, p. 7–27.

Groves, D.I., Goldfarb, R.J., Knox-Robinson, C.M., Ojala, J., Gardoll, S., Yun, G.Y., and Holyland, P., 2000, Late-kinematic timing of orogenic gold deposits and significance for computer-based exploration techniques with emphasis on the Yilgarn Block, Western Australia: Ore Geology Reviews, v. 17, no. 1–2, p. 1–38.

Groves, D.I., Goldfarb, R.J., Robert, F., and Hart, C.J.R., 2003, Gold deposits in metamorphic belts: Overview of current understanding, outstanding problems, future research and exploration significance: Economic Geology, v. 98, no. 1, p. 1–29.

Harrison, T.M., Catlos, E.J., and Montel, J.-M., 2002, U-Th-Pb dating of phosphate minerals: Reviews in Mineralogy and Geochemistry, v. 48, no. 1, p. 524–558.

Harrison, T.M., Duncan, I., and McDougall, I., 1985, Diffusion of 40Ar in biotite: Temperature, pressure and compositional effects: Geochimica et Cosmochimica Acta, v. 49, no. 11, p. 2461–2468.

Hart, C.J.R., 2007, Reduced Intrusion-related gold systems: Mineral deposits of Canada: A synthesis of major deposit types, district metallogeny, the evolution of geological provinces, and exploration methods: Geological Association of Canada, Mineral Deposits Division, Special Publication No. 5, v. 5, p. 95–112.

Howard, K.A., 2003, Crustal structure in the Elko-Carlin Region, Nevada, during Eocene gold mineralization: Ruby-East Humboldt metamorphic core complex as a guide to the deep crust: Economic Geology, v. 98, no. 2, p. 249–268.

Howard, K.A., Wooden, J.L., Barnes, C.G., Premo, W.R., Snoke, A.W., Lee, S.Y., 2011, Episodic growth of a Late Cretaceous and Paleogene intrusive complex of pegmatitic leucogranite, Ruby Mountains core complex, Nevada, USA: Geosphere, v. 7, no. 5, p. 1220.

Hruska, D.C., Deng, Q., and Kilby, D., 1996, Geology of the Mary/Drinkwater gold deposit, Esmeralda County, Nevada: Internal company report, Mineral Ridge Resources, Inc, 21 p.

Izaguirre, A., Iriondo, A., Kunk, M.J., McAleer, R.J., Atkinson, W.W., and Martínez-Torres, L.M., 2017, Tectonic framework for late cretaceous to eocene quartz-gold vein mineralization from the caborca orogenic gold belt in Northwestern Mexico: Economic Geology, v. 112, no. 6, p. 1509–1529.

Johnston, M.K., Coleman, K.N., and Ressel, M.W., 2015, Late Cretaceous orogenic Au-Ag vein deposits of western and north-central Nevada : Consequences of Sevier flat-slab subduction, and links with other Cordilleran orogenic deposits: Geological Society of Nevada 2015 Symposium, p. 583–610.

Keith, W.J., Silbemlan, M.L., and Erd, R.C., 1976, K-Ar age of mineralization, Silver Peak (Red Mountain) mining district, Esmeralda County, Nevada: Isochron/West, , no. 16, p. 13–14.

Kelley, S., 2002, K-Ar and Ar-Ar Dating: Reviews in Mineralogy and Geochemistry, v. 47, no. 1, p. 785–818.

Kempe, U., Lehmann, B., Wolf, D., Rodionov, N., Bombach, K., Schwengfelder, U., and Dietrich, A., 2008, U-Pb SHRIMP geochronology of Th-poor, hydrothermal monazite: An example from the Llallagua tin-porphyry deposit, Bolivia: Geochimica et Cosmochimica Acta, v. 72, no. 17, p. 4352–4366.

Kerrick, D.M., 1972, Experimental determination of muscovite + quartz stability with P H2O total: American Journal of Science, v. 272, no. 10, p. 946–958.

Kirsch, S. A., 1971, Chaos structure and turtleback dome, Mineral Ridge, Esmeralda County, Nevada: Geological Society of America Bulletin, v. 82, no. 11, p. 3169.

Kirsch, S.A., 1968, Structure of the metamorphic and sedimentary rocks of Mineral Ridge, Esmeralda County, Nevada: Unpublished PhD dissertation, University of California, Berkeley , PhD., 128 p.

Kohn, M.J., and Vervoort, J.D., 2008, U-Th-Pb dating of monazite by single-collector ICP-MS: Pitfalls and potential: Geochemistry, Geophysics, Geosystems, v. 9, no. 4.

Lang, J.R., and Baker, T., 2001, Intrusion-related gold systems: The present level of understanding: Mineralium Deposita, v. 36, no. 6, p. 477–489.

Lee, S., Barnes, C.G., Arthur, W., Keith, S., Carol, A.H., Snoke, A.W., Howard, K.A., and Frost, C.D., 2003, Petrogenesis of Mesozoic, peraluminous granites in the Lamoille Canyon area, Ruby Mountains, Nevada, USA: Journal of Petrology, v. 44, no. 4, p. 713–732.

Long, S.P., and Soignard, E., 2016, Shallow-crustal metamorphism during Late Cretaceous anatexis in the Sevier hinterland plateau: Peak temperature conditions from the Grant Range, eastern Nevada, U.S.A.: Lithosphere, v. 8, no. 2, p. 150–164.

Micklethwaite, S., and Cox, S.F., 2004, Fault-segment rupture, aftershock-zone fluid flow, and mineralization: Geology, v. 32, no. 9, p. 813–816.

Micklethwaite, S., Ford, A., Witt, W., and Sheldon, H.A., 2015, The where and how of faults, fluids and permeability - insights from fault stepovers, scaling properties and gold mineralisation: Geofluids, v. 15, no. 1–2, p. 240–251.

Middlemost, E.A.K., 1994, Naming materials in the magma igneous rock system: Earth-Science Reviews, v. 37, no. 1994, p. 215–224.

Miller, C.F., and Bradfish, L.J., 1980, An inner Cordilleran belt of muscovite-bearing plutons: Geology, v. 8, no. 9, p. 412–416.

Miller, E.L., and Gans, P.B., 1989, Cretaceous crustal structure and metamorphism in the hinterland of the Sevier thrust belt, western US Cordillera: Geology, v. 17, no. 1, p. 59–62.

Noland, P.D., Briscoe, S., and Hawley, P.J., 2014, Genesis and timing of gold mineralization at Mineral Ridge, Esmeralda County, Nevada, and implications for future exploration and discovery: New concepts and discoveries: Geological Society of Nevada 2015 Symposium Proceedings, p. 843-858.

Oldow, J.S., Kohler, G., and Donelick, R.A., 1994, Late Cenozoic extensional transfer in the Walker Lane strike-slip belt, Nevada: Geology, v. 22, July, p. 637–640.

Petronis, M.S., Geissman, J.W., Oldow, J.S., and McIntosh, W.C., 2002, Paleomagnetic and 40Ar/39Ar geochronologic data bearing on the structural evolution of the Silver Peak extensional complex, west-central Nevada: Geological Society of America Bulletin, v. 114, no. 9, p. 1108–1130.

Pitcairn, I.K., Craw, D., and Teagle, D.A.H., 2014, The gold conveyor belt: Large-scale gold mobility in an active orogen: Ore Geology Reviews, v. 62, p. 129–142.

Poitrasson, F., Chenery, S., and Bland, D.J., 1996, Contrasted monazite hydrothermal alteration mechanisms and their geochemical implications: Earth and Planetary Science Letters, v. 145, p. 79–96.

Rasmussen, B., Sheppard, S., and Fletcher, I.R., 2006, Testing ore deposit models using in situ U-Pb geochronology of hydrothermal monazite: Paleoproterozoic gold mineralization in northern Australia: Geology, v. 34, no. 2, p. 77–80.

Reheis, M.C., Sawyer, T.L., Survey, U.S.G., and Road, S.F., 1997, Late Cenozoic history and slip rates of the Fish Lake Valley, Emigrant Peak , and Deep Springs fault zones , Nevada and California: Geological Society of America Bulletin, v.109, no. 3, p. 280–299.

Reichardt, H., and Weinberg, R.F., 2012, The dike swarm of the Karakoram shear zone , Ladakh , NW India : Linking granite source to batholith: The dike swarm of the Karakoram shear zone, v.124, no. 1, p. 89–103.

Renne, P.R., Swisher, C.C., Deino, A.L., Karner, D.B., Owens, T.L., and DePaolo, D.J., 1998, Intercalibration of standards, absolute ages and uncertainties in Ar-40/Ar-39 dating: Chemical Geology, v. 145, no. 1–2, p. 117–152.

Ridley, J.R., and Diamond, L.W., 2000, Fluid chemistry of orogenic lode gold deposits and implications for genetic models: Reviews in Economic Geology, v. 13, p. 141–162.

Roering, C., and Smit, C.A., 1987, Bedding-parallel shear, thrusting and quartz vein formation in Witwatersrand quartzites: Journal of Structural Geology, v. 9, no. 4, p. 419–427.

Rose, A.W., Hawkes, H.E., Webb, J.S., 1979, Geochemistry in Mineral Exploration: Shamberger, London.

Saleeby, J., 2003, Segmentation of the Laramide Slab - Evidence from the southern Sierra Nevada region: Bulletin of the Geological Society of America, v. 115, no. 6, p. 655–668.

Sarma, D.S., McNaughton, N.J., Fletcher, I.R., Groves, D.I., Mohan, M.R., and Balaram, V., 2008, Timing of gold mineralization in the Hutti gold deposit, Dharwar craton, South India: Economic Geology, v. 103, no. 8, p. 1715–1727.

Saunders, J.A., Hofstra, A.H., Goldfarb, R.J., and Reed, M.H., 2013, Geochemistry of Hydrothermal Gold Deposits: Elsevier Ltd.

Schandl, E.S., and Gorton, M.P., 2004, A textural and geochemical guide to the identification of hydrothermal monazite: criteria for selection of samples for dating epigenetic hydrothermal ore deposits: Economic Geology, v. 99, p. 1027–1035.

Schilling, J.H., 1965, Isotopic age determinations of Nevada rocks: Nevada Bureau of Mines Report No. 10.

Schleicher, H., and Lippolt, H.J., 1982, Magmatic muscovite in felsitic parts of rhyolites from Southwest Germany: Contributions to Mineralogy and Petrology, v. 78, no. 3, p. 220–224.

Schweickert, R.A., and Lahren, M.M., 1990, Speculative reconstruction of the Mojave-Snow Lake Fault: implications for Paleozoic and Mesozoic orogenesis in the western United States: Tectonics, v. 9, no. 6, p. 1609–1629.

Sibson, R.H., Robert, F., and Poulsen, K.H., 1988, High-angle reverse faults, fluid-pressure cycling, and mesothermal gold-quartz deposits: Geology, v. 16, no. 6, p. 551–555.

Sillitoe, R.H., 2008, Major gold deposits and belts of the North and South American Cordillera; distribution, tectonomagmatic settings, and metallogenic considerations: Economic Geology and the Bulletin of the Society of Economic Geologists, v. 103, no. 4, p. 663–687.

Sindern, S., Gerdes, A., Ronkin, Y.L., Dziggel, A., Hetzel, R., and Schulte, B.A., 2012, Monazite stability, composition and geochronology as tracers of Paleoproterozoic events at the eastern margin of the East European Craton (Taratash complex, Middle Urals): Lithos, v. 132–133, p. 82–97.

Spurr, J.E., 1906, Ore Deposits of the Silver Peak Quadrangle, Nevada. USGS Professional Paper no. 55, 174 p.

Steiger, R.H., and Jager, E., 1977, Subcommision on geochronology: convention on the use of decay constants in geo- and cosmochronology: Earth and Planetary Science Letters, v. 36, p. 359–362.

Stewart, J.H., 1970, Upper Precambrian and Lower Cambrian Strata, in the Southern Great Basin California and Nevada: U.S. Geological Survey Professional Report 620, 206 p.

Stipp, M., Stünitz, H., Heilbronner, R., and Schmid, S.M., 2002, The eastern Tonale fault zone: A "natural laboratory" for crystal plastic deformation of quartz over a temperature range from 250 to 700 °C: Journal of Structural Geology, v. 24, no. 12, p. 1861–1884.

Sullivan, W.A., and Law, R.D., 2007, Deformation path partitioning within the transpressional White Mountain shear zone, California and Nevada: Journal of Structural Geology, v. 29, no. 4, p. 583–599.

Taylor, R.D., Goldfarb, R.J., Monecke, T., Fletcher, I.R., Cosca, M.A., and Kelly, N.M., 2015, Application of U-Th-Pb phosphate geochronology to young orogenic gold deposits : New age constraints on the formation of the Grass Valley gold district, Sierra Nevada foothills province, California: Economic Geology, v. 110, p. 1313–1337.

Tikoff, B., and De Saint Blanquat, M., 1997, Transpressional shearing and strike-slip partitioning in the Late Cretaceous Sierra Nevada magmatic arc, California: Tectonics, v. 16, no. 3, p. 442–459.

Vearncombe, J.R., 1993, Quartz vein morphology and implications for formation depth and classification of Archaean gold-

vein deposits: Ore Geology Reviews, v. 8, no. 5, p. 407–424.

Viljoen, B., 1996, Underground Mary Mine development plan, Internal company report, Golden Phoenix Minerals, Inc., 42 p.

Villaros, A., Stevens, G., and Buick, I.S., 2009, Lithos Tracking S-type granite from source to emplacement : Clues from garnet in the Cape Granite Suite: LITHOS, v. 112, no. 3–4, p. 217–235.

Wark, D.A., and Watson, E.B., 2006, TitaniQ: A titanium-in-quartz geothermometer: Contributions to Mineralogy and Petrology, v. 152, no. 6, p. 743–754.

Wells, M.L., Hoisch, T.D., Cruz-Uribe, A.M., and Vervoort, J.D., 2012, Geodynamics of synconvergent extension and tectonic mode switching: Constraints from the Sevier-Laramide orogen: Tectonics, v. 31, no. 1, p. 1–21.

Wendt, I., and Carl, C., 1991, The statistical distribution of the mean squared weighted deviation: Chemical Geology: Isotope Geoscience Section, v. 86, no. 4, p. 275–285.

Wesnousky, S.G., 2005, The San Andreas and Walker Lane fault systems , western North America : transpression , transtension , cumulative slip and the structural evolution of a major transform plate boundary: Journal of Structural Geology, v. 27, p. 1505–1512.

White, A.J.R., and Chappell, B.W., 1988, Some supracrustal (S-type) granites of the Lachlan Fold Belt: Transactions of the Royal Society of Edinburgh: Earth Sciences, v. 79, no. 2–3, p. 169–181.

Yonkee, A.W., Weil, A.B., 2015, Tectonic evolution of the Sevier and Laramide belts within the North American Cordillera orogenic system: Earth-Science Reviews, v. 150, p. 531–593.

Appendix

Appendix A-1 : Geochemical data of vein material

Sample		71803	MR69-323	Sol519E	71107	71602	71603	71502	729qtz	71312	71201
ALS name		MR1623	MR1628	MR17-28	MR1614	MR1619	MR1621	MR1609	MR1636	MR1634	MR17-26
Lithology		Fe-Ox	BM Qtz	RibQtz	BM Qtz	RibQtz	Mrbl	RibQtz	Mass	RibQtz	Fe-Ox
Easting		436402	-	436519	436770	437181	437181	437158	437152	437938	-
Northing		4183208	-	4183522	4182690	4182489	4182489	4183862	4182442	4183577	-
Recvd Wt.	kg	1.13	2.23	1.24	2.61	1.28	1.34	1.58	2.66	1.8	3.18
Au	ppm	49.7	33	32.6	31.4	23.2	17.55	15.85	12.6	10.7	7.47
Ag	ppm	14.8	21.6	3.8	19.15	2.92	17.75	3.12	1.69	3.28	0.48
Al	%	0.07	0.59	0.2	0.08	3.6	3.55	0.42	0.1	1.26	0.75
As	ppm	39.2	16.3	53.2	3.2	11.6	16.6	9.7	13.9	14	66.4
Ba	ppm	10	70	15	10	350	480	60	20	180	33
Be	ppm	0.08	0.4	0.17	<0.05	1.89	1.77	0.24	0.13	0.51	0.41
Bi	ppm	23.4	12	1.92	32.6	2.01	47.7	5.36	11.9	0.66	1.305
Ca	%	0.09	0.18	0.01	0.01	3.68	5.03	0.04	0.02	1.17	0.61
Cd	ppm	0.41	83.6	0.541	1.67	0.19	0.88	0.04	0.09	0.2	0.061
Ce	ppm	0.75	4.96	0.89	0.32	18.6	18.6	5.46	3.43	7.89	4.92
Co	ppm	0.8	1.2	15.15	0.5	8.8	9	2.1	0.7	10.4	8.85
Cr	ppm	35	53	59.3	77	63	60	97	74	113	89.6
Cs	ppm	0.07	0.2	0.14	<0.05	0.59	0.6	0.21	0.06	0.48	0.51
Cu	ppm	12.3	5	45.9	16.1	20.4	33.2	7.8	4.7	24.8	32.5
Fe	%	1.06	1.07	2.14	0.7	2.21	2.17	0.96	0.98	2.1	2.32
Ga	ppm	0.48	2.87	1.21	0.43	12.75	13.4	2.02	0.8	5.34	3.44
Ge	ppm	0.11	0.14	<0.05	0.12	0.15	0.14	0.12	<0.05	<0.05	<0.05
Hf	ppm	<0.1	<0.1	0.005	<0.1	0.1	0.1	0.1	<0.1	0.2	0.095
In	ppm	0.029	0.387	0.009	0.054	0.042	0.046	0.009	0.01	0.012	<0.005
K	%	0.03	0.36	0.09	0.03	1.67	2.12	0.19	0.08	0.52	0.18
La	ppm	0.5	2.6	0.487	<0.5	9.4	9.4	2.9	1.9	3.9	2.63
Li	ppm	2.4	3.8	4.2	1.3	11.4	9.5	3.9	1	11.4	23.3
Mg	%	0.01	0.05	0.02	0.01	0.23	0.25	0.07	0.01	0.53	0.27
Mn	ppm	49	71	68.4	60	515	556	83	61	163	245
Mo	ppm	4.89	11.25	3.72	4.58	3.88	3.42	5.85	4.52	3.88	5.67
Na	%	0.01	0.01	0.006	0.02	0.45	0.24	0.01	0.01	0.03	0.032
Nb	ppm	0.1	1.6	0.805	0.1	6.9	6.3	1.3	0.5	2.1	3.01
Ni	ppm	2.3	3.5	13.6	2.8	5.7	8.3	5.1	2.8	13.3	18.4
P	%	0.002	0.006	0.001	0.001	0.015	0.016	0.004	0.004	0.016	0.007
Pb	ppm	1320	10600	53.4	4460	11.9	554	47.7	110	139	7
Rb	ppm	1.5	15.9	4.39	1.2	77.8	89.9	8.5	3.7	19.9	10.95
Re	ppm	0.002	0.002	<0.002	<0.002	0.002	<0.002	<0.002	<0.002	<0.002	<0.002
S	%	0.07	1.14	1.36	0.07	0.55	1.03	0.02	0.11	0.77	0.01
Sb	ppm	3.1	1.55	1.85	0.28	0.56	1.07	0.39	1.19	0.66	2.77
Sc	ppm	0.2	0.6	0.2	0.1	2.2	2.4	0.6	0.1	2.9	1.29
Se	ppm	<1	2	0.4	1	1	1	<1	1	1	0.2
Sn	ppm	0.2	0.7	0.23	0.2	2.3	2.3	0.4	0.2	0.6	0.39
Sr	ppm	7.3	24	3.33	3.8	151.5	362	7.4	14.7	67.3	19.8
Ta	ppm	<0.05	0.08	0.09	<0.05	0.83	0.64	0.07	0.06	0.15	0.08
Te	ppm	2.36	2.1	0.27	1.59	0.45	1.57	0.36	1.52	0.08	0.51
Th	ppm	0.09	1.01	0.257	0.11	4.25	3.92	0.78	0.42	1.17	0.604
Ti	%	<0.005	0.021	0.005	<0.005	0.06	0.065	0.018	0.006	0.053	0.024
Tl	ppm	0.15	0.09	0.105	0.03	0.32	0.42	0.06	0.14	0.12	0.257
U	ppm	0.6	1.7	1.38	0.3	4	4.9	0.2	0.3	1.3	1.62
V	ppm	7	6	2	<1	13	15	5	1	22	11.7
W	ppm	0.3	1.2	0.229	0.1	4.3	4.8	1	0.3	2.8	0.477
Y	ppm	1.1	0.8	0.51	0.1	7.4	7.7	1.6	0.5	2.3	2.48
Zn	ppm	123	12050	97.5	261	25	86	15	23	40	32.2
Zr	ppm	<0.5	2.2	0.2	<0.5	4.8	4.3	1.4	<0.5	3	2.9

Sample		71402	729Iron	71604	MR6510	709BR2	71006	70903	71711	71308	71708	71704
ALS name		MR-009	MR1637	MR1604	MR1615	MR17-27	MR1618	MR1624	MR1620	MR1633	MR1617	MR1605
Lithology		Mass	Fe-Ox	RibQtz	RIbQtz	Fe-Ox	Fe-Ox	Mass	RibQtz	Mass	Fe-Ox	AltMafic
Easting		436857	437152	437181	438435	437127	436546	437735	436337	437797	436403	436403
Northing		4182802	4182442	4182489	4183288	4182409	4183488	4183712	4183249	4183561	4183200	4183200
Recvd Wt.	kg	0.5	1.84	1.79	2.55	0.64	2.3	1.04	0.5	1.82	1.24	1.27
Au	ppm	6.1	5.3	5.2	4.87	4.2	3.14	1.815	1.68	1.54	1.49	1.315
Ag	ppm	1.37	2.93	0.71	1.06	16.2	0.61	1.98	1.31	1.03	0.35	0.25
Al	%	0.07	1.2	0.57	1.02	0.07	0.19	0.06	1.69	1.01	0.87	5.78
As	ppm	47.6	59.4	3.2	2.2	21.9	13.7	22.5	6.5	7	4.3	5
Ba	ppm	6	100	60	220	31	30	20	310	190	180	570
Be	ppm	0.04	1.08	0.36	0.56	0.25	0.16	0.05	0.78	0.3	0.33	2.13
Bi	ppm	0.691	9.01	1.31	0.27	26	1.49	2.63	0.99	0.17	0.23	0.76
Ca	%	0.05	0.04	0.91	0.65	0.02	0.01	0.02	5.39	0.75	0.55	3.96
Cd	ppm	0.07	1.61	0.08	0.02	0.119	<0.02	0.04	0.34	0.15	0.3	0.7
Ce	ppm	0.63	5.79	3.58	6.4	0.47	1.38	0.69	21.1	10.85	6.53	48.1
Co	ppm	16.45	11.2	2.4	1.1	1.09	0.4	0.7	4.1	0.9	2.4	16.3
Cr	ppm	20.1	35	86	62	44.7	92	61	62	39	59	257
Cs	ppm	0.09	0.31	0.15	0.34	0.09	0.15	0.05	0.54	0.19	0.53	1.61
Cu	ppm	8.3	53.1	13.1	4.5	10.05	2.3	2.4	10	3	21.3	11
Fe	%	4.55	5.18	0.92	0.6	1.81	0.6	0.83	0.9	0.61	0.95	4.22
Ga	ppm	0.35	4.11	2.35	4	0.75	0.86	0.37	6.46	2.88	3.68	18.7
Ge	ppm	<0.05	<0.05	0.12	<0.05	0.15	0.1	0.21	0.16	0.05	0.11	0.2
Hf	ppm	0.014	<0.1	<0.1	<0.1	0.004	0.2	<0.1	0.2	<0.1	<0.1	1
In	ppm	0.005	0.014	0.011	0.008	<0.005	<0.005	0.005	0.038	0.006	0.011	0.043
K	%	0.02	0.36	0.28	0.76	0.16	0.1	0.04	0.63	0.63	0.45	1.44
La	ppm	0.298	3.1	1.9	3.4	0.389	0.8	<0.5	10.1	6	3.5	24.5
Li	ppm	0.9	11.5	3.1	3.4	2.1	5.5	1.4	10.5	1.6	11.5	52.7
Mg	%	0.04	0.05	0.07	0.06	<0.01	0.01	<0.01	0.31	0.04	0.12	2.63
Mn	ppm	43.5	198	154	69	80.2	49	51	454	87	140	578
Mo	ppm	1	8.49	4.95	3.73	2.81	5.13	3.57	3.05	2.16	3.95	3.69
Na	%	0.012	0.02	0.01	0.09	0.031	0.01	0.01	0.27	0.29	0.09	0.81
Nb	ppm	0.143	1.4	1.5	2.1	0.25	0.8	0.2	4.1	2.2	2.2	10.7
Ni	ppm	6.35	12.8	3.2	4.8	3.7	2.5	2.5	10.4	3.2	4.5	107.5
P	%	0.001	0.024	0.003	0.009	0.006	0.001	0.001	0.013	0.007	0.004	0.073
Pb	ppm	90.2	104	6.4	87.2	538	8.9	214	141.5	19.8	22.2	7.7
Rb	ppm	0.9	18.2	13.8	30.6	7.35	5.4	1.4	30.4	22.4	18	83.7
Re	ppm	<0.002	<0.002	<0.002	<0.002	<0.002	<0.002	<0.002	<0.002	<0.002	<0.002	0.002
S	%	4.63	0.03	0.1	0.02	0.38	0.04	0.17	0.01	0.24	<0.01	<0.01
Sb	ppm	0.31	4.88	0.39	0.14	2.45	1.13	0.94	0.26	1.13	0.31	0.28
Sc	ppm	0.19	0.8	0.5	0.7	0.11	0.2	0.1	2.5	0.5	1.1	11.8
Se	ppm	<0.2	2	<1	<1	0.6	<1	<1	<1	<1	<1	1
Sn	ppm	0.16	0.5	0.5	0.8	0.1	0.3	0.2	1.2	0.5	0.6	2.1
Sr	ppm	4.8	18.5	50.7	48	15.85	7.1	3.7	262	86	47.2	222
Ta	ppm	0.01	0.15	0.15	0.15	0.01	0.08	<0.05	0.27	0.15	0.17	0.98
Te	ppm	0.14	0.65	0.21	0.05	1.59	0.19	0.11	0.33	<0.05	<0.05	0.3
Th	ppm	0.069	1.25	0.8	1.35	0.162	0.13	0.12	3.37	1.35	1.09	5.59
Ti	%	0.004	0.016	0.014	0.027	0.002	0.007	<0.005	0.066	0.026	0.025	0.263
Tl	ppm	0.016	0.29	0.07	0.18	0.268	0.09	<0.02	0.14	0.14	0.09	0.5
U	ppm	0.28	3.5	1.2	0.6	0.49	0.2	0.2	0.7	0.3	0.4	2.3
V	ppm	1.3	5	3	8	0.9	1	1	16	4	10	87
W	ppm	0.114	0.8	0.7	1.9	0.15	0.4	0.2	2.4	2.2	0.7	5.1
Y	ppm	0.23	2.1	1.7	1.1	0.53	0.5	0.1	5.5	1.4	2.1	13.3
Zn	ppm	19.8	310	20	34	31.5	3	10	49	39	85	97
Zr	ppm	0.5	<0.5	0.5	1.1	0.1	1	<0.5	1.9	0.5	0.7	44.4

Sample		71002	71403	Dwlamp	71709	71106	71004	Blu	61503	NW DW	62501	61910
ALS name		MR-004	MR1606	MR1613	MR-008	MR17-25	MR-006	MR-007	MR-001	MR-003	MR1601	MR1602
Lithology		Late	RibQtz	AltMafic	AltMafic	Mass	Late	AltMafic	AltGrn	RibQtz	AltGrn	Late
Easting		436945	436857	437993	436337	436782	436998	436402	436589	437843	436914	439165
Northing		4183557	4182802	4183618	4183249	4182731	4183569	4183208	4183451	4183723	4183542	4183004
Recvd Wt.	kg	0.7	0.89	0.42	1.32	1.2	0.54	1.06	0.96	0.52	0.28	0.9
Au	ppm	0.015	0.013	0.013	0.012	0.011	0.008	0.008	0.007	0.007	0.003	0.002
Ag	ppm	2.33	0.18	0.14	0.057	0.125	0.302	0.174	0.068	0.049	0.25	0.04
Al	%	1.22	0.66	1.88	4.04	0.52	3.78	4.68	6.12	2.48	0.78	0.23
As	ppm	2.73	8.6	3.2	17.25	14.05	3.19	1.96	2.7	2.74	0.6	0.8
Ba	ppm	164	80	100	216	91	460	620	155	204	110	10
Be	ppm	0.51	0.34	0.61	0.82	0.21	0.81	1.06	2.89	1.73	0.36	0.17
Bi	ppm	1.21	0.18	0.09	0.18	0.104	0.251	0.078	0.032	0.058	0.37	0.02
Ca	%	0.12	0.05	2.12	7.76	0.04	0.25	4.47	0.5	6.45	0.04	0.03
Cd	ppm	0.426	0.06	0.03	0.203	0.296	0.088	0.07	<0.005	0.055	0.06	0.03
Ce	ppm	7.6	4.32	11.35	32.1	1.51	17.25	54.1	5.47	29	1.37	0.32
Co	ppm	2.25	0.9	6.8	9.53	2.24	0.797	36.3	0.721	0.748	0.4	0.4
Cr	ppm	43.5	88	144	206	33.5	12	277	15.6	29.8	20	25
Cs	ppm	0.3	0.19	0.34	0.35	0.21	0.56	12.15	1.46	0.74	0.11	0.26
Cu	ppm	197.5	2.5	4.8	5.29	9.4	2.81	53.8	2.8	4.02	1.8	2
Fe	%	0.9	0.6	1.65	5.06	0.76	0.53	4.73	0.43	1.52	0.33	0.44
Ga	ppm	4.61	3.2	6.74	16	1.29	7.21	12.2	18.6	9.01	1.46	1.03
Ge	ppm	<0.05	0.14	0.17	0.08	<0.05	<0.05	0.11	<0.05	0.09	0.14	0.14
Hf	ppm	0.522	0.1	0.2	0.616	0.008	0.024	1.5	0.369	0.204	<0.1	<0.1
In	ppm	0.03	0.008	0.016	0.016	<0.005	<0.005	0.04	0.005	0.031	0.007	<0.005
K	%	0.37	0.47	0.42	0.68	0.16	1.21	1.25	1.74	1.16	0.31	0.14
La	ppm	3.47	2.3	5.6	14.75	0.851	8.9	23.1	3.79	14.05	0.8	<0.5
Li	ppm	58.4	2	14.3	54.3	5.6	11.7	34.1	24.1	15.5	85.8	1.1
Mg	%	0.26	0.06	0.83	2.58	0.02	0.08	4.41	0.07	0.47	0.02	0.01
Mn	ppm	96	54	216	1240	71.2	87.1	761	67.7	956	49	53
Mo	ppm	0.76	4.98	3.08	1.19	2.5	0.69	0.92	0.88	0.78	1.17	1.47
Na	%	0.383	0.04	0.37	0.407	0.209	2.15	0.946	2.72	0.214	0.38	0.06
Nb	ppm	4.78	2	2.4	6.36	0.577	4.31	8.2	5.33	4.23	0.4	3
Ni	ppm	12.3	4	28.5	121	2.3	1.13	275	1.78	4.18	1.8	1.9
P	%	0.01	0.002	0.019	0.054	0.001	0.015	0.104	0.003	0.012	0.003	0.001
Pb	ppm	219	6.6	5.4	7.11	3.63	20.2	11.4	11.4	4.72	29.5	1.2
Rb	ppm	14.35	18.7	17.9	28.3	6.24	42.6	131.5	82.5	65.4	11	8.4
Re	ppm	<0.002	<0.002	0.002	<0.002	<0.002	<0.002	<0.002	<0.002	<0.002	<0.002	<0.002
S	%	0.03	0.01	0.33	<0.01	0.13	<0.01	0.28	<0.01	<0.01	0.01	<0.01
Sb	ppm	1.23	0.21	0.19	0.64	0.63	0.48	0.34	0.24	0.29	0.52	0.06
Sc	ppm	1.29	0.6	3.7	9.63	0.17	0.67	18.15	2.1	3.33	0.2	0.3
Se	ppm	<0.2	<1	<1	<0.2	<0.2	<0.2	<0.2	<0.2	<0.2	<1	<1
Sn	ppm	0.63	0.7	0.8	0.78	0.11	0.38	0.91	1.12	1.48	0.2	0.3
Sr	ppm	27.8	12.4	163	500	26	167.5	585	306	440	27.1	5.7
Ta	ppm	0.25	0.14	0.13	0.51	0.04	0.32	0.43	0.47	0.3	<0.05	0.32
Te	ppm	0.54	<0.05	<0.05	0.06	<0.04	0.33	0.05	<0.04	<0.04	<0.05	<0.05
Th	ppm	0.767	1.12	1.34	3.58	0.203	5.16	1.62	50.2	4.57	1.3	0.19
Ti	%	0.051	0.02	0.104	0.188	0.005	0.036	0.44	0.019	0.08	0.005	0.006
Tl	ppm	0.111	0.09	0.07	0.236	0.065	0.276	1.145	0.456	0.278	0.08	0.03
U	ppm	0.62	0.3	0.6	1.4	0.34	0.4	0.53	8.67	1.04	0.2	0.1
V	ppm	11.9	8	33	71.5	1.5	5.1	121.5	1.9	15.3	2	1
W	ppm	1.465	1.4	2.3	2.68	0.167	1.005	0.125	0.505	4.96	0.2	0.1
Y	ppm	1.8	0.6	3	15.75	0.54	2.44	12.2	9.1	10.6	0.4	0.5
Zn	ppm	131.5	15	32	87.1	35.5	32.8	71.4	4.6	15.2	7	2
Zr	ppm	10.2	1.3	10.8	19.3	0.4	1	40.4	8.4	1.2	0.5	<0.5
Y	ppm	17	11.9	17.6	9.55	2.4	1.7	2.6	2.9	15.1	1.3	16
Zn	ppm	68	17	591	28.6	5	17	134	11	80	42	33
Zr	ppm	1.8	3	8.4	1.8	0.7	2	0.7	0.8	1.1	<0.5	1.4

Appendix A-2: Whole-rock geochemical data

Sample		71301	61902	Rhy1	721DW2	61507	62505	71004	624BR5	710DW2	722DW1	Brody
ALS name		MR17-8	MR17-5	MR17-20	MR15-7	MR17-4	MR17-7	MR17-22	MR15-1	MR17-15	MR15-8	MR17-19
Sample		21101	61501	61909	71303	71316	71705	629BR-1	630DW-1	630DW3	CPB	21102
ALS name		MR17-1	MR17-3	MR17-6	MR17-9	MR17-11	MR17-12	MR15-2	MR15-3	MR15-18	MR15-15	MR17-2
Lithology		Leucogranite	Leucogranite	Leucogranite	Leucogranite	Leucogranite	Leucogranite	Leucogranite	Leucogranite	Leucogranite	Leucogranite	Miocene dbs
Altered?		No	Yes	Yes	No	Yes	Yes	Yes	No	No	No	No
Easting		437851	436529	439165	437797	437946	436403	437157	437992	437969	-	437851
Northing		4183463	4183365	4183004	4183561	4183624	4183200	4182454	4183621	4183609	-	4183463
Au	ppm	0.00	0.00	0.00	0.01	0.00	0.03	0.00	0.00	0.07	0.00	0.00
SiO2	%	94.34	78.66	76.34	71.59	63.35	66.29	74.50	74.95	82.47	72.51	49.36
Al2O3	%	2.95	11.85	13.72	15.47	19.01	16.84	14.03	14.00	9.91	15.58	16.87
FeO	%	0.46	0.71	0.70	1.67	1.82	1.10	1.13	0.80	0.46	0.57	8.87
CaO	%	0.19	0.48	1.42	1.96	3.76	6.55	1.73	0.99	1.91	1.26	9.10
MgO	%	0.02	0.11	0.17	0.30	0.45	0.39	0.18	0.13	0.12	0.06	8.27
Na2O	%	0.71	3.00	4.26	3.36	4.06	3.38	3.41	2.72	2.80	2.92	3.20
K2O	%	1.28	4.87	3.24	5.11	5.97	5.11	4.64	6.14	1.91	6.72	1.93
Cr2O3	%	0.01	0.00	0.00	0.01	0.01	0.01	0.06	0.04	0.06	0.03	0.04
TiO2	%	0.00	0.03	0.05	0.14	0.21	0.09	0.10	0.05	0.00	0.02	1.29
MnO	%	0.01	0.01	0.03	0.02	0.04	0.03	0.03	0.02	0.01	0.10	0.15
P2O5	%	0.01	0.21	0.01	0.26	1.08	0.01	0.03	0.03	0.28	0.02	0.61
SrO	%	0.01	0.03	0.03	0.05	0.08	0.05	0.05	0.04	0.04	0.06	0.16
BaO	%	0.00	0.05	0.02	0.06	0.16	0.15	0.11	0.10	0.02	0.16	0.14
LOI		0.15	0.38	1.30	1.75	2.85	6.12	1.32	0.91	1.25	1.21	6.32
Total-recalc		100.00	100.00	100.00	100.00	100.00	100.00	100.00	100.00	100.00	100.00	100.00
C	%	0.08	0.05	0.21	0.24	0.42	1.31	0.25	0.16	0.18	0.22	1.04
S	%	0.005	0.005	0.005	0.12	0.12	0.005	0.01	0.01	0.02	0.01	0.19
Ba	ppm	32.8	382	178	521	1325	1225	956	849	206	1390	1110
Ce	ppm	0.25	32	10.3	19.9	95.2	10.9	19.4	11.1	12.5	4	94.8
Cr	ppm	60	10	10	20	10	10	480	290	440	190	300
Cs	ppm	0.44	2.12	2.06	3.37	2.36	1.47	1.38	2.74	1.21	1.95	7.51
Dy	ppm	0.09	4.26	1.19	4.15	11.2	1.01	0.98	0.77	2.57	2.33	4.32
Er	ppm	0.05	1.59	0.63	1.93	4.24	0.54	0.68	0.33	1.21	2.99	2.36
Eu	ppm	0.015	0.28	0.23	0.47	1.27	0.18	0.42	0.51	0.47	0.49	1.83
Ga	ppm	3	13.8	20.4	21.8	24.5	23.5	20.3	16.7	12.3	18.1	18.5
Gd	ppm	0.08	4.35	1.09	3.93	12.95	1.01	1.27	1.09	3.26	0.84	5.58
Ge	ppm	2.5	2.5	2.5	2.5	2.5	2.5	2.5	2.5	2.5	2.5	2.5
Hf	ppm	0.1	2.6	2.2	2.5	0.7	0.2	2.9	0.6	0.7	1.1	5.4
Ho	ppm	0.01	0.68	0.21	0.77	1.83	0.19	0.21	0.12	0.46	0.68	0.84
La	ppm	0.25	16	5.5	9.9	47.1	6	11.2	6.3	6.1	2.4	46.1
Lu	ppm	0.005	0.12	0.08	0.16	0.3	0.05	0.09	0.04	0.09	0.56	0.31
Nb	ppm	0.7	8.5	13.7	18.1	14.8	12.5	12	8.7	1.5	3.7	17
Nd	ppm	0.1	13.8	4	9.9	44.9	4.6	7.8	4.3	6.8	1.6	43
Pr	ppm	0.05	3.77	1.21	2.5	11.6	1.3	2.17	1.27	1.61	0.5	11.3
Rb	ppm	55	164	147	224	208	136	162	233	63.2	232	82.4
Sm	ppm	0.05	4.02	1.08	3.13	11.7	1.06	1.54	1.15	2.35	0.51	7.26
Sn	ppm	0.5	1	1	3	3	2	1	2	1	1	1
Sr	ppm	38.8	239	249	386	656	415	459	357	375	491	1240
Ta	ppm	0.05	1	1	4.3	1.2	1.4	0.7	0.9	0.1	0.3	0.8
Tb	ppm	0.01	0.77	0.2	0.71	2.04	0.15	0.18	0.13	0.48	0.21	0.79
Th	ppm	0.1	13.15	8.38	6.94	19.05	3.34	6.13	3.08	2.79	1.63	5.44
Tm	ppm	0.005	0.19	0.1	0.25	0.46	0.07	0.09	0.06	0.11	0.49	0.3
U	ppm	0.19	2.78	1.66	7.07	4.2	0.71	47.1	4.08	6.02	13.65	1.22
V	ppm	2.5	2.5	2.5	9	12	14	9	2.5	6	2.5	176
W	ppm	1	1	1	2	6	4	1	1	1	1	1
Y	ppm	0.25	20.2	6.8	22.7	50.5	5.6	5	3.6	12.9	19	22.2
Yb	ppm	0.03	1.09	0.59	1.4	2.4	0.46	0.56	0.17	0.59	3.5	2.01
Zr	ppm	1	54	49	52	20	6	94	16	20	33	245
As	ppm	0.5	2.1	0.5	1.1	1.2	20.6	1.5	0.05	0.1	0.5	0.6
Bi	ppm	0.02	0.13	0.1	0.09	0.33	0.02	0.03	0.03	0.04	0.03	0.01
Hg	ppm	0.0025	0.012	0.019	0.007	0.005	0.064	0.006	0.015	0.013	0.0025	0.006
In	ppm	0.0025	0.0025	0.0025	0.006	0.009	0.0025	0.0025	0.0025	0.0025	0.0025	0.022
Re	ppm	0.0005	0.0005	0.0005	0.0005	0.0005	0.0005	0.0005	0.001	0.0005	0.0005	0.0005
Sb	ppm	0.27	0.14	0.1	0.21	0.16	1.76	0.2	1.3	0.025	0.025	0.14
Se	ppm	0.1	0.1	0.1	0.1	0.4	0.1	0.3	0.2	0.6	0.1	0.1
Te	ppm	0.005	0.005	0.005	0.005	0.01	0.01	0.005	0.005	0.005	0.005	0.01
Tl	ppm	0.02	0.05	0.05	0.07	0.07	0.14	0.05	0.03	0.02	0.03	0.6
Ag	ppm	0.25	0.25	0.25	0.25	0.25	0.25	0.25	0.25	0.25	0.25	0.25
Cd	ppm	0.25	0.25	0.25	0.25	0.25	0.25	0.25	0.25	0.25	0.25	0.25
Co	ppm	0.5	1	1	0.5	1	1	0.5	1	0.5	0.5	29
Cu	ppm	4	5	12	7	8	5	4	2	3	1	29
Li	ppm	5	5	5	5	10	5	5	5	5	5	20
Mo	ppm	3	1	2	1	1	1	8	6	15	4	1
Ni	ppm	1	2	6	1	0.5	2	4	3	4	1	147
Pb	ppm	14	19	28	31	49	12	24	39	12	33	12
Sc	ppm	0.5	1	2	2	2	1	2	1	0.5	1	15
Zn	ppm	19	9	17	30	56	18	38	22	8	8	101
Li	ppm	10	10	10	30	10	5	10	10	5	10	10
Mo	ppm	1	1	1	4	1	1	0.5	6	1	5	1
Ni	ppm	20	1	0.5	37	1	0.5	2	6	2	2	2
Pb	ppm	15	20	25	10	15	20	22	20	56	18	23
Sc	ppm	7	5	5	12	1	1	1	2	1	2	2
Zn	ppm	61	60	60	82	63	38	49	75	34	55	82

Sample		71313	71314	71501	71706	630MP2	702BR1	715DW1	716DW1	722DW2	728BR1	728DW1
ALS name		MR17-10	MR17-24	MR17-23	MR17-13	MR15-4	MR15-5	MR17-16	MR17-17	MR15-9	MR15-10	MR15-12
Lithology		Pre-Tertiary dbs	Pre-Tertiary dbs	Pre-Tertiary dbs	Pre-Tertiary dbs	Miocene dbs	Diabase	Miocene dbs	Diabase	Miocene dbs	Diabase	Diabase
Altered?		Yes	No	No	No	No	Yes	Yes	Yes	No	Yes	Yes
Easting		437993	437993	437156	436395	438357	437217	437971	437740	437992	437839	437987
Northing		4183618	4183618	4183845	4183124	4183477	4182380	4183657	4183705	4183439	4183595	4183616
Au	ppm	0.02	0.00	0.00	0.00	0.00	0.01	0.01	0.10	0.00	0.03	0.01
SiO2	%	47.73	50.90	50.00	49.41	49.06	59.52	46.49	63.11	50.54	58.97	63.83
Al2O3	%	15.26	16.48	17.07	16.89	15.41	18.92	15.44	7.69	17.67	19.75	18.46
FeO	%	8.90	9.70	10.61	11.42	8.45	7.82	9.46	7.06	8.34	5.12	3.93
CaO	%	12.30	10.57	8.13	10.44	10.59	1.10	11.40	9.14		3.77	1.90
MgO	%	10.09	6.87	7.20	6.08	10.04	8.37	12.71	9.87	7.08	2.53	6.41
Na2O	%	1.89	2.86	3.23	3.00	2.38	0.04	0.36	0.83	3.48	3.65	0.06
K2O	%	1.92	1.07	1.58	0.92	1.92	1.66	2.15	1.08	2.02	3.56	3.04
Cr2O3	%	0.10	0.06	0.02	0.01	0.09	0.09	0.16	0.09	0.04	0.04	0.09
TiO2	%	1.21	1.02	1.60	1.33	1.01	1.38	1.21	0.63	1.35	1.36	1.55
MnO	%	0.12	0.17	0.16	0.18	0.15	0.14	0.15	0.14	0.14	0.10	0.05
P2O5	%	0.36	0.18	0.26	0.20	0.49	0.91	0.35	0.24	0.63	0.85	0.55
SrO	%	0.07	0.06	0.07	0.06	0.16	0.01	0.07	0.06	0.17	0.12	0.01
BaO	%	0.06	0.05	0.07	0.05	0.24	0.03	0.05	0.07	0.18	0.18	0.13
LOI		10.60	1.53	2.86	2.91	6.62	9.94	13.20	7.88	2.86	5.51	12.45
Total-recalc		100.00	100.00	100.00	100.00	100.00	100.00	100.00	100.00	100.00	100.00	100.00
C	%	1.65	0.19	0.2	0.44	1.12	0.01	2.06	1.46	0.4	0.04	0.02
S	%	0.7	0.3	0.005	0.51	0.12	0.81	0.4	0.26	0.19	0.01	0.63
Ba	ppm	418	437	586	421	1910	320	344	525	1470	1490	977
Ce	ppm	43.7	40.1	40	40.4	83.1	119.5	40.4	70.9	91.6	118.5	52.3
Cr	ppm	670	410	110	80	640	670	950	560	320	330	600
Cs	ppm	7.3	0.7	3.35	1.72	3.26	2.48	3.93	8.99	6.95	1.84	2.45
Dy	ppm	3.36	3.79	3.9	4.44	3.94	5.48	3.16	2.7	4.49	5.02	1.9
Er	ppm	1.82	2.25	2.03	2.56	2	3.4	1.67	1.27	2.46	2.58	1.18
Eu	ppm	1.23	1.24	1.47	1.31	1.88	2.37	1.13	0.95	1.94	2.87	1.15
Ga	ppm	16.3	18.4	18.1	18.7	16.6	26.5	14.9	9.9	19.6	21.1	22.4
Gd	ppm	3.98	4.07	4.76	4.6	6.01	8.16	3.79	3.79	5.78	8.19	3.33
Ge	ppm	2.5	2.5	2.5	2.5	2.5	2.5	2.5	2.5	2.5	2.5	2.5
Hf	ppm	3	3.1	3.3	2.9	3.7	6.9	2.8	3.2	5.6	6.6	4.4
Ho	ppm	0.63	0.8	0.74	0.9	0.71	1.09	0.58	0.48	0.85	0.96	0.38
La	ppm	20.3	19.5	18.5	19.9	42.2	58	19	34.6	47.5	63.2	24
Lu	ppm	0.24	0.36	0.25	0.35	0.25	0.48	0.22	0.14	0.3	0.34	0.16
Nb	ppm	9.3	5.4	5.9	4.7	7.4	21.2	8.5	8.2	17.9	20.5	12.3
Nd	ppm	23.2	19.7	22.8	20.7	40.6	58.1	21.8	30.6	42.5	57	25.9
Pr	ppm	5.7	4.88	5.29	5.07	10.55	15.2	5.19	8.28	11.25	15.3	6.71
Rb	ppm	101	28	40	22.4	58	64.8	85.7	92.2	64.9	98.1	107.5
Sm	ppm	4.56	4.01	4.93	4.45	7.11	9.72	4.25	5.32	7.77	9.36	4.72
Sn	ppm	1	1	1	1	1	2	1	1	1	2	1
Sr	ppm	539	542	577	487	1215	65.4	487	445	1320	910	110
Ta	ppm	0.5	0.3	0.2	0.2	0.3	0.9	0.3	0.3	0.8	1	0.6
Tb	ppm	0.55	0.61	0.68	0.72	0.74	1.05	0.51	0.51	0.81	0.98	0.41
Th	ppm	2.84	3.39	2.96	4.94	7.98	5.67	3.04	7.66	5.29	5.46	3.48
Tm	ppm	0.26	0.34	0.28	0.37	0.26	0.46	0.23	0.16	0.32	0.34	0.16
U	ppm	4.81	0.99	0.95	1.18	2.26	2.09	2.48	1.16	1.21	2.13	1.58
V	ppm	223	272	283	322	225	209	208	94	178	190	221
W	ppm	1	0.5	1	1	1	3	1	1	0.5	3	4
Y	ppm	17.2	22.3	20	24.1	19.4	29	15.4	12.7	22.1	25.3	9.2
Yb	ppm	1.62	2.25	1.74	2.4	1.69	3.16	1.44	0.97	1.95	2.19	1.06
Zr	ppm	115	115	124	116	145	318	112	125	261	309	186
As	ppm	3.3	0.5	0.8	1.4	0.7	4.4	1.3	1	1.3	28.9	17.4
Bi	ppm	0.15	0.02	0.02	0.06	0.02	0.05	0.02	0.06	0.02	0.14	0.04
Hg	ppm	0.0025	0.0025	0.025	0.005	0.0025	0.305	0.006	0.0025	0.014	0.275	0.317
In	ppm	0.041	0.015	0.022	0.026	0.017	0.038	0.039	0.014	0.026	0.045	0.04
Re	ppm	0.0005	0.0005	0.0005	0.001	0.0005	0.003	0.0005	0.0005	0.0005	0.0005	0.0005
Sb	ppm	0.31	0.07	0.09	0.16	0.09	0.2	0.15	0.15	0.09	0.51	0.91
Se	ppm	0.5	0.2	0.2	0.4	0.6	0.5	0.1	0.3	0.6	1	0.4
Te	ppm	0.02	0.01	0.01	0.03	0.005	0.005	0.03	0.03	0.01	0.005	0.01
Tl	ppm	0.67	0.03	0.02	0.04	0.1	0.19	0.33	0.83	0.22	0.07	1.1
Ag	ppm	0.25	0.25	0.25	0.5	0.25	0.25	0.25	0.25	0.25	0.25	0.25
Cd	ppm	0.7	0.25	0.25	0.25	0.25	0.25	0.25	0.25	0.25	0.25	0.25
Co	ppm	33	38	35	44	38	37	41	37	29	18	42
Cu	ppm	76	34	29	26	33	26	23	54	35	35	36
Li	ppm	60	10	10	10	30	50	50	20	20	20	40
Mo	ppm	0.5	0.5	1	0.5	0.5	4	0.5	1	2	4	1
Ni	ppm	125	49	33	20	164	185	170	362	104	35	175
Pb	ppm	12	3	6	4	9	13	11	5	11	12	1
Sc	ppm	22	27	23	29	22	18	23	15	15	17	23
Zn	ppm	160	88	97	94	87	241	91	82	99	64	105

Sample		bluelite	Bluelite Qtz	DPA	DWD	707BR3	715DW2	728BR2	728DW3	728DW4
ALS name		MR17-21	MR17-18	MR15-17	MR15-16	MR15-6	MR17-14	MR15-11	MR15-13	MR15-14
Lithology		Diabase	Diabase	Miocene dbs	Diabase	Wyman	Wyman	Wyman	Wyman	Wyman
Altered?		No	Yes	No	No	No	Yes	No	No	No
Easting		436408	436408	-	437717	437117	436659	437839	437987	437987
Northing		4183168	4183168	-	4183650	4182420	4183140	4183595	4183616	4183616
Au	ppm	0.02	0.00	0.00	0.00	0.02	0.03	0.01	0.03	1.21
SiO2	%	64.87	69.96	52.53	50.20	57.37	54.64	62.97	41.49	71.76
Al2O3	%	17.79	17.39	16.13	13.84	13.35	9.73	18.98	6.77	9.59
FeO	%	4.30	5.03	8.37	9.79	3.52	1.50	5.75	2.01	1.97
CaO	%	2.24	0.23	8.74	7.99	19.01	27.76	3.10	45.58	10.10
MgO	%	5.77	1.03	7.40	12.60	1.45	0.58	2.27	1.05	0.52
Na2O	%	0.08	0.09	2.93	1.98	1.84	1.14	0.11	0.03	1.13
K2O	%	2.82	5.30	1.57	0.98	2.79	4.13	5.83	2.25	4.37
Cr2O3	%	0.07	0.01	0.06	0.10	0.02	0.01	0.02	0.03	0.04
TiO2	%	1.42	0.71	1.40	1.27	0.33	0.18	0.74	0.22	0.17
MnO	%	0.05	0.08	0.12	0.16	0.07	0.15	0.07	0.12	0.08
P2O5	%	0.50	0.07	0.55	0.47	0.09	0.06	0.07	0.12	0.09
SrO	%	0.01	0.01	0.10	0.11	0.10	0.05	0.01	0.30	0.09
BaO	%	0.10	0.08	0.09	0.50	0.06	0.09	0.09	0.03	0.09
LOI		11.00	3.78	9.02	4.17	12.20	18.65	6.37	26.90	7.82
Total-recalc		100.00	100.00	100.00	100.00	100.00	100.00	100.00	100.00	100.00
C	%	0.11	0.06	1.53	0.33	3.08	4.97	0.79	7.2	2.18
S	%	1.08	0.01	0.005	0.12	0.41	0.005	0.01	0.14	0.49
Ba	ppm	759	674	687	4150	405	577	695	174.5	664
Ce	ppm	56.2	97	73.7	72.6	47.5	24.8	106.5	23.2	23.3
Cr	ppm	450	90	360	660	190	20	190	140	270
Cs	ppm	12.9	2.45	2.17	4.02	2.51	1.43	3.38	0.74	1.23
Dy	ppm	2.17	4.73	4.5	3.47	2.76	2.68	5.85	2.45	1.87
Er	ppm	1.13	2.24	2.25	1.74	1.7	1.35	3.52	1.37	1.12
Eu	ppm	1.17	1.38	1.81	1.69	0.75	0.77	1.53	1.01	0.65
Ga	ppm	21.1	21	17.2	15.6	17	11.3	24.3	11.2	15.7
Gd	ppm	3.34	5.58	5.92	5.11	3.39	2.38	6.97	2.7	2.3
Ge	ppm	2.5	2.5	2.5	2.5	2.5	2.5	2.5	2.5	2.5
Hf	ppm	3.9	7.4	5.4	4.6	2.4	1.8	5.1	1.9	1.8
Ho	ppm	0.39	0.81	0.83	0.63	0.51	0.49	1.14	0.49	0.38
La	ppm	26	47.2	35.8	37.3	26	13.3	56.4	12.2	12.4
Lu	ppm	0.17	0.26	0.27	0.22	0.19	0.19	0.45	0.16	0.14
Nb	ppm	12.3	18.2	15	11.4	15.1	9.6	18.7	5.8	10.7
Nd	ppm	27.3	39.7	37.9	34.9	20.4	11	46	10.8	10.3
Pr	ppm	6.88	10.95	9.35	8.98	5.74	2.96	12.65	2.89	2.89
Rb	ppm	116	232	59.1	35.5	105.5	111	276	62.9	109
Sm	ppm	4.83	7	6.99	6.24	3.72	2.32	7.99	2.49	2.4
Sn	ppm	1	4	2	2	3	1	3	2	3
Sr	ppm	111.5	40.4	739	789	752	334	83.7	1845	667
Ta	ppm	0.5	1.2	0.6	0.6	1.2	1.1	1.2	0.4	0.7
Tb	ppm	0.4	0.83	0.78	0.63	0.48	0.42	1.03	0.42	0.34
Th	ppm	3.38	16.5	3.56	4.47	8.35	4.59	17.15	3.74	4.12
Tm	ppm	0.14	0.28	0.3	0.23	0.22	0.19	0.48	0.19	0.15
U	ppm	1.66	18.9	1.01	1.02	6.91	1.91	4.1	4.25	6.32
V	ppm	206	78	206	164	35	19	80	25	25
W	ppm	5	3	0.5	0.5	2	6	6	4	6
Y	ppm	9.8	20.4	21.1	17.5	15.3	15.7	31.6	14.5	10.6
Yb	ppm	1.02	1.82	1.9	1.43	1.53	1.34	3.26	1.12	1.02
Zr	ppm	164	274	241	198	85	67	199	75	63
As	ppm	28.4	27.5	0.5	0.3	9.9	7.6	32.7	30.3	5.4
Bi	ppm	0.05	1.28	0.01	0.03	2.75	0.29	0.09	0.12	0.57
Hg	ppm	0.929	0.661	0.009	0.0025	0.019	0.191	0.037	0.014	0.009
In	ppm	0.047	0.027	0.028	0.017	0.017	0.056	0.009	0.034	0.026
Re	ppm	0.0005	0.0005	0.0005	0.0005	0.0005	0.0005	0.0005	0.001	0.0005
Sb	ppm	2.88	5.04	0.06	0.07	0.66	0.7	0.39	0.52	0.3
Se	ppm	0.2	0.2	0.5	0.4	0.5	0.3	0.5	1	0.6
Te	ppm	0.02	0.02	0.005	0.01	0.02	0.03	0.01	0.02	0.03
Tl	ppm	1.38	1.21	0.17	0.02	0.4	0.08	0.12	0.08	0.13
Ag	ppm	0.25	0.25	0.25	0.25	0.25	0.8	0.25	0.25	0.25
Cd	ppm	0.25	0.25	0.25	0.25	0.25	3.4	0.25	0.25	0.25
Co	ppm	36	33	28	51	6	1	13	2	3
Cu	ppm	43	40	7	27	16	5	24	3	11
Li	ppm	40	30	50	30	20	10	40	10	10
Mo	ppm	0.5	3	0.5	2	3	1	2	2	6
Ni	ppm	168	68	117	381	19	5	39	6	8
Pb	ppm	5	7	14	4	11	266	44	26	27
Sc	ppm	19	11	21	14	7	3	14	4	3
Zn	ppm	95	96	97	111	118	274	85	29	13

Appendix B-1: U-Pb zircon geochronometry

Sample 624BR5 (Two-mica granite)

Spot 624br5 (Granite)	238U 206Pb	1 sigma % error	207Pb 206Pb	1 sigma % error	206/238 age	1 sigma abs err	207/206 age	1 sigma abs err
3b	63.0131	0.01	0.0494	0.01	101.5	0.8	168.2	30.2
3m	5.8143	0.01	0.0747	0.01	1023.1	5.9	1062.8	20.9
3t	67.3715	0.01	0.0480	0.01	95.0	0.6	111.0	26.8
b1	65.8169	0.01	0.0559	0.02	97.2	0.8	523.1	47.8
2b	46.0948	0.01	0.0503	0.02	138.4	1.1	224.4	35.4
2t	38.2172	0.01	0.0505	0.01	166.5	1.1	220.0	32.5
10r	72.9311	0.01	0.0489	0.01	87.8	0.8	191.7	33.8
12c	70.3341	0.01	0.0465	0.03	91.0	1.0	118.0	70.2
12r	70.7921	0.01	0.0479	0.01	90.4	0.6	101.3	21.5
b10	17.9528	0.01	0.0808	0.01	349.4	2.4	1222.1	18.4
5r	71.6298	0.01	0.0479	0.01	89.4	0.6	95.7	23.6
6m	68.2000	0.01	0.0469	0.01	93.8	0.8	60.3	34.1
6t	70.7958	0.01	0.0485	0.01	90.4	0.6	123.1	21.0
33r	66.2105	0.01	0.0480	0.01	96.6	0.8	100.1	26.1
33c	7.1842	0.01	0.0941	0.01	840.1	6.8	1496.3	12.6
31	71.0910	0.01	0.0458	0.02	90.0	1.0	0.0	37.9
20r	70.6973	0.01	0.0478	0.01	90.5	0.7	91.1	20.6
18r	70.6652	0.01	0.0661	0.02	90.6	1.1	977.7	43.0
18c	35.9380	0.01	0.0512	0.01	176.9	1.5	248.6	26.2
16t	73.9948	0.01	0.0476	0.01	86.5	0.7	76.6	19.4
16b	67.1043	0.01	0.0486	0.01	95.4	0.8	130.4	21.5
13b	69.3649	0.01	0.0502	0.01	92.3	0.9	207.2	28.9
5t	38.3427	0.01	0.0490	0.01	166.0	1.2	157.6	30.7
5m	38.6481	0.01	0.0489	0.02	164.7	1.3	143.3	38.9
5b	37.5732	0.01	0.0584	0.02	169.3	1.3	544.7	36.6
4t	13.4684	0.01	0.0769	0.01	461.7	4.0	1127.8	24.0
4b	5.4360	0.01	0.0810	0.01	1088.6	7.6	1222.1	23.3
2b	4.0379	0.01	0.0917	0.01	1426.4	8.5	1460.4	17.7
1	73.0239	0.01	0.0486	0.01	87.7	0.6	126.3	34.1
12	34.0254	0.01	0.0874	0.01	186.7	2.4	1368.4	17.6
11	18.6190	0.01	0.0659	0.01	337.2	3.4	803.2	24.6
9	71.4479	0.01	0.0482	0.01	89.6	1.0	109.6	28.9
8a	69.1095	0.01	0.0481	0.01	92.6	1.0	105.1	21.9
8b	10.8421	0.01	0.1012	0.01	568.7	6.3	1646.0	14.3
7	71.4552	0.01	0.0451	0.03	89.6	1.2	417.9	66.9
6t	70.3994	0.01	0.0500	0.01	90.9	1.0	194.9	22.0

UTM Coordinates Sample 624BR5 (NAD83 Zone 11N): 437148 4182459

Sample 021101 (Leucogranite pegmatite)
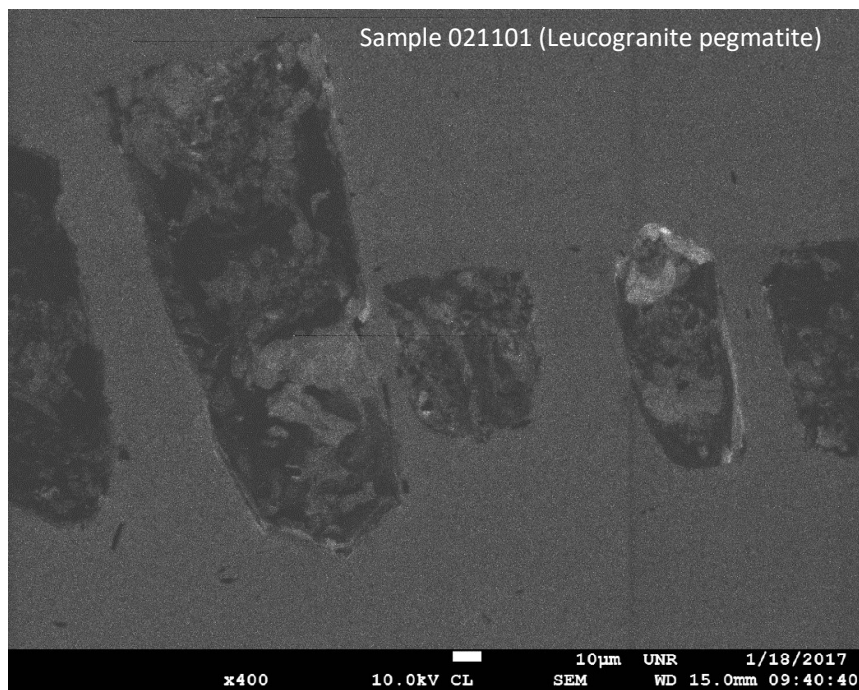
Spot	238U	1 sigma	207Pb	1 sigma	206/238	1 sigma	207/206	1 sigma
21101 (Leucogranite)	206Pb	% error	206Pb	% error	age	abs err	age	abs err
34	48.80	0.0096	0.18	0.0	130.8	1.2	2639.311	39.52951
33	72.42	0.0100	0.05	0.0	88.4	0.9	152.8194	24.37851
32	71.54	0.0095	0.05	0.0	89.5	0.8	167.6292	23.60803
59	68.87	0.0089	0.05	0.0	92.9	0.8	389.383	18.66625
58	72.42	0.0090	0.05	0.0	88.4	0.8	406.4567	17.63423
57	72.41	0.0125	0.09	0.0	88.4	1.1	1493.71	46.09137
56	59.99	0.0151	0.35	0.0	106.6	1.6	3718.306	41.6865
55	76.28	0.0119	0.09	0.0	84.0	1.0	1383.371	65.73004
54	68.89	0.0218	0.05	0.0	92.9	2.0	307.7326	16.8537
53	63.11	0.0146	0.05	0.0	101.3	1.5	167.6665	17.5988
52	65.66	0.0098	0.08	0.0	97.4	0.9	1142.039	51.211
51	75.88	0.0098	0.05	0.0	84.4	0.8	330.2003	18.00547
50	71.65	0.0088	0.05	0.0	89.3	0.8	140.809	14.13093
70	77.51	0.0080	0.05	0.0	82.6	0.7	228.969	16.56627
69	66.05	0.0079	0.12	0.0	96.9	0.8	1891.107	11.78554
68	71.96	0.0089	0.05	0.0	89.0	0.8	283.1572	18.8488
67	65.84	0.0080	0.09	0.0	97.2	0.8	1470.516	31.21912
66	100.08	0.0115	0.07	0.0	64.1	0.7	881.261	28.02109

UTM Coordinates Sample 021101 (NAD83 Zone 11N): 437851 4183

Appendix B-2: ^{40}Ar/^{39}Ar hornblende geochronometry

Claypoole-CREG, 71315, Amphibole, 10.02 mg, J = 0.001749 ± 0.42%
4 amu discrimination = 0.9879 ± 0.08%, 40/39K = 0.0136 ± 12.80%, 36/37Ca = 0.000301 ± 0.80%, 39/37Ca = 0.000831 ± 0.44%

step	T (C)	t (min.)	36Ar	37Ar	38Ar	39Ar	40Ar	%40Ar*	% 39Ar rlsd	Ca/K	40Ar*/39ArK	Age (Ma)	1s.d.
1	900	12	1.867	18.244	0.650	8.991	738.485	25.4	8.3	8.15367781	20.355680	63.11	2.34
2	970	12	0.213	8.868	0.125	2.349	85.681	35.0	2.2	15.2085037	9.915342	31.02	0.38
3	1040	12	0.170	12.223	0.322	5.081	76.571	48.3	4.7	9.67180531	5.372863	16.87	0.22
4	1100	12	0.193	31.744	0.685	11.853	121.377	67.4	10.9	10.7716999	5.755272	18.07	0.22
5	1130	12	0.244	44.478	0.757	15.849	150.435	64.4	14.6	11.2895127	5.297051	16.64	0.16
6	1150	12	0.147	17.659	0.318	6.377	78.496	74.8	5.9	11.1393032	5.904144	18.53	0.26
7	1170	12	0.132	19.199	0.366	6.864	82.302	85.3	6.3	11.2519365	6.733408	21.12	0.38
8	1190	12	0.124	11.381	0.201	4.003	61.948	80.1	3.7	11.4379935	6.762268	21.21	0.23
9	1210	12	0.141	19.306	0.324	6.642	79.372	79.3	6.1	11.6946857	6.111989	19.18	0.40
10	1230	12	0.182	30.416	0.496	10.226	104.604	72.2	9.4	11.9683476	5.401654	16.96	0.16
11	1250	12	0.223	43.648	0.709	14.793	138.760	71.5	13.7	11.8721931	5.350470	16.80	0.21
12	1280	12	0.163	22.170	0.392	7.517	89.111	72.5	6.9	11.8670617	5.878529	18.45	0.27
13	1400	12	0.201	22.531	0.398	7.799	107.390	76.0	7.2	11.6231944	6.321191	19.84	0.35

Cumulative %39Ar rlsd = 100.0   Total gas age = 22.10   0.13
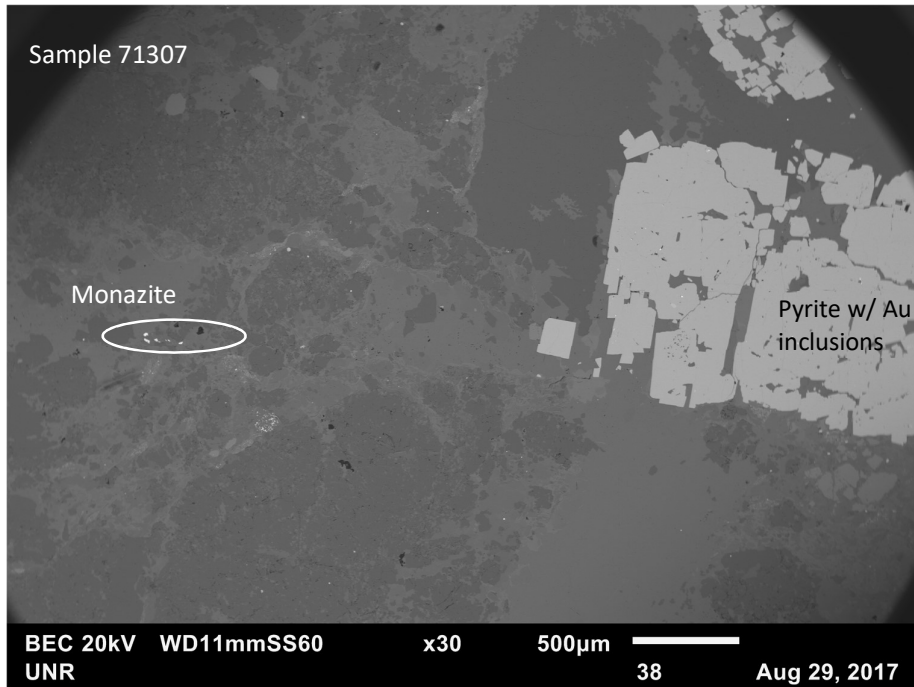
note: isotope beams in mV, rlsd = released, error in age includes J error, all errors 1 sigma   No plateau
(36Ar through 40Ar are measured beam intensities, corrected for decay for the age calculations)   No isochron

UTM Coordinates Sample 71315 (NAD83 Zone 11N): 437993 4183618

Appendix B-3. U-Pb monazite geochronology

Sample 71307

Monazite

Pyrite w/ Au inclusions

BEC 20kV   WD11mmSS60   x30   500µm

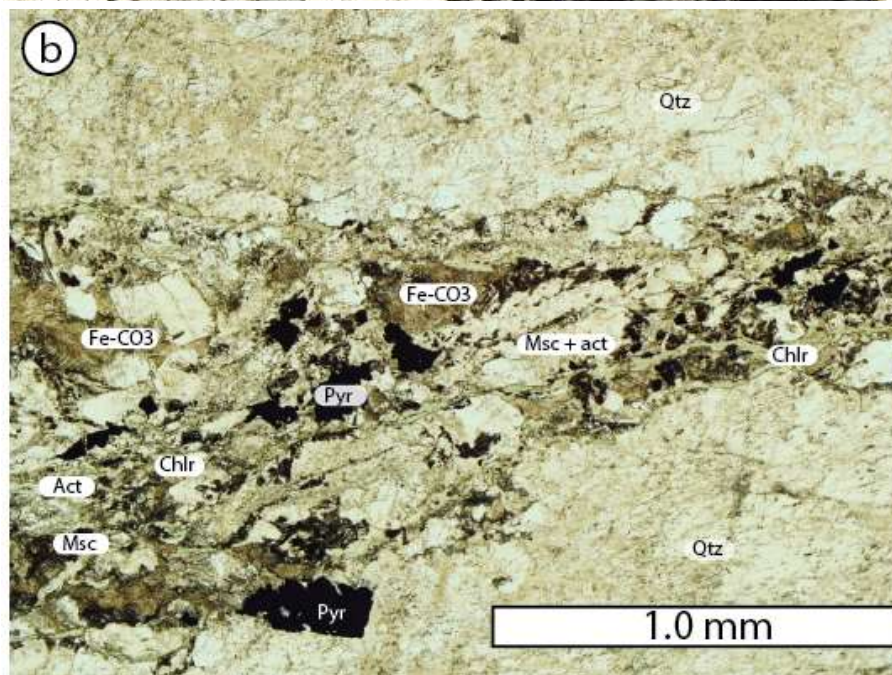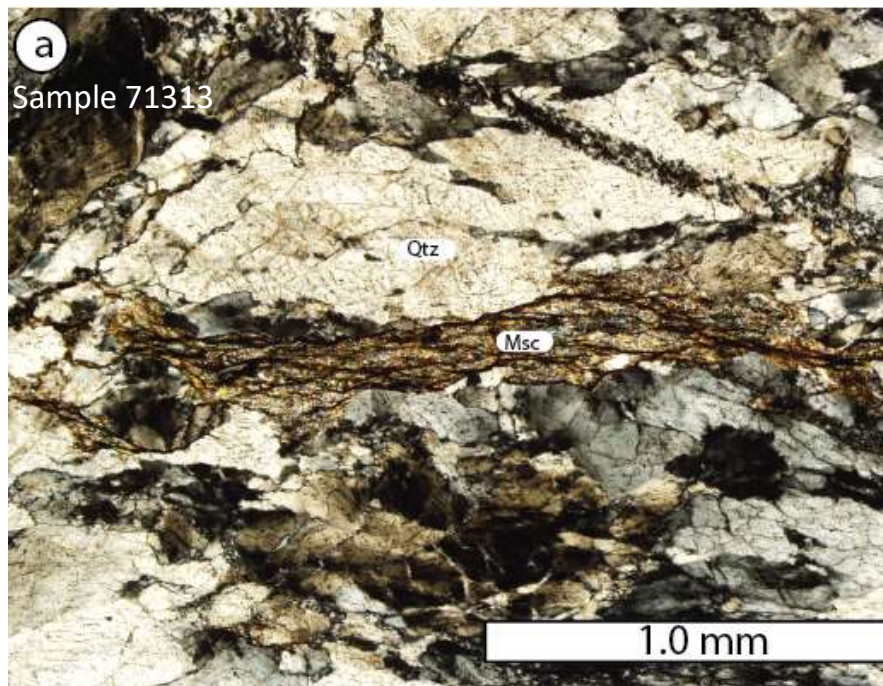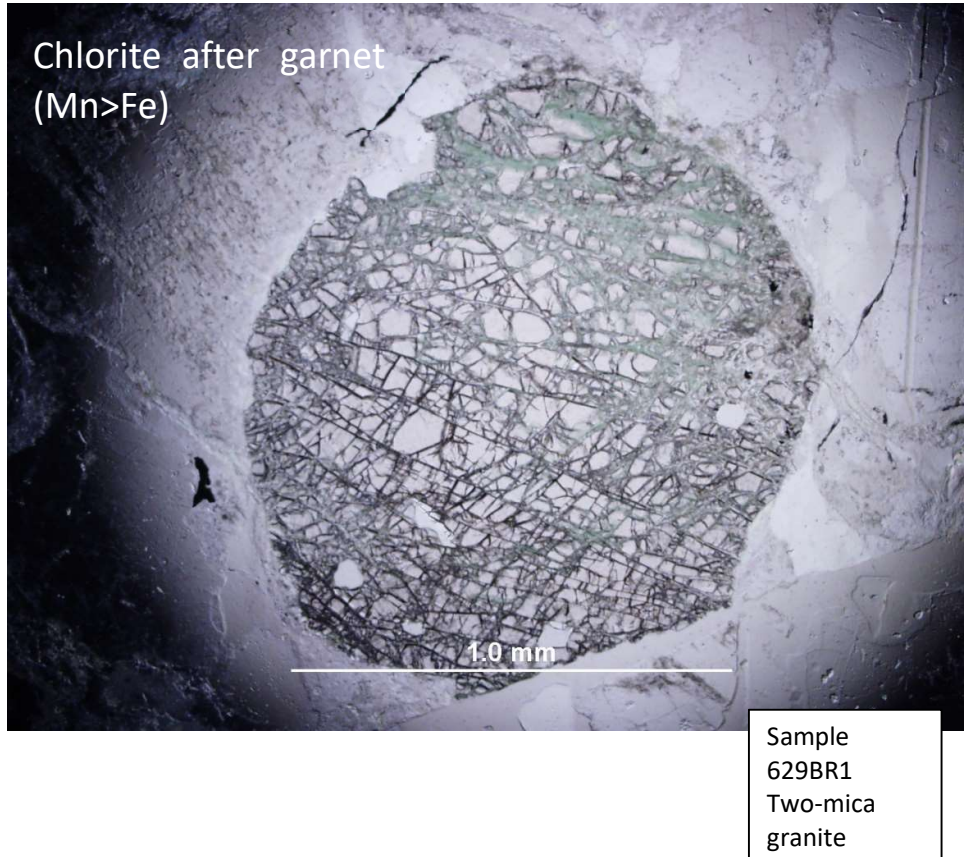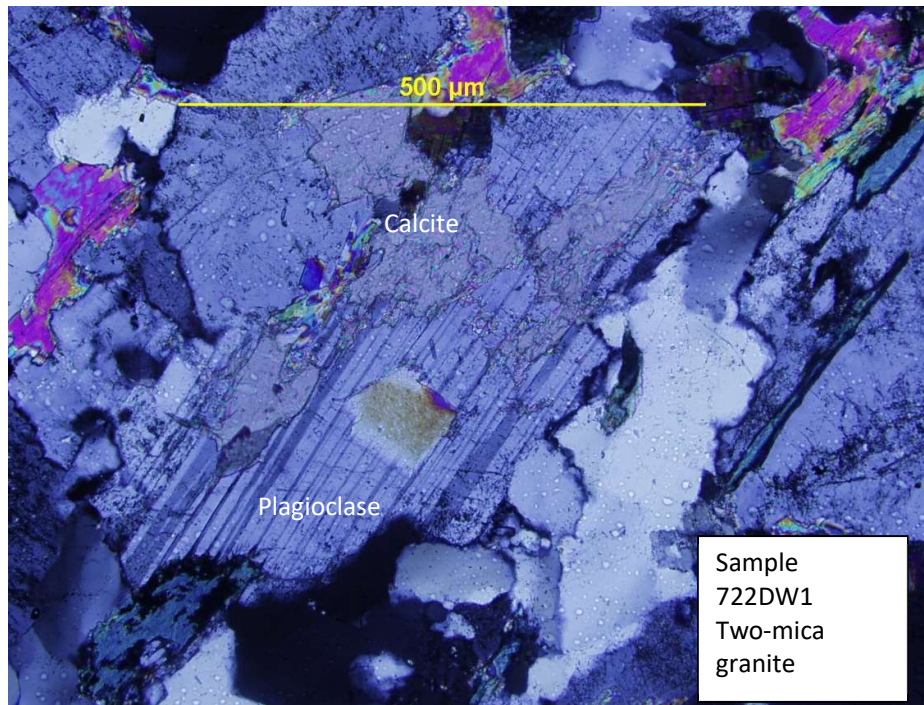UNR   38   Aug 29, 2017
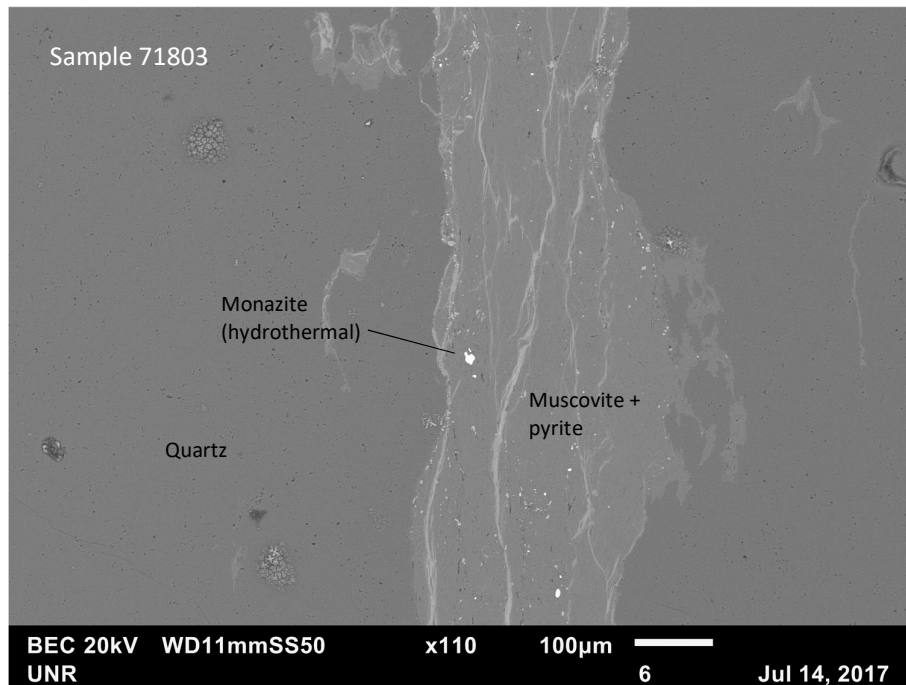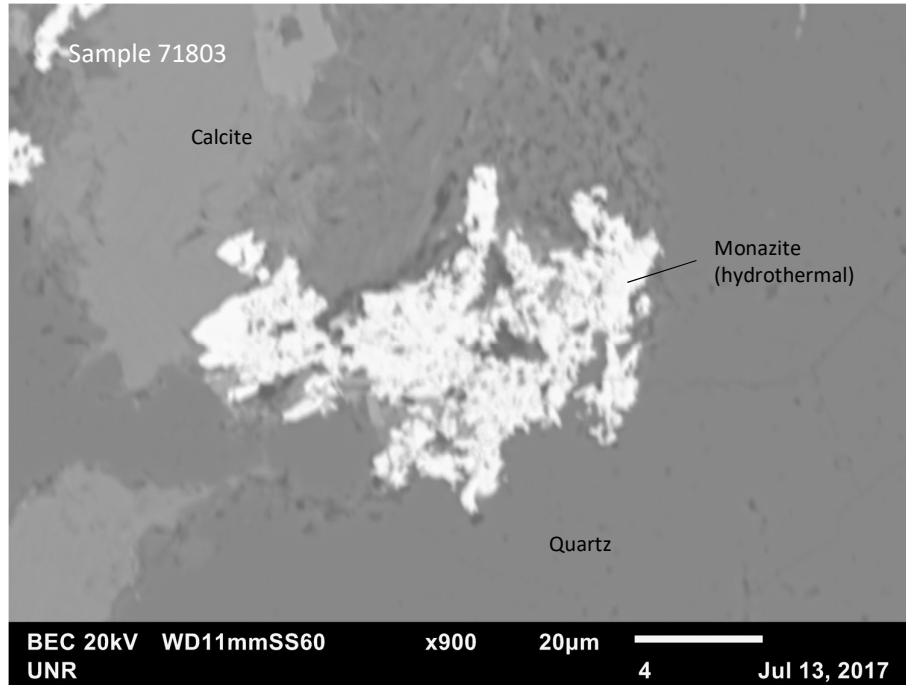
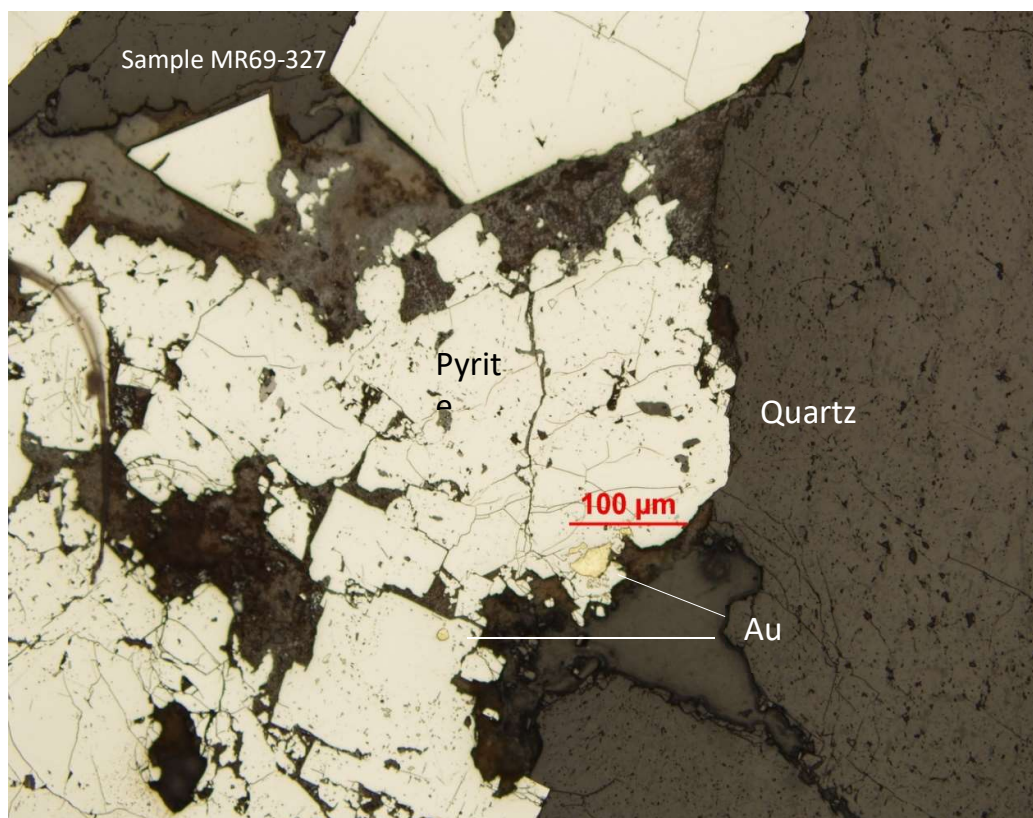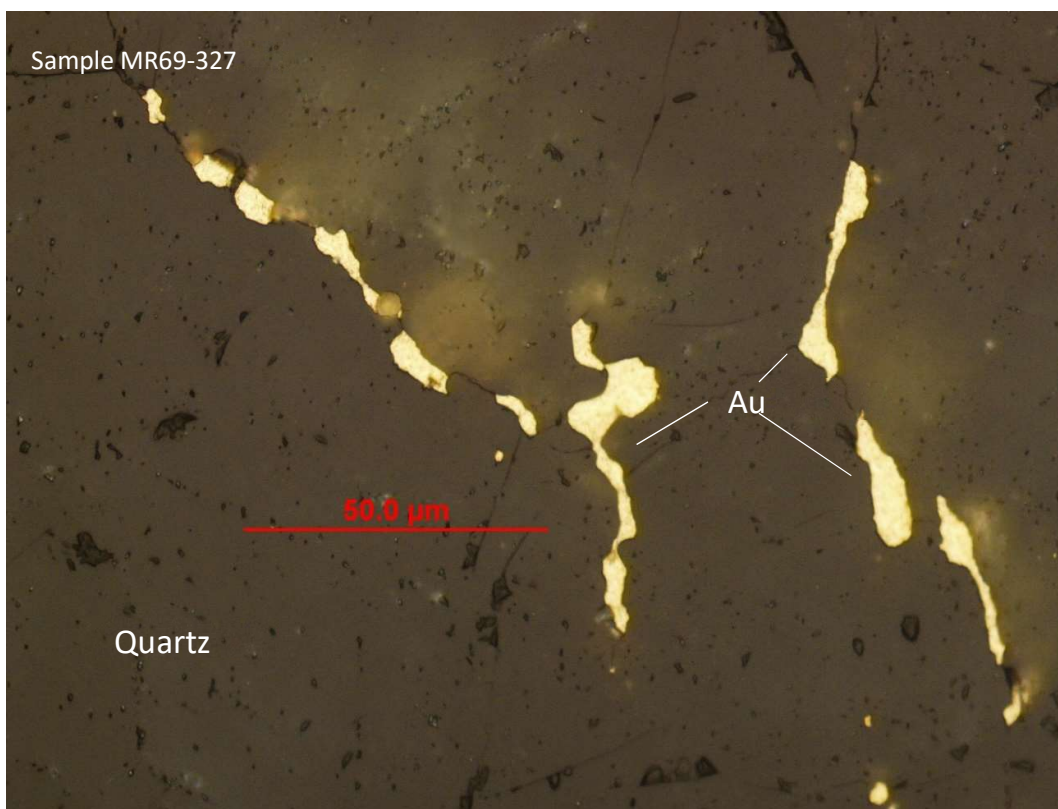**Sample 71317 UTM Coordinates Sample 71317 (NAD83 Zone 11N): 437717 4183650**

Day 1	Final207_235	Final207_235_Int2SE	Final206_238	Final206_238_Int2SE	Final238_206	Final238_206_Int2SE	Final207_206	Final207_206_Int2SE	Final208_232	Final208_232_Int2SE	FinalAge207_235	FinalAge207_235_Int2SE	FinalAge206_238	FinalAge206_238_Int2SE	FinalAge208_232	FinalAge208_232_Int2SE	FinalAge207_206	FinalAge207_206_Int2SE
Output 1_1	12.17	0.38	0.1138	0.0034	8.787346	0.2625393	0.775	0.02	0.751	0.03	2595	29	693	19	11190	340	4904	46
Output 1_2	0.0803	0.0071	0.01186	0.00029	84.31703	2.067715	0.0487	0.0044	0.012	0.0021	81	6.4	76	1.8	240	42	190	160
Output 1_3	23.7	2.6	0.21	0.02	4.761905	0.4535147	0.92	0.11	1.6	2.6	3440	440	1200	100	1.84E+04	1.20E+03	6130	270
Output 1_4	0.447	0.025	0.03053	0.00077	32.75467	0.8261085	0.1078	0.0051	0.066	0.0045	374	18	193.8	4.8	1287	85	1716	88
Output 1_5	0.435	0.052	0.0327	0.0013	30.58104	1.21576	0.097	0.012	0.147	0.034	372	36	207.3	8.2	2400	460	1460	240
Output 1_6	44	13	0.5	13	2	0.62	0.62	0.16	0.67	0.13	3920	340	2490	660	1.01E+04	1.60E+03	4720	430
Output 1_7	32.6	6.7	0.325	0.45	3.076923	0.4733728	0.72	0.1	0.38	0.041	3520	470	1760	290	6390	960	4690	280
Output 1_8	0.48	0.64	0.0046	0.0041	222.2222	202.4694	0.1	0.49	0.34	0.056	710	200	28	26	470	42	-2.66E+04	9.70E+03
Output 1_9	0.199	0.097	0.0046	0.0012	217.3913	56.74078	0.33	0.3	0.0501	0.00061	435	82	29.7	8	101	4	-5.20E+03	4.70E+03
Output 1_10	0.83	0.6	0.0025	0.0056	400	880	0.1	0.39	0.11	0.27	1080	460	42	35	600	7.9	-2.02E+04	8.40E+03
Output 1_11	0.327	0.033	0.00625	0.00044	160	11.264	0.51	0.1	0.0543	0.0039	279	25	40.2	2.8	109.4	6.1	3480	410
Output 1_12	0.773	0.047	0.01138	0.00051	87.87346	3.93809	0.521	0.037	0.00412	0.0003	572	27	72.9	3.2	83	7	4160	120
Output 1_13	1.74	0.14	0.02	0.0013	50	3.25	0.781	0.094	0.00471	0.00035	985	52	127.5	8.1	95	4	4310	410
Output 1_14	0.111	0.012	0.0043	0.00018	232.5581	9.734992	0.199	0.024	0.00295	0.0002	105	11	27.7	1.1	59.5	4.3	2480	250
Output 1_15	0.215	0.03	0.00564	0.00035	177.305	11.00297	0.296	0.052	0.00333	0.00021	203	24	36.3	2.2	67.2	4.2	2170	560
Output 1_16	0.888	0.052	0.01196	0.00068	83.61204	4.753862	0.553	0.025	0.00377	0.00021	646	29	76.6	4.3	76.1	4.3	4361	73
Output 1_17	0.0605	0.0054	0.00424	0.00019	235.8491	10.56871	0.1026	0.0089	0.0031	0.00024	58.9	5.1	27.3	1.2	62.5	4.8	1400	180
Output 1_18	0.0636	0.0054	0.00421	0.00013	237.5297	7.334646	0.1132	0.0098	0.00336	0.00023	62.7	5.1	27.08	0.82	67.7	4.7	1660	170
Output 1_19	0.0471	0.0045	0.00405	0.00011	246.9136	6.706295	0.084	0.0082	0.00349	0.00019	46.6	4.3	26.06	0.72	70.5	4.7	1030	190
Output 1_20	0.933	0.036	0.062	0.0023	16.12903	5.983361	0.1085	0.0064	0.275	0.0078	667	20	388	14	4730	280	1721	86
Output 1_21	1.072	0.076	0.0692	0.0024	14.45087	5.601486	0.1086	0.003	0.1886	0.016	734	48	430	14	3480	130	1738	46
Output 1_22	1.424	0.076	0.1049	0.0048	9.523808	0.4362046	0.1086	0.002	0.203	0.0038	885	32	644	28	9670	260	1667	38
Output 1_23	0.268	0.018	0.01814	0.00046	55.12679	1.397923	0.1086	0.007	0.00497	0.00016	240	14	115.8	2.9	100.2	260	1730	120
Output 1_24	0.869	0.097	0.01142	0.00093	87.56667	7.131005	0.496	0.025	0.00529	0.00038	569	64	73.5	6	406.7	7.6	4190	84
Output 1_25	1.199	0.07	0.01454	0.00068	68.77579	3.216474	0.648	0.048	0.00374	0.00022	788	33	93	4.3	75.4	4.4	4540	140

Sample 71317 UTM Coordinates Sample 71317 (NAD83 Zone 11N): 437717 4183650

Day 2	Final207_235	Final207_235_Int2SE	Final206_238	Final206_238_Int2SE	Final238_206	Final238_206_Int2SE	Final207_206	Final207_206_Int2SE	Final208_232
Output_1_1	2.95	0.13	0.0293	0.0012	34.12969	1.397803	0.731	0.042	0.009918
Output_1_2	0.685	0.048	0.0094	0.00054	106.383	6.111363	0.537	0.031	0.00721
Output_1_3	1.271	0.091	0.01469	0.00085	68.07352	3.938903	0.66	0.046	0.00861
Output_1_4	53.4	2.4	0.514	0.024	1.945525	0.09084165	0.752	0.016	6.5
Output_1_5	42.5	1.2	0.399	0.01	2.506266	0.06281368	0.763	0.015	14.9
Output_1_6	45.4	1.2	0.429	0.011	2.331002	0.05976929	0.766	0.016	10.91
Output_1_7	4.63	0.67	0.0312	0.0049	32.05128	5.033695	-0.02	0.43	0.0485
Output_1_8	15.5	1.4	0.147	0.013	6.802721	0.6016012	0.79	0.15	0.0459
Output_1_9	2.8	3.7	-0.016	0.017	-62.5	66.40625	-0.4	1.4	0.021
Output_1_10	1.58	0.22	0.0162	0.0022	61.7284	8.382868	0.82	0.18	0.0043
Output_1_11	0.427	0.069	0.00584	0.00053	171.2329	15.53997	0.46	0.13	0.00473
Output_1_12	0.304	0.035	0.00587	0.00038	170.3578	11.02827	0.382	0.05	0.00357
Output_1_13	0.65	0.51	0.0116	0.0048	86.2069	35.67182	0.32	0.29	0.00212
Output_1_14	0.68	0.3	0.0101	0.0032	99.0099	31.36947	-3	4.8	0.00253
Output_1_15	0.64	0.49	0.0082	0.004	121.9512	59.4884	0.38	0.3	0.00178
Output_1_16	2.76	0.62	0.0339	0.0061	29.49853	5.307994	0.55	0.25	0.00882
Output_1_17	0.29	0.1	0.0106	0.0014	94.33962	12.45995	0.15	0.14	0.186

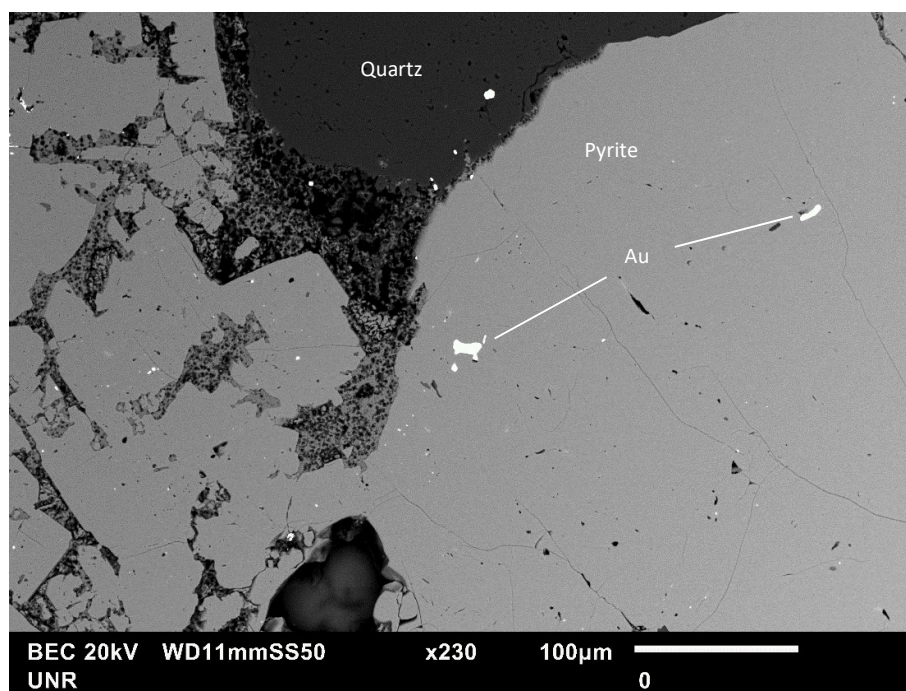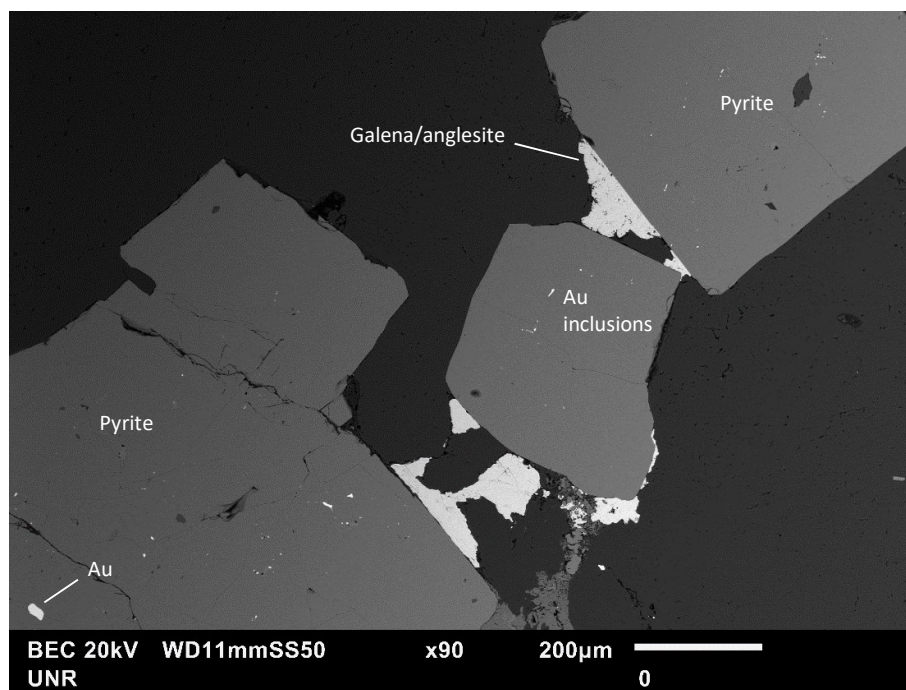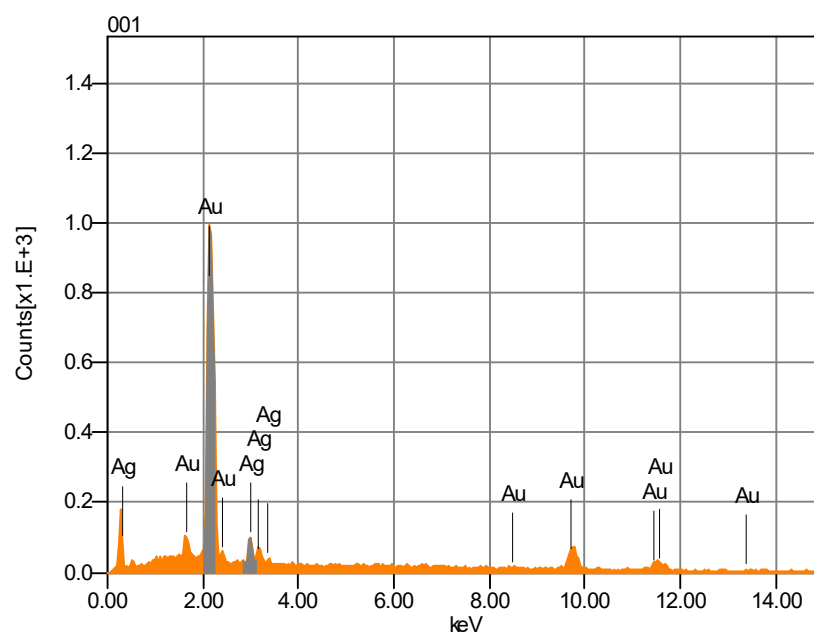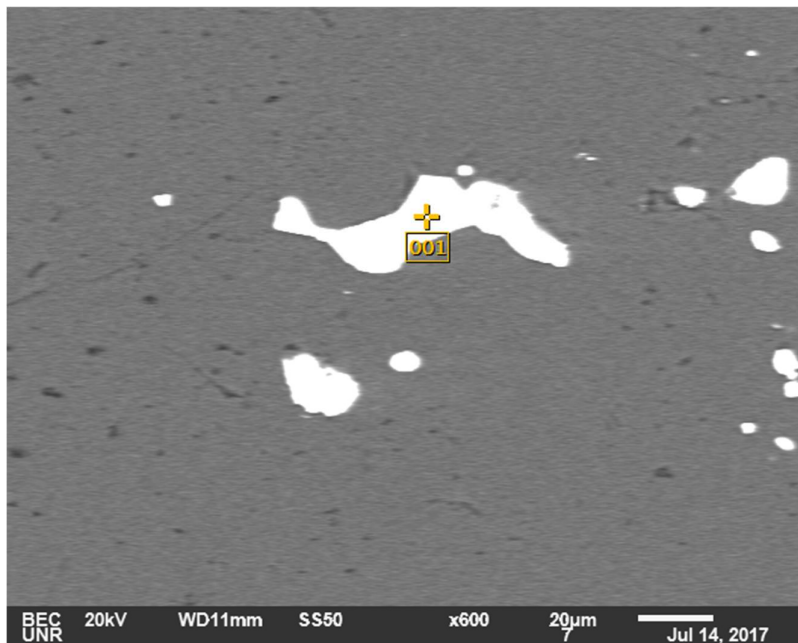|	Final208_232_Int2SE	FinalAge207_235	FinalAge207_235_Int2SE	FinalAge206_238	FinalAge206_238_Int2SE	FinalAge208_232	FinalAge208_232_Int2SE	FinalAge207_206	FinalAge207_206_Int2SE
Output_1_1	0.00076	1388	34	186.8	7.1	185	15	4810	100
Output_1_2	0.00062	521	28	60.2	3.4	145	12	4284	95
Output_1_3	0.00098	809	39	93.9	5.4	173	19	4550	130
Output_1_4	1.2	4007	47	2640	100	2.96E+04	2.90E+03	4854	37
Output_1_5	2.1	3823	28	2162	47	4.68E+04	2.10E+03	4882	34
Output_1_6	0.66	3884	27	2290	50	4.86E+04	1.20E+03	4890	36
Output_1_7	0.0073	1690	120	195	31	930	140	-3.40E+04	1.60E+04
Output_1_8	0.0038	2749	95	875	72	906	73	4650	710
Output_1_9	0.041	1620	780	-110	110	340	840	-3.50E+04	2.80E+04
Output_1_10	0.00048	952	86	103	13	86.5	9.7	1.30E+03	1.90E+03
Output_1_11	0.00046	334	41	37.5	3.4	95.2	9.3	3.20E+03	1.20E+03
Output_1_12	0.00024	263	26	37.7	2.4	72.1	4.9	2730	540
Output_1_13	0.00078	910	190	75	29	43	16	-1.23E+04	5.60E+03
Output_1_14	0.00047	710	130	63	20	50.9	9.6	-6.50E+04	3.90E+04
Output_1_15	0.0006	780	150	51	25	36	12	-7.70E+03	3.40E+03
Output_1_16	0.00086	1450	120	218	37	177	17	1.60E+03	2.40E+03
Output_1_17	0.085	270	82	67.5	8.7	1780	760	-2.80E+03	2.30E+03

Appendix C-1: Petrography

Calcite

Plagioclase

Sample
722DW1
Two-mica
granite

500 µm

Chlorite after garnet
(Mn>Fe)

1.0 mm

Sample
629BR1
Two-mica
granite

Sample MR69-327

Au

50.0 µm

Quartz

Sample MR69-327

Pyrite

Quartz

100 µm

Au

Chemical formula	mass%	Atom%	Sigma	Net	K ratio	Line
Ag	11.50	19.18	0.30	6729	0.0271451	L
Au	88.50	80.82	0.68	61794	0.2791862	M
Total	100.00	100.00				
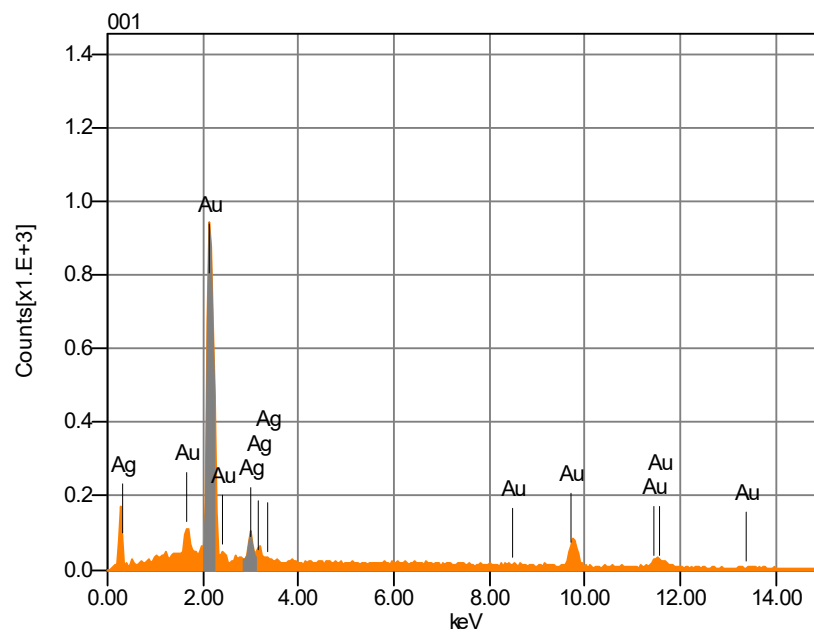
Chemical formula	mass%	Atom%	Sigma	Net	K ratio	Line
Ag	9.65	16.33	0.32	5247	0.0211368	L
Au	90.35	83.67	0.71	59124	0.2667509	M
Total	100.00	100.00				

Sample 71803

BEC 20kV WD11mm SS50 x3,300 5µm Jul 18, 2017
UNR 8
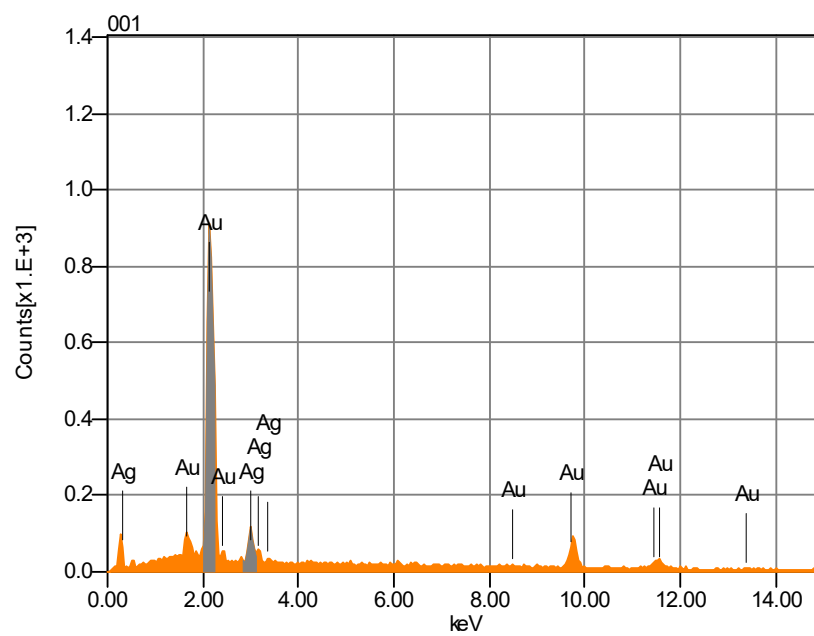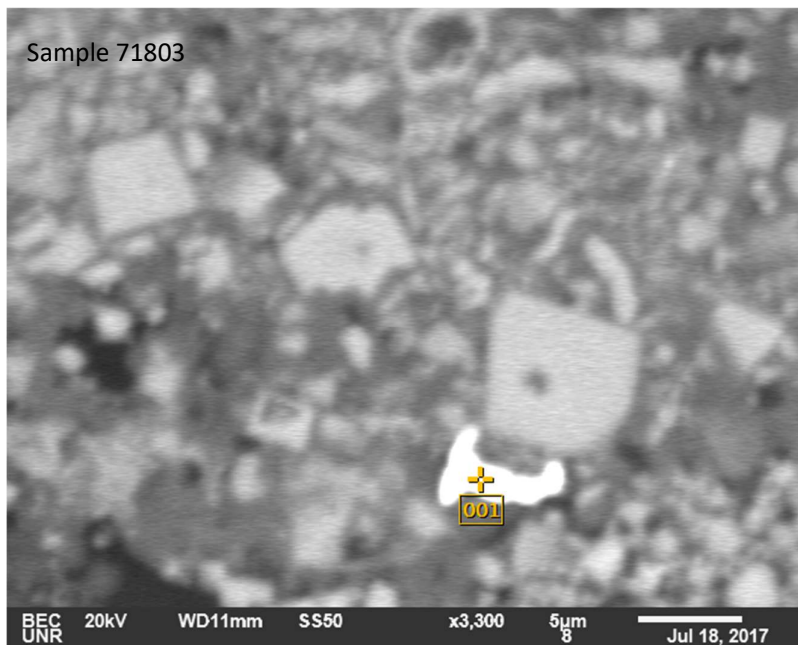
Chemical formula	mass%	Atom%	Sigma	Net	K ratio	Line
Ag	10.76	18.05	0.33	5663	0.0227806	L
Au	89.24	81.95	0.72	56226	0.2533225	M
Total	100.00	100.00				

Sample 71803

BEC UNR 20kV WD11mm SS50 x3,300 5μm 8 Jul 18, 2017
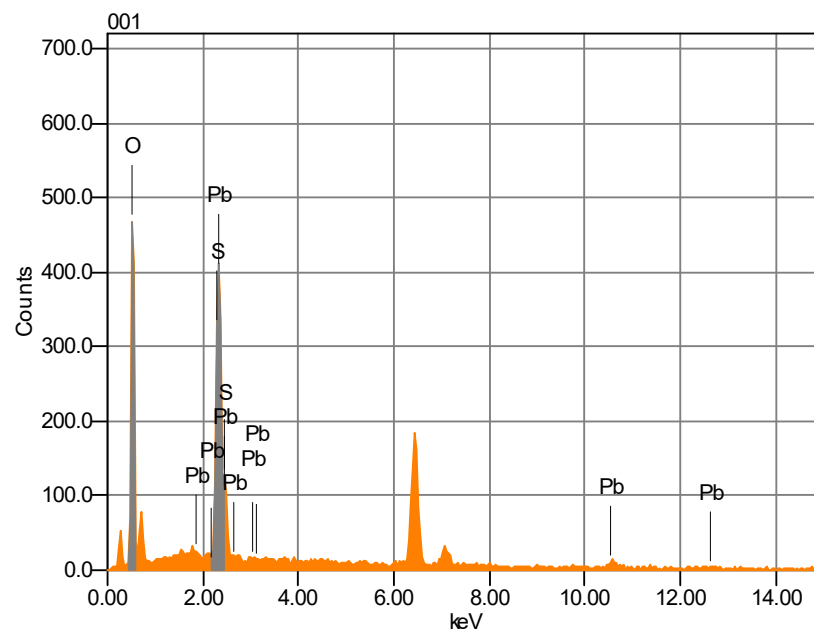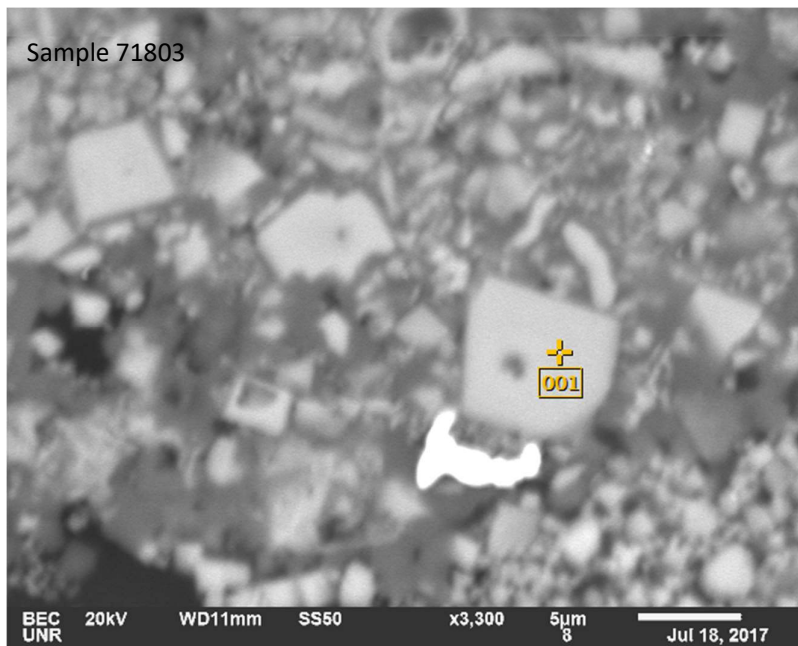
Chemical formula	mass%	Atom%	Sigma	Net	K ratio	Line
O	45.81	83.92	0.28	10744	0.0612224	K
S	10.88	9.95	0.18	9667	0.0238822	K
Pb	43.30	6.13	0.83	16880	0.0789259	M
Total	100.00	100.00				

Sample 71803

001
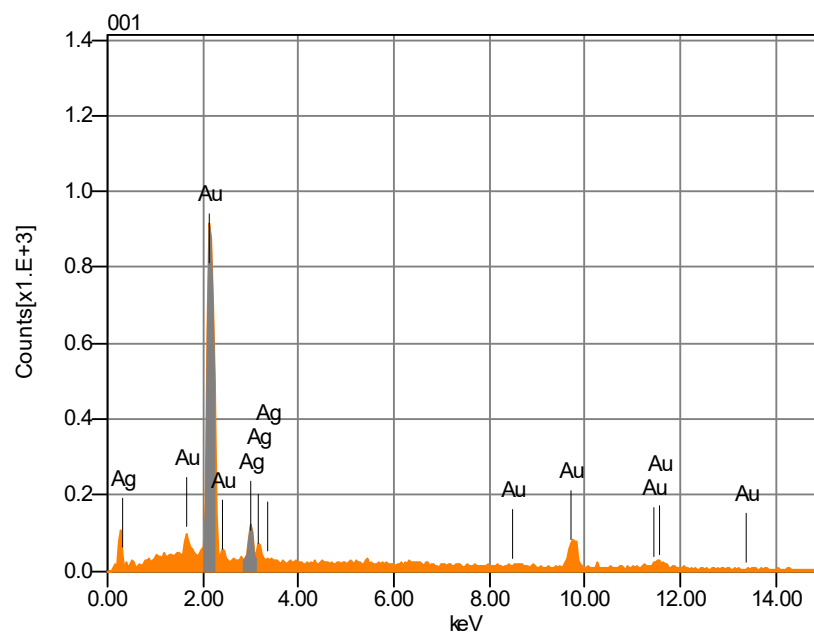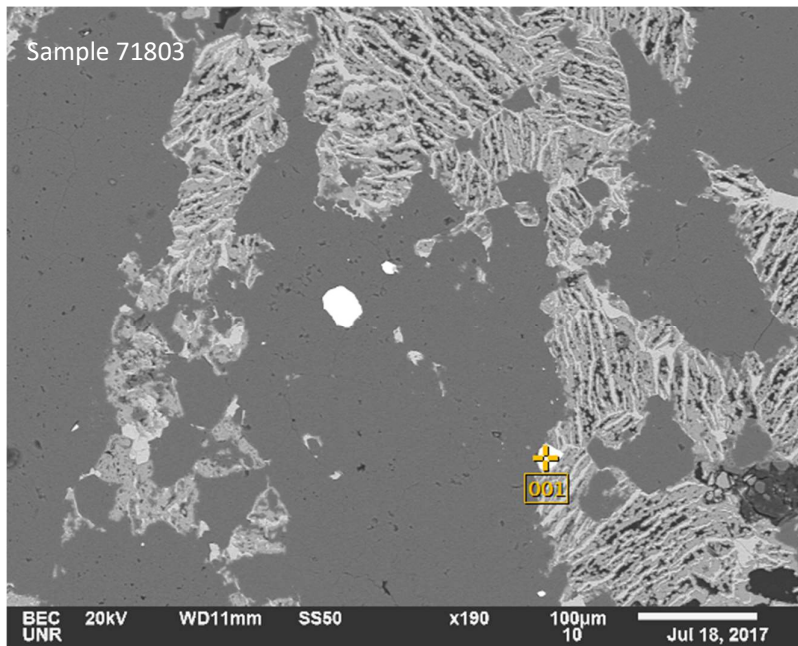
Chemical formula	mass%	Atom%	Sigma	Net	K ratio	Line
Ag	12.57	20.79	0.34	7016	0.0282847	L
Au	87.43	79.21	0.70	57923	0.2615153	M
Total	100.00	100.00				
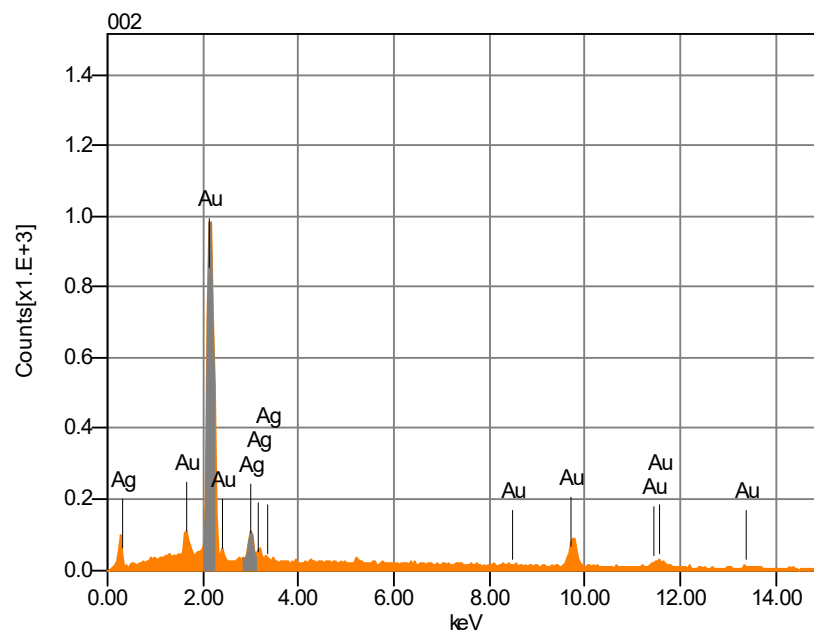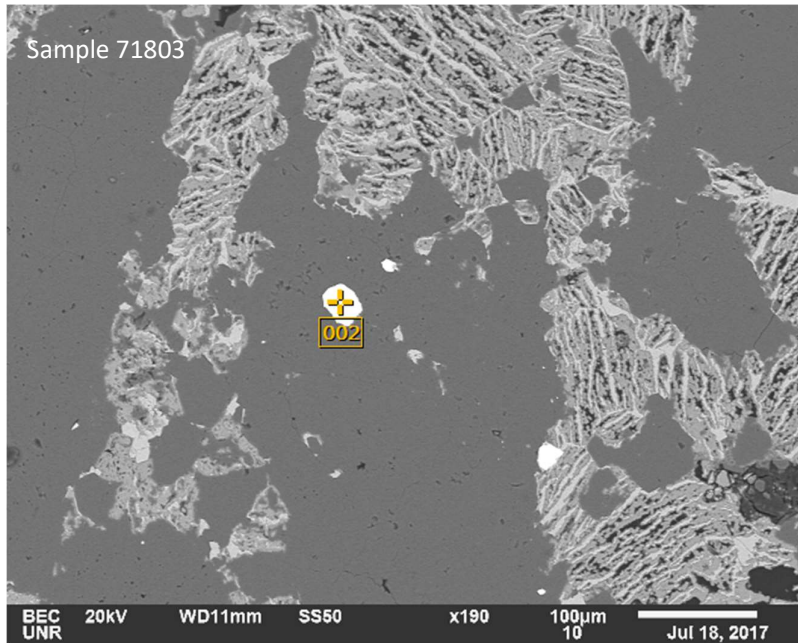
Chemical formula	mass%	Atom%	Sigma	Net	K ratio	Line
Ag	10.01	16.88	0.32	5687	0.0229410	L
Au	89.99	83.12	0.69	61457	0.2776643	M
Total	100.00	100.00				

Sample 71803

BEC UNR | 20kV | WD11mm | SS50 | x190 | 100μm 10 | Jul 18, 2017

003
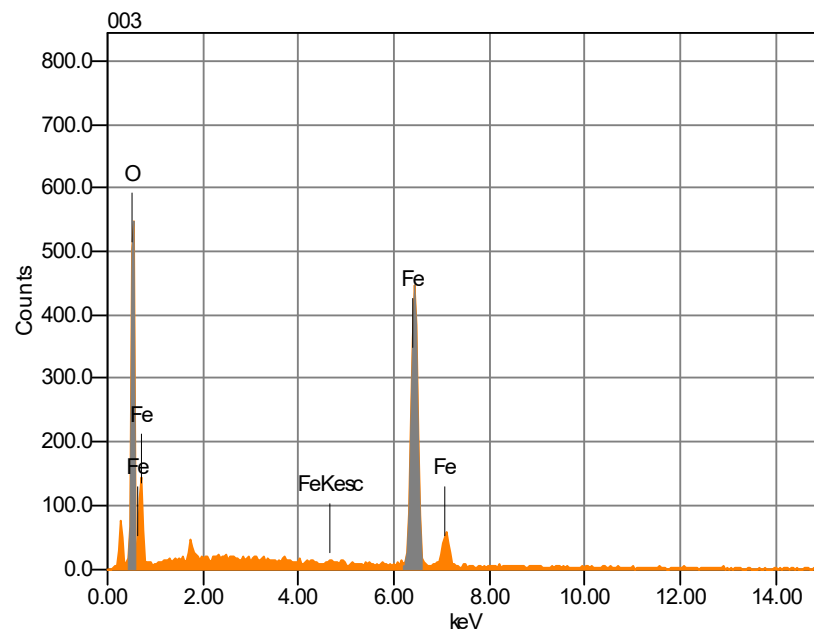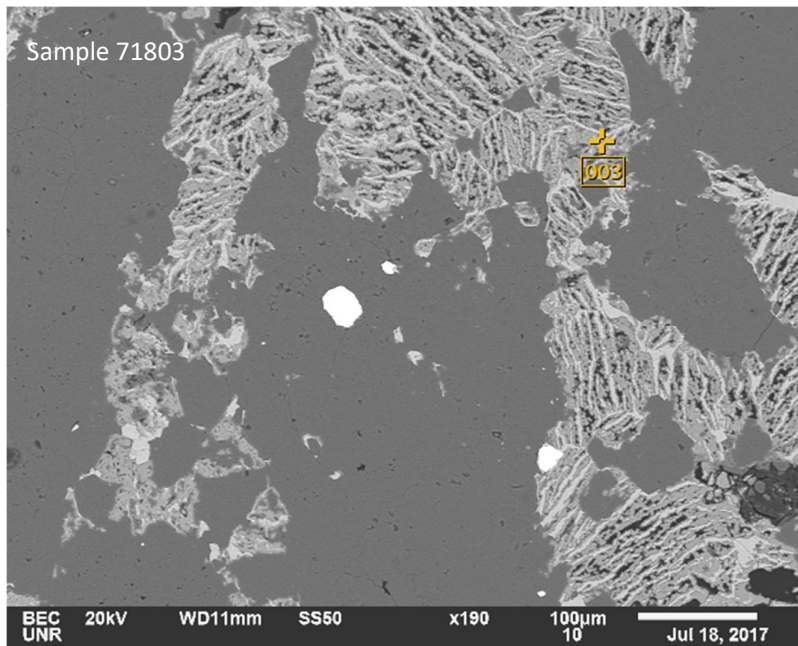
Chemical formula	mass%	Atom%	Sigma	Net	K ratio	Line
O	38.61	68.70	0.22	13357	0.0762150	K
Fe*	61.39	31.30	0.56	18482	0.1350628	K
Total	100.00	100.00				
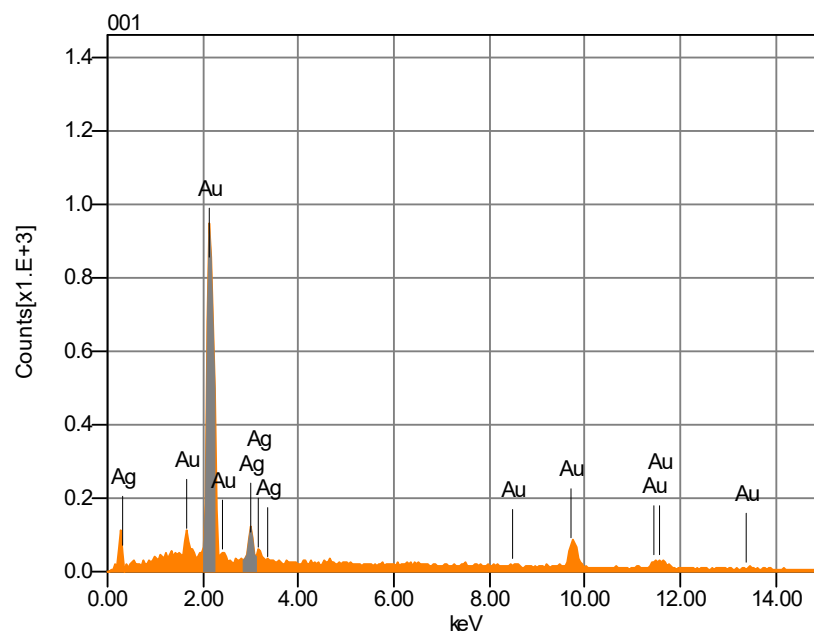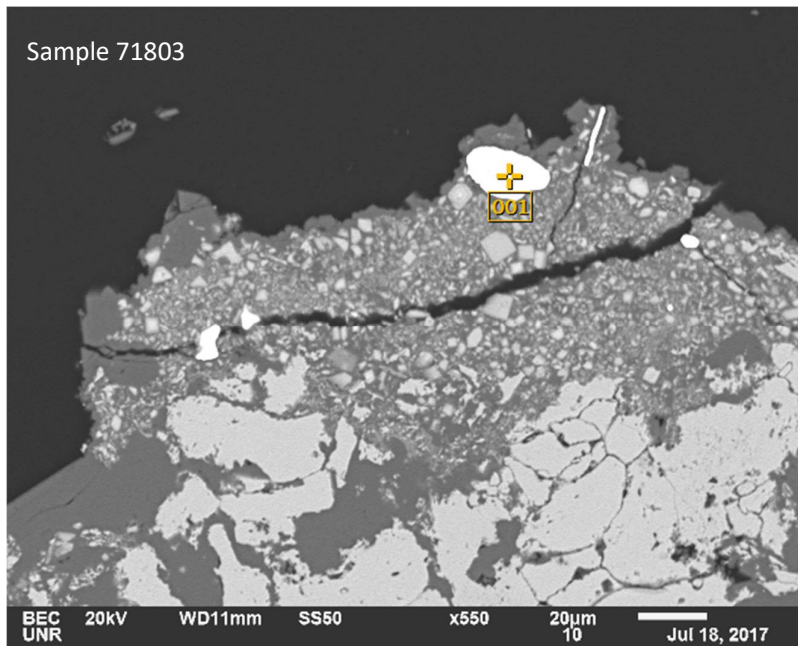
Chemical formula	mass%	Atom%	Sigma	Net	K ratio	Line
Ag	11.35	18.94	0.33	6344	0.0255930	L
Au	88.65	81.06	0.70	59188	0.2674137	M
Total	100.00	100.00				
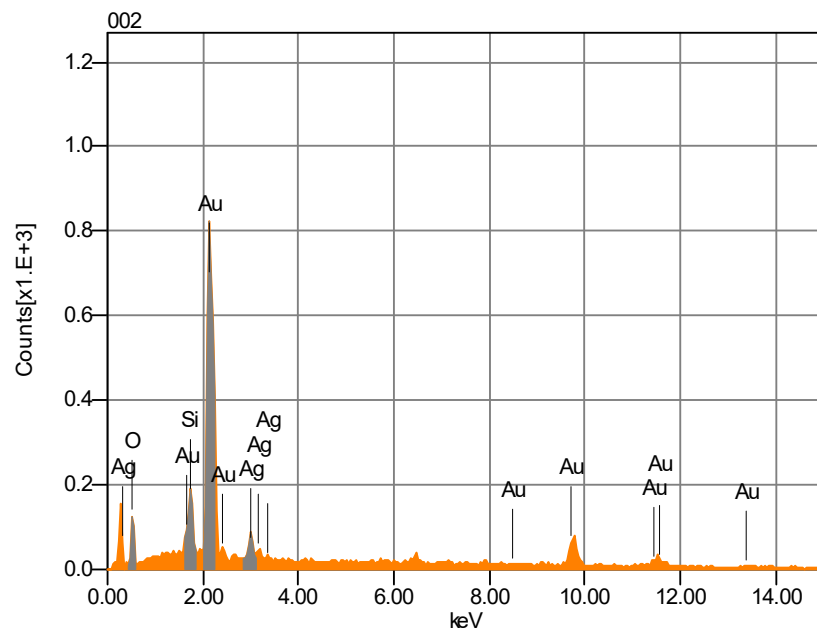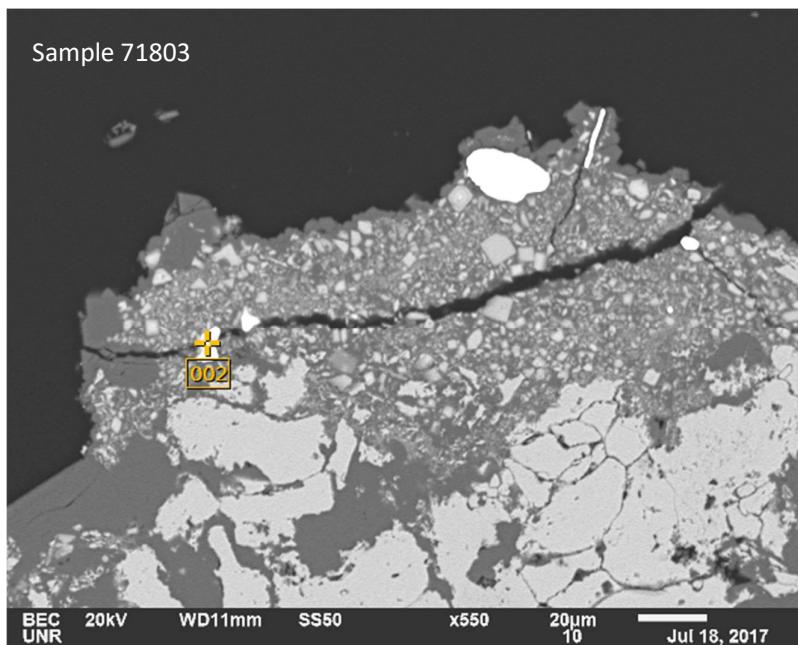
Chemical formula	mass%	Atom%	Sigma	Net	K ratio	Line
O	12.36	57.14	0.17	2715	0.0158176	K
Si	3.44	9.05	0.12	5112	0.0106988	K
Ag	7.09	4.86	0.28	4049	0.0162639	L
Au	77.11	28.95	0.66	50507	0.2272373	M
Total	100.00	100.00				

Sample 71803

BEC UNR | 20kV | WD11mm | SS50 | x550 | 20μm 10 | Jul 18, 2017

003
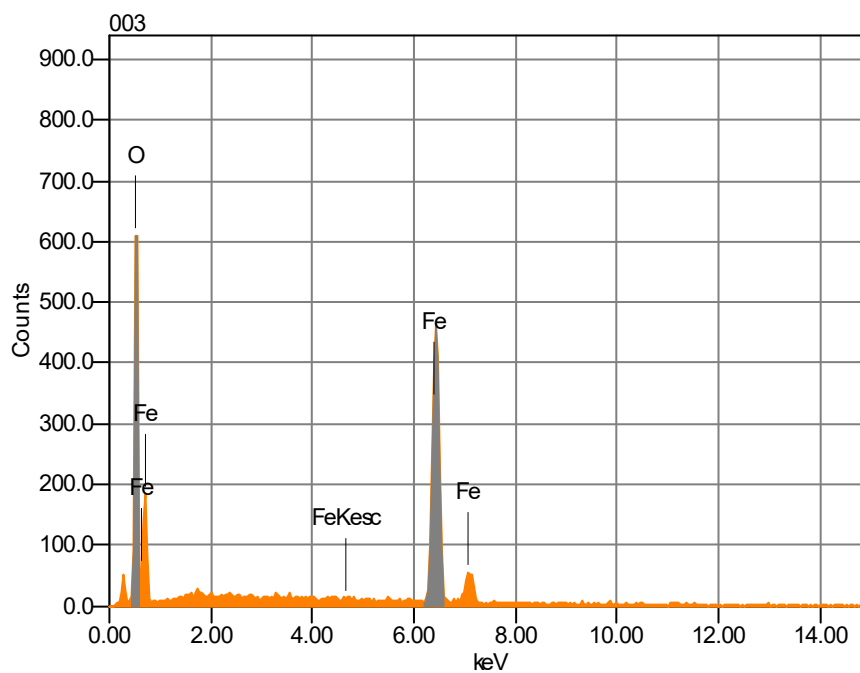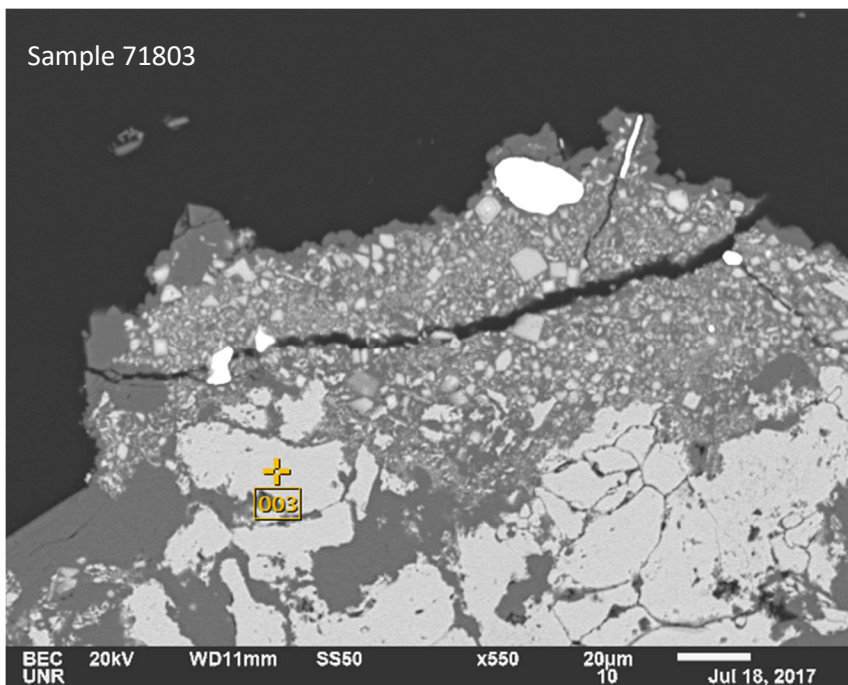
Chemical formula	mass%	Atom%	Sigma	Net	K ratio	Line
O	39.79	69.76	0.21	14686	0.0839138	K
Fe*	60.21	30.24	0.54	19202	0.1405186	K
Total	100.00	100.00				

Sample 71604
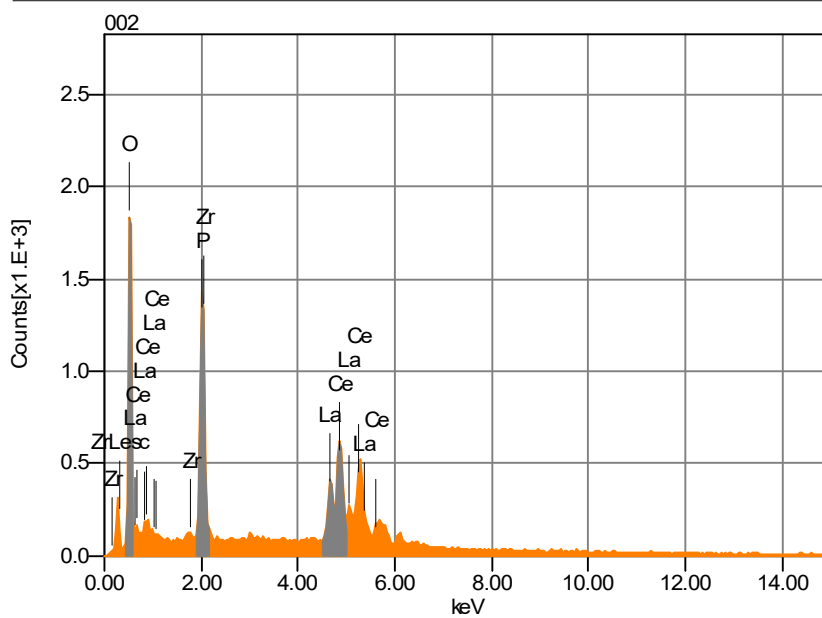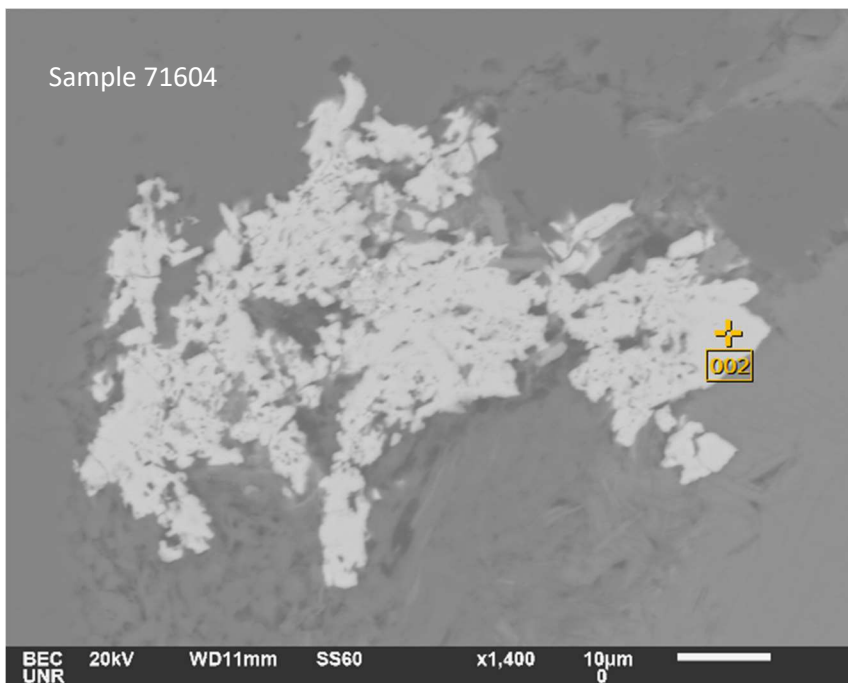
Chemical formula	mass%	Atom%	Sigma	Net	K ratio	Line
O	33.42	72.00	0.11	41643	0.2700883	K
P	11.04	12.29	0.09	44718	0.1436723	K
Zr*	15.28	5.78	0.24	41221	0.1584482	L
La*	15.26	3.79	0.20	29567	0.2271396	L
Ce*	25.00	6.15	0.26	45957	0.3783613	L
Total	100.00	100.00				

Chemical formula	mass%	Atom%	Sigma	Net	K ratio	Line
O	34.93	73.24	0.11	50064	0.3300850	K
P	10.97	11.88	0.08	50532	0.1650417	K
Zr*	14.75	5.42	0.22	45248	0.1768088	L
La*	13.86	3.35	0.18	30487	0.2380840	L
Ce*	25.50	6.11	0.24	53220	0.4454141	L
Total	100.00	100.00				
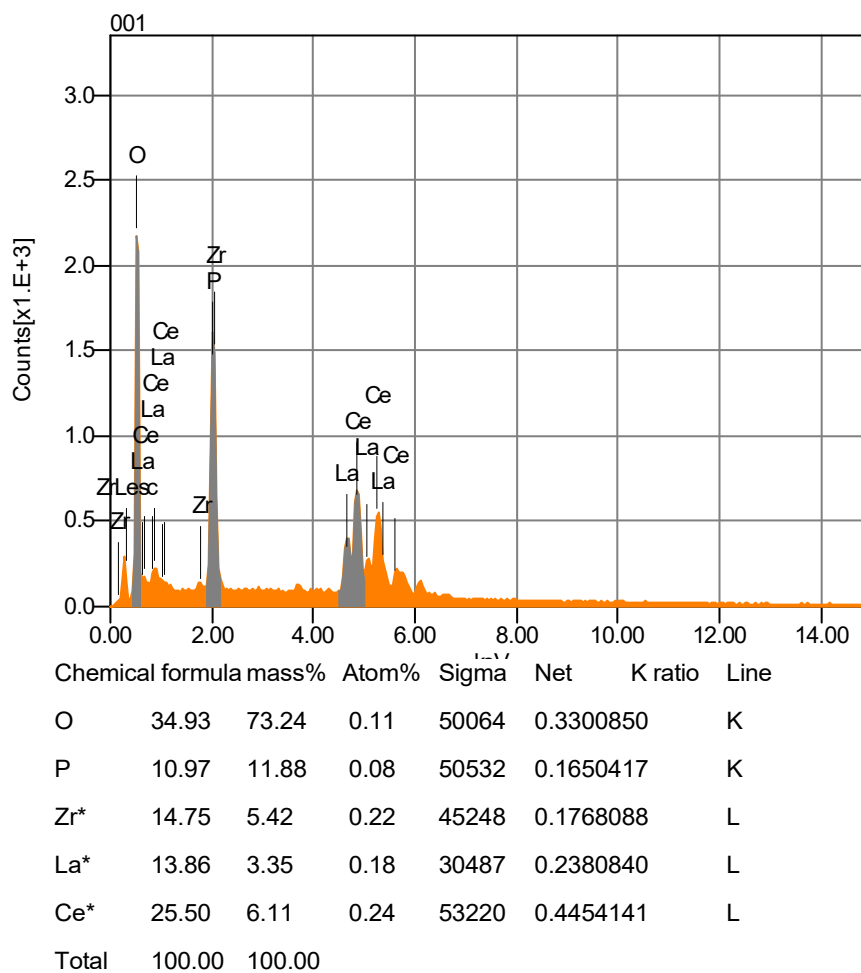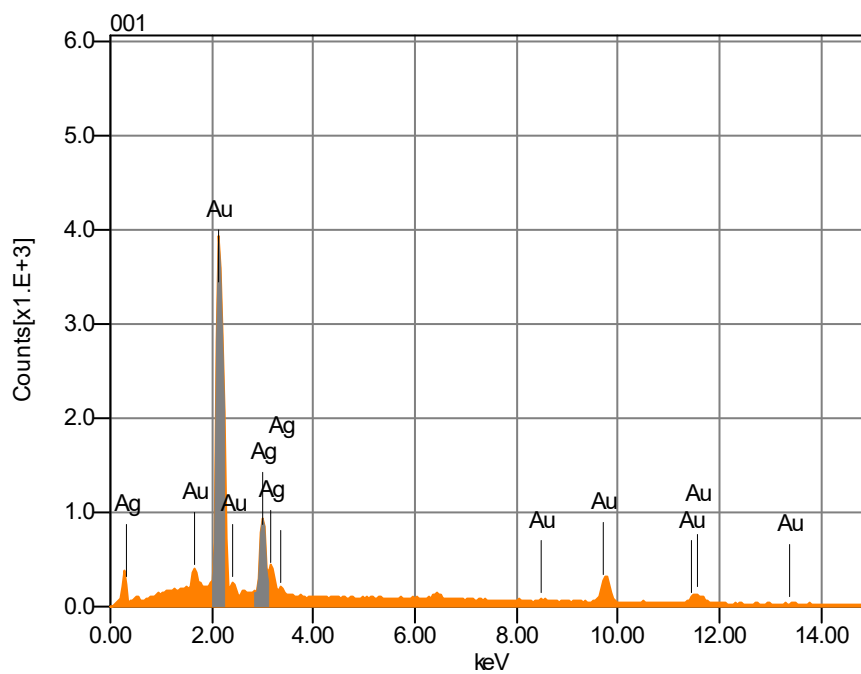
Chemical formula	mass%	Atom%	Sigma	Net	K ratio	Line
Ag	20.97	32.64	0.19	56113	0.2840550	L
Au	79.03	67.36	0.31	240496	1.3634601	M
Total	100.00	100.00				

Sample 729Qtz
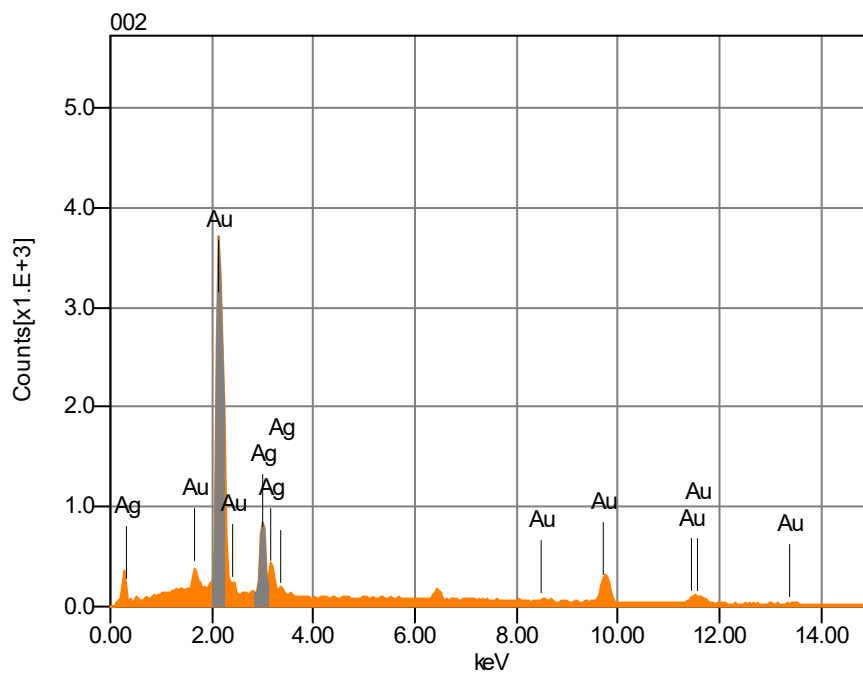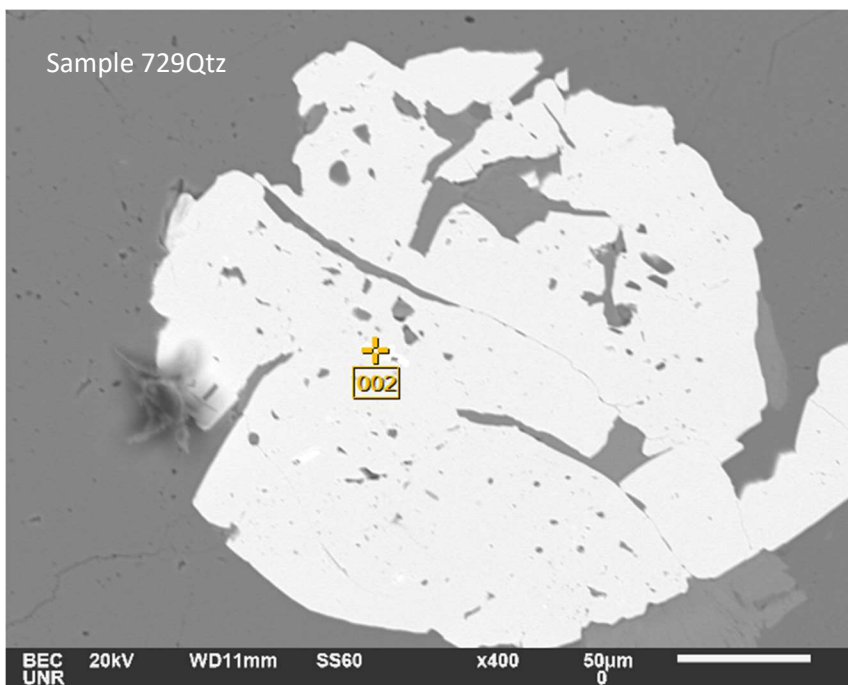
Chemical formula	mass%	Atom%	Sigma	Net	K ratio	Line
Ag	21.96	33.95	0.20	53431	0.2646614	L
Au	78.04	66.05	0.34	214763	1.1914016	M
Total	100.00	100.00				

Sample 624BR5   Two-mica granite

25 µm   25 µm   25 µm

25 µm   25 µm   25 µm

Sample 71502   Au-bearing   quartz

$CO_{2(l)}$

25 µm   25 µm   25 µm

$CO_{2(l)}$

25 µm   25 µm   25 µm